Experimental Tight Rock Characterization and Surfactant Screening for Hydraulic Fracturing Operations

by

Mohammad Yousefi

A THESIS SUBMITTED IN PARTIAL FULFILLMENT OF
THE REQUIREMENTS FOR THE DEGREE OF

DOCTOR OF PHILOSOPHY

in

Petroleum Engineering

Department of Civil and Environmental Engineering

UNIVERSITY OF ALBERTA

Abstract

Recently, unconventional resources, especially tight and shale reservoirs, have developed rapidly because of advances in horizontal drilling technologies and hydraulic fracturing technique. For example, the Montney tight oil play with a size of more than 90,000 km^2, has estimated in-place hydrocarbon resources of almost 2,133 Tcf of natural gas, 28.9 billion bbl of natural-gas liquids, and 136.3 billion bbl of oil (Reynolds et al. 2014). Based on the annual energy outlook of the Energy Information Administration (Nalley and LaRose 2022), tight oil production in the US will increase from 8.2 million bbl/day in 2022 to 9.1 million bbl/day in 2050 ,and it will form more than 70% of all the US oil production. The tight and shale gas production in the US will also increase from 31.7 Tcf in 2022 to 39.2 Tcf in 2050, forming more than 92% of all the US natural gas production. Despite the great extent of unconventional resources, the recovery factor of those reservoirs is typically less than 10%, which shows the importance of enhanced oil/gas recovery methods. The first step in this path is to characterize rock/fluid properties to better understand fluid flow through such tight porous media.

Measuring tight-rock properties, particularly permeability, is important in a wide range of engineering applications, from radioactive waste disposal and CO2 storage to production from unconventional hydrocarbon reservoirs. The steady-state method of permeability measurement is currently considered impractical for tight rocks due to the long time needed to reach stabilized pressure and flowrate. In contrast to experimental results, the diffusivity equation shows the steady state to happen much faster when a constant injection flowrate is used as a boundary condition. In this study, we investigate the reason behind the inconsistency between the modeled and measured equilibrium time. We modify the boundary condition of the diffusivity equation based on an

analogy from the well-testing models. We propose a semi-analytical solution for a more general diffusivity equation with a modified boundary condition. The results show that the main reason that makes the steady-state method time-consuming is the accumulator “storage effect”. When dealing with low-permeability rocks, the compressibility-induced flowrate, which is pressure-dependent, could be in the order of pump flowrate and makes the permeability measurement time-consuming. We modify the conventional coreflooding device to reduce the time of permeability measurement, making the steady-state method practical for tight-rock samples. The modified device is used to measure the permeability of a tight-rock sample, and the model can match the measured data with good accuracy. Reducing the volume of the accumulator vessel from 500 cc to around 10 cc causes a 50- fold decrease in the time required for steady-state establishment.

During hydraulic fracturing operation, a huge volume of fracturing fluid is pumped into the well to create a network of fractures and propagate the fractures away from the wellbore. Some part of the injected fluid remains in the fracture system, and some part of it leaks off into the rock matrix. At the end, pressure is released to let the well flow. During flowback and post flowback periods, only a small portion (5-50%) of the injected fluid will be recovered (Bertoncello et al. 2014). The remaining leaked-off fracturing fluid will form a water-loaded zone near the fracture face that hinder oil production during flowback (Bennion et al. 1996).

On the other hand, the imbibition of fracturing fluid into the rock matrix can be considered as a production mechanism that forces oil out of the rock matrix (Kathel and Mohanty 2013). This dual behavior of fracturing fluid led researchers to find an optimized situation where imbibition oil recovery is maximum, and water blockage near the fracture face is minimum. Chemical additives such as surfactant solutions and microemulsions have been introduced to serve this purpose. Screening such additives for field applications requires evaluating their impacts on regained permeability and post-flowback well performance. In this study, we are using our developed method to measure liquid permeability before leak-off and after flowback to investigate the effects of different surfactant solutions on regained permeability of tight plugs. The plugs we use are from the Montney Formation with permeabilities in the range of micro-Darcy. We also measure the particle size distribution of structures formed in the surfactant solution used as the leak-off fluid. Then, we compare it with the pore-throat size distribution of the plug coming from the mercury injection capillary pressure (MICP) test to evaluate the possibility of pore throat blockage by particles in surfactant solution. Ultimately, we investigate the effect of initial water saturation (S_{wi}) on the performance of surfactant solutions in the enhancement of regained permeability after flowback.

The two-phase flow of immiscible fluids in porous media has been studied for a long time in different engineering disciplines. Relative permeability (k_r) is one of the constitutional relationships in the general equation governing immiscible displacement that needs to be determined. Due to the complexity and nonlinear nature of the governing equations of the problem, such as capillary pressure, there is no unique model for the relative permeability. The modified Brooks and Corey (MBC) model is the most common model for k_r prediction. Here, a practical technique is presented to measure k_r for low-permeability tight rocks. We use this experimental data to tune the empirical constants of the MBC model. The proposed method is based on a simple mathematical technique that uses assumptions of frontal advance theory to model the pressure drop along the core plug during two-phase immiscible displacement at constant-injection flowrate. We assume that the maximum point on the modeled pressure profile corresponds to the minimum total mobility (summation of oil and water mobilities), which happens at the breakthrough time. We also assume that in the plot of mobility vs. water saturation, the minimum of total mobility

coincides with the intersection point of oil mobility and water mobility. At the end, the amount of work for an immiscible displacement is calculated as the area under the pressure-profile curve. The effect of initial water saturation (S_{wi}) and interfacial tension (IFT) is studied on the work required for an immiscible displacement. Using this concept, it is concluded that adding chemical additives such as surfactants to fracturing fluids can help the reservoir oil to remove the water blockage out of the rock matrix more easily while maintaining the flowrate at an economic level.

Preface

This thesis is an original work by Mohammad Yousefi. All or parts of Chapters 2 to 4 have been published as peer-reviewed papers or submitted for peer review and publication. I was responsible for conducting laboratory tests, model development, and writing and editing these papers.

Chapter 2 has been published as Yousefi, Mohammad, and Hassan Dehghanpour. 2022. “A Model and Measurement Technique for Liquid Permeability of Tight Porous Media Based on the Steady-State Method.” *Energy & Fuels*.

Chapter 3 has been submitted (under review) as Yousefi, Mohammad, and Hassan Dehghanpour. 2022. Modeling Two-Phase Flow in Tight Core Plugs with an Application for Relative Permeability Measurement. *SPE Reservoir Evaluation & Engineering*.

Chapter 4 is ready for submission as Yousefi, Mohammad, and Hassan Dehghanpour. 2022. A Laboratory Protocol for Surfactant Screening in Hydraulic Fracturing Operation.

A part of Chapter 2 and Chapter 3 has been published as Yousefi, M., Yuan, L., & Dehghanpour, H. (2020, October). Advances in Understanding Relative Permeability Shifts by Imbibition of Surfactant Solutions into Tight Plugs. In SPE Annual Technical Conference and Exhibition. OnePetro SPE-201520-MS.

A part of Chapter 3 and Chapter 4 has been published as Yousefi, M., Habibi, A., & Dehghanpour, H. (2020, August). Surfactant in Fracturing Fluid: Enhancing Imbibition Oil Recovery or Blocking Pore Throats? In SPE Improved Oil Recovery Conference. OnePetro SPE-200470-MS.

Dedicated to my beloved family.

Acknowledgements

I would like to express my gratitude and respect to my supervisor, Dr. Hassan Dehghanpour who has always been generous with his time and advice. Most importantly, however, he has encouraged me to develop my own ideas. I am forever indebted to him for all academic and life lessons he taught me during my PhD journey.

My gratitude extends to Dr. Japan Trivedi and Dr. Juliana Leung as my supervisory committee, Dr. Mohtada Sadrzadeh and Dr. Arman Hemmati as my internal examiners, as well as Dr. Rouzbeh Ghanbarnezhad Moghanloo as my external examiner from the University of Oklahoma.

I also would like to appreciate my colleagues, friends, and family for their valuable help and contributions.

Table of Contents

List of Tables

List of Figures

Chapter 1
General Introduction

1.1 Overview of Unconventional Resources

The classical definition of unconventional resources has evolved through time and will change as available exploration and production technologies and also the economic environment are changing with time. The general definition based on Energy Information Administration (EIA) website encompasses the oil and gas produced by means that are not classified as conventional methods. The list is broad and changes from time to time. It includes but is not limited to oil and gas shale reservoirs, tight sands, oil sands, coalbed methane, extra heavy oil, and gas hydrates. Our focus in this thesis is tight and shale reservoirs.

Unconventional resources have become an important energy source due to recent developments in horizontal drilling and multistage hydraulic fracturing. They have been developed to cope with the increasing demand for energy. Based on the annual energy outlook (AEO) of 2022 (Nalley and LaRose 2022), the US energy consumption is expected to grow from 98.1×10^{15} BTU in 2021 to 110.2×10^{15} BTU in 2050. In line with consumption, the US energy production will also increase from 98.9×10^{15} BTU in 2021 to 117.9×10^{15} BTU in 2050. As shown in **Figure 1-1**, most of the produced energy is expected to come from crude oil and natural gas.

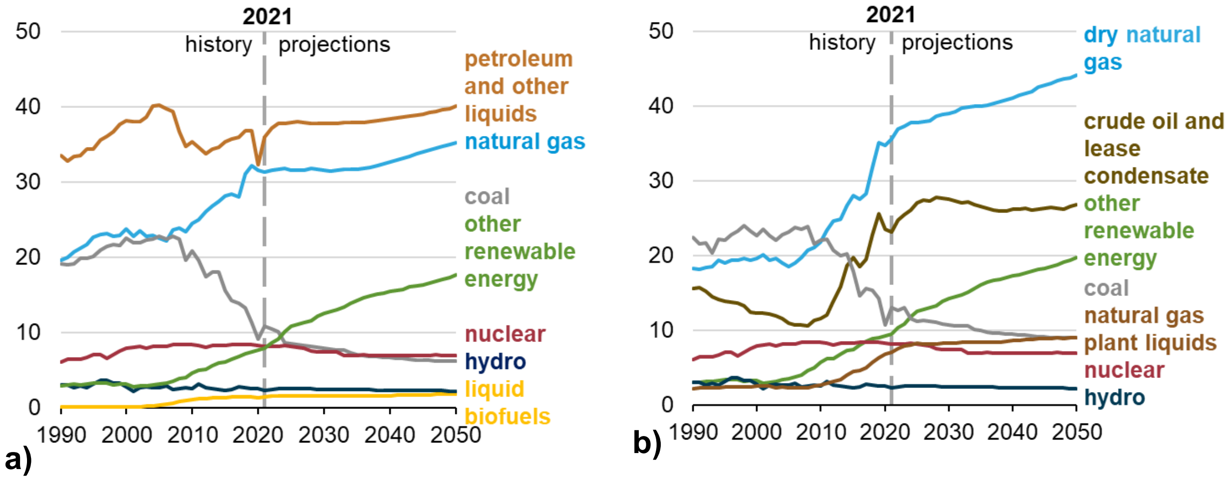

Figure 1-1: a) Energy consumption by fuel, b) Energy production by source, based on the reference case (quadrillion British thermal units) (Nalley and LaRose 2022).

Investigating the source of crude oil and natural gas produced in the US shows that more than 70% of all US oil production and more than 92% of all US natural gas production is expected to come from the tight and shale reservoirs in 2050 (**Figure 1-2**).

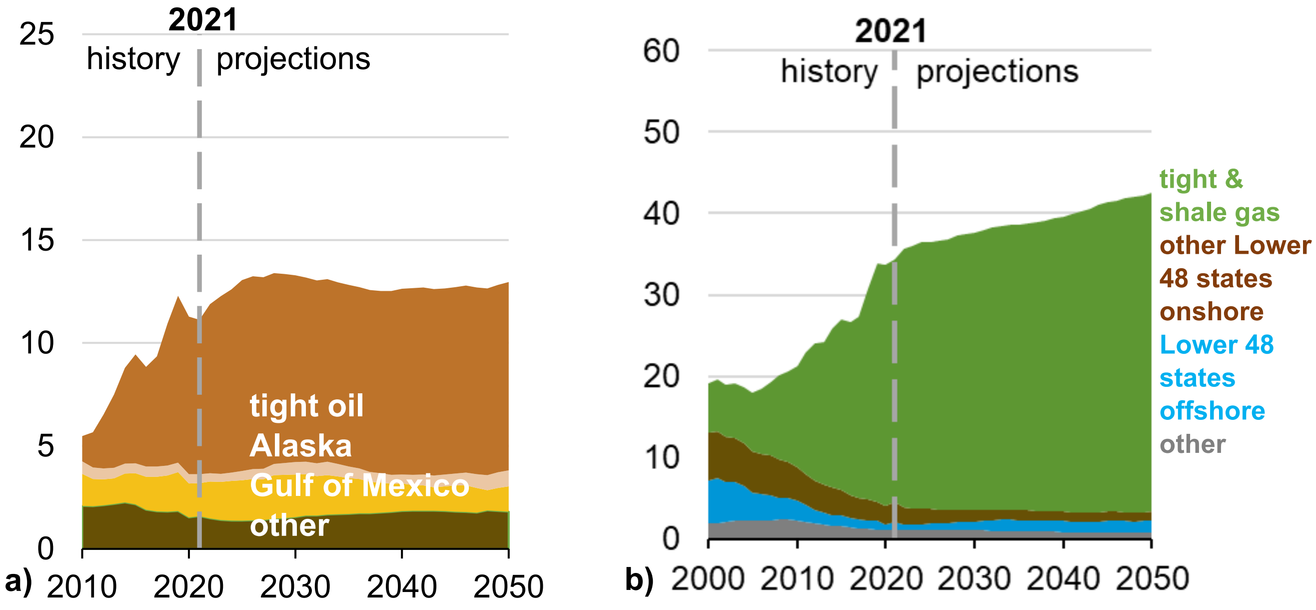

Figure 1-2: a) Crude oil production (million bbl/day), b) Natural gas production (Tcf) based on the reference case (Nalley and LaRose 2022).

The unconventional tight and shale reservoirs are geologically and petrophysically complex (Ahmed and Meehan 2016). The fine-grained structure, organic-rich pore space, extremely low permeability, and small-scale heterogeneity of these unconventional reservoirs pose significant challenges in formation evaluation and reservoir characterization.

1.2 Permeability Measurement

1.2.1 Steady-state method: Permeability is a property of the porous medium that shows the ease of fluid conductance through the medium. Darcy (1856) conducted some experiments on sand packs and came up with an equation that describes fluid flow through porous media (**Eq. 1-1**).

$$Q = \frac{kA}{\mu}\frac{\Delta P}{L} \tag{1-1}$$

Eq. 1-1 can be used to measure the absolute permeability when the porous medium is 100% saturated with a liquid. It is also applicable to rock samples that are saturated with liquid 1 in the presence of an irreducible saturation of liquid 2 to calculate the effective permeability to liquid 1. In order to measure the liquid permeability, several different steady-state flowrates are established across the plug sample. At each flowrate, the pressure drop across the plug sample is recorded. A plot of Q vs. ΔP, shows a straight line that passes through the origin. The permeability can be calculated from the slope of the straight line knowing the dimensions of the plug sample and the viscosity of the fluid used for measurement. It is also possible to impose different pressure drop values across the plug sample and wait for the flow to become stable. When steady flow is established, the flowrate can be measured. Plotting Q vs. ΔP can give us the liquid permeability of the plug sample.

Compared to liquids, gasses have much smaller viscosity values that need a smaller injection pressure to establish a similar flowrate. Using gas for permeability measurement is generally easier than using liquids. Despite the advantages that gases have for permeability measurement, it should be noted that they are compressible compared to liquids and thus, the flowrate of gas depends on the pressure. For example, if the inlet pressure is twice the outlet pressure, based on Boyle's law, the outlet flowrate would be twice the inlet flowrate. Therefore, a correction must be made for the expansion of the gas when using the Darcy equation. A convenient way is to correct the measured flowrate at the core inlet or outlet to the mean flowrate (Q_m) at mean pressure ($P_m = \frac{P_1+P_2}{2}$). Eq. 1-1 can be rearranged as **Eq. 1-2**:

$$k_g = \frac{Q_m \mu L}{A \Delta P} \tag{1-2}$$

If the flow is measured at the plug outlet, which is at atmospheric pressure, we can write:

$$Q_m = \frac{Q P_{atm}}{P_m} \tag{1-3}$$

Therefore, the Darcy equation for gas flow can be written as:

$$k_g = \frac{2 Q \mu L P_{atm}}{A(P_1^2 - P_2^2)} \tag{1-4}$$

Permeability is a property of the porous medium and should be constant regardless of the type of fluid used for measurement. Klinkenberg (1941) found that the measured permeability of a plug sample is affected by the type of gas and pressure since the gas flow in porous media is affected by slip flow. He correlated the gas permeability at mean pressure to the true liquid permeability by **Eq. 1-5**.

$$k_g = k_L\left(1 + \frac{b}{P_m}\right) \tag{1-5}$$

Therefore, if we plot k_g vs. $1/P_m$, it results in a straight line that its y-intercept shows the true liquid permeability.

The steady-state method is the standard method for the measuring permeability of a rock sample in the laboratory. It is comparatively simple and straightforward in terms of setup, operation, and even analytical solution. However, its application for very low permeability rocks is considered impractical because of the long time needed for the steady state establishment.

1.2.2 Unsteady-state methods:

The unsteady-state methods are usually used for low permeability samples. There are two main methods in this category: the pulse decay method and the GRI or pressure fall-off method. The pulse decay is the most common experimental method for the permeability measurement of tight rock samples. In contrast to steady-state experiments, the pulse decay method requires two gas cylinders of known volumes on the upstream and downstream of the core holder. Pressure in each cylinder and pressure difference between the two cylinders are measured with pressure sensors. Isothermal condition is of great importance in this method since temperature fluctuations can introduce error in permeability calculation. **Figure 1-3** shows a schematic of the pulse decay method apparatus. Ideally, the volumes of upstream and downstream cylinders should be equal. In this case, as the gas travels through the plug sample, a pressure decrease in the upstream would be equal to the pressure increase in the downstream cylinder, and the mean pressure of the sample would remain constant. If the two cylinders have different volumes, the mathematical solution of the pulse decay becomes more complicated. Brace et al. (1968) proposed the **Eq. 1-6** for the pulse decay method.

$$\frac{\partial^2 P}{\partial x^2} = \left(\frac{\mu c_f}{k}\right)\left[\frac{c_b - c_r}{c_f} + \emptyset\left(1 - \frac{c_r}{c_f}\right)\right]\left(\frac{\partial P}{\partial t}\right) \tag{1-6}$$

where c_b is the compressibility of the bulk rock, c_r is the compressibility of the rock solid, c_f is the compressibility of the fluid, and $\emptyset$ is the porosity of the sample. He proposed a simple solution, as shown in **Eq. 1-7**, by making a simplifying assumption that the storage in the sample is negligible ($\emptyset = 0$).

$$\left(P_u - P_f\right) = \Delta P_0 \left[\frac{V_d}{V_d + V_u}\right] e^{-\alpha t} \tag{1-7}$$

where P_f is the final equilibrium pressure that upstream and downstream pressure eventually approach; ΔP_0 is the initial step change in upstream pressure; V_u and V_d are the volumes of the upstream and downstream gas storage reservoirs, respectively; t is time; and α is the slope of the decay curve in the semi-logarithmic plot which is defined as:

$$\alpha = \left(\frac{kA}{\mu c_f L}\right)\left(\frac{1}{V_d} + \frac{1}{V_u}\right) \tag{1-8}$$

Permeability can be calculated from the slope presented in Eq. 1-8.

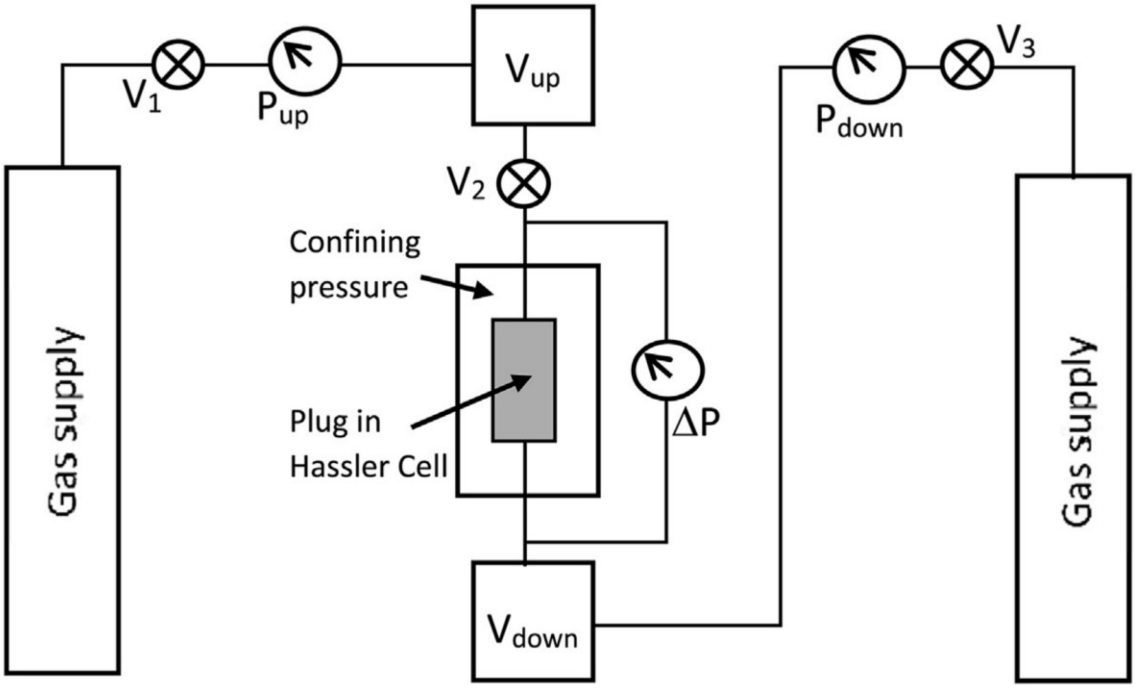

Figure 1-3: Schematic of the setup of pulse decay experiment (Sander et al. 2017).

The GRI method is a special case of the pulse decay method where the downstream cylinder is removed, and the outlet of the plug is opened to the atmosphere.

1.2.3 Uncertainty Analysis: This section presents an evaluation of the uncertainties produced by measuring instruments and equipment in permeability determination using the steady-state method. Permeability is not measured directly but calculated using several other measured parameters. So, the measurement is subject to uncertainties coming from different sources. Four major classes could be considered for sources of uncertainties: 1. Instrument uncertainties: which include viscometer, flowmeter, pressure gauges, caliper, and ruler. 2. Material uncertainties: including heterogeneity in plug sample or air trapping and partially saturating the plug before running the test. 3. Environmental uncertainties: such as fluctuations in ambient pressure and temperature. 4. Human-factor-related uncertainties: It is always present but can be minimized by proper training and a systematic procedure for doing the tests.

1.3 Immiscible Two-Phase Displacement

When water displaces oil during the leak-off or when oil pushes out the water during the flowback, two immiscible fluids move simultaneously inside the porous medium. Buckley and Leverett (1942) proposed the frontal advance model to predict the displacement performance during immiscible displacement. They applied the continuity equation to two phases of oil and water. Four assumptions were made in Buckley-Leverett model:

- Incompressible flow
- Fractional flow of water is a function only of the water saturation
- No mass transfer between phases
- The rock is homogenous (Green and Willhite 1998).

Eq. 1-9 is the Buckley-Leverett equation or frontal advance equation.

$$\left.\frac{dx}{dt}\right|_{S_w} = \frac{Q_i}{A\emptyset}\left.\frac{df_w}{dS_w}\right| \tag{1-9}$$

Where

x distance from the origin,

t time,

S_w water saturation,

Q_i injection rate,

A cross-section area,

ϕ porosity,

f_w water fractional flow.

Buckley-Leverett equation states that in a linear displacement process, each water saturation moves through the porous rock at a constant velocity that can be computed from the derivative of the fractional flow with respect to water saturation. The location of any saturation can be obtained by integrating Eq. 1-9 with respect to time.

Welge (1952) implemented a graphical method for solving the frontal advance equation. His aim was to calculate the average water saturation in the plug as the flood progressed during the water flooding process. The main interest in displacement calculation is when water first breaks through at the producing end of the core plug ($x = L$). The first step in applying the method is constructing the fractional flow relationship using **Eq. 1-10**.

$$f_w = \frac{1}{1 + \left(\frac{k_{ro}}{k_{rw}}\right)\left(\frac{\mu_w}{\mu_o}\right)} \tag{1-10}$$

An example of a water fractional flow curve is shown in **Figure 1-4**. A tangent to the fractional flow curve that originates from S_{wi} is drawn. The point of tangency defines the flood front saturation S_{wf}. Extending the tangent to intersect the line $f_w = 1$ gives the average water saturation in the plug at breakthrough.

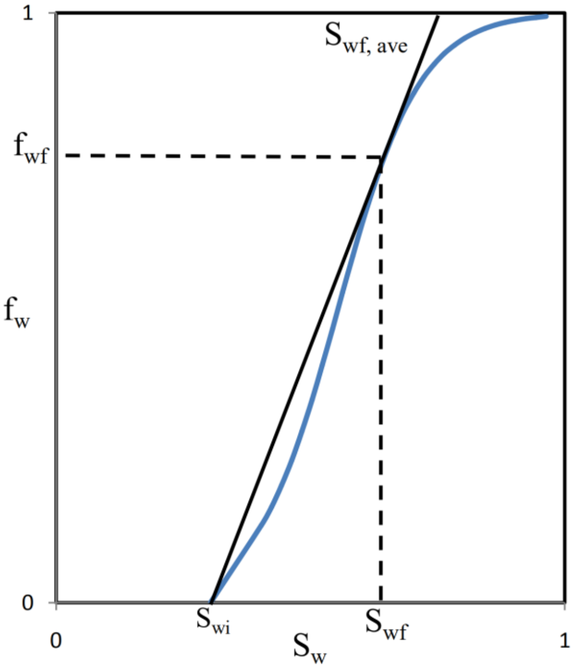

Figure 1-4: An example of a fractional flow curve.

In the Buckley-Leverett solution, it is assumed that all the saturations less than S_{wf} move at the velocity of the flood front. Saturations greater than S_{wf} move at velocities computed from Eq. 1-9.

There are two basic methods for relative permeability measurement: steady-state and unsteady-state methods. The most reliable method is the steady-state method. In this method, two fluids are injected simultaneously at constant flowrates for a while to let the pressure become stable. Using the Darcy equation, the effective permeability of each phase can be calculated at a specific saturation. By changing the ratio of the two phases flowrates, a wide range of saturations can be achieved in the core plug. The limitation of the steady-state method is the inherent time-consuming nature of this method. In the unsteady state method, one fluid displaces the other while pressure drop and fluids productions are recorded. Individual relative permeabilities can be calculated from linear displacement data when the pressure differences across the core sample are measured during displacement at a constant rate. The individual relative permeability can be calculated by application of Welge's equation and JBN method developed by Johnson et al. (1959) or by using a graphical technique developed by Jones and Roszelle (1978). The graphical technique is easier to use and is the industry-accepted procedure. When a displacement is conducted at a constant injection rate, at any instant of time, the total pressure drop is related to fluid and rock properties by Eq. 1-11:

$$\Delta p = -\int_0^L \frac{\frac{Q_i}{A}}{k_b\left(\frac{k_{ro}}{\mu_o}+\frac{k_{rw}}{\mu_w}\right)}dx \tag{1-11}$$

where k_b is the base permeability for the relative permeability data.

Defining the effective or apparent viscosity and the average apparent viscosity with Eq. 1-12 and 1-13:

$$\lambda_r^{-1} = \left(\frac{k_{ro}}{\mu_o}+\frac{k_{rw}}{\mu_w}\right)^{-1} \tag{1-12}$$

$$\overline{\lambda^{-1}} = \frac{\int_0^x \lambda_r^{-1}dx}{\int_0^x dx} \tag{1-13}$$

By integrating Eq. 1-11 and using Eq. 1-13, at the outlet end of the core (point2):

$$\overline{\lambda^{-1}} = \frac{k_b A \Delta p}{Q_i L} \qquad (1\text{-}14)$$

Computation of individual relative permeabilities requires values of the apparent viscosity at the S_{w2}. Thus, k_{rw} and k_{ro} can be calculated from Eq. 1-15 and 1-16:

$$k_{rw} = \frac{\mu_w f_{w2}}{\lambda_2^{-1}} \qquad (1\text{-}15)$$

Where λ_2^{-1} is the apparent viscosity at the outlet end of the core sample. Only the average apparent viscosity is determined from experimental data. Jones and Roszelle (1978) developed a relationship between $\overline{\lambda^{-1}}$and $\lambda_2^{-1}$to compute values of λ_2^{-1}. They showed that drawn tangents to the graph of $\overline{\lambda^{-1}}$ versus Q_i intersect the $Q_i = 0$ at λ_2^{-1}. Thus, it is necessary to express $\overline{\lambda^{-1}}$ versus Q_i.

1.4 Chemical Enhanced Oil Recovery

The economical oil recovery from conventional oil reservoirs, which takes place by primary and secondary processes, is around 30% of the initial oil in place. This number for unconventional tight and shale reservoirs is less than 10%. In conventional reservoirs, different methods have been introduced to improve the oil recovery of the reservoirs and reduce the residual oil saturation that remained in the reservoir rock. Chemical methods and in particular surfactant flooding is one of the promising methods that has been successfully tested in different field trials. In unconventional reservoirs, chemical additives such as surfactant solutions are used for fracture treatment during hydraulic fracturing job to reduce the water trapping and increase the imbibition oil recovery. The rationale behind using surfactants in fracturing fluid is to reduce the capillary pressure of the system (Mirchi et al. 2015). The capillary pressure calculated using Young–Laplace equation (**Eq. 1-16)**, is responsible for holding oil and water in the pore space.

$$P_c = \frac{2\gamma_{ow} \cos\theta_{ow}}{r} \qquad (1\text{-}16)$$

Surfactants in fracturing fluid tend to accumulate at the interface of liquid-liquid and solid-liquid to reduce the interfacial tension and alter wettability to reduce the capillary pressure. However, the adsorption of surfactant on rock surface can result in loss of surfactant concentration, reducing the surfactant's efficiency. Consequently, it can make the treatment non-feasible by increasing the cost of surfactant base EOR processes.

1.4.1 Definition of Surfactants: Surfactants (surface active agents) are a class of chemicals that tend to concentrate at the interface. They are usually organic compounds with a hydrophilic polar head and a hydrophobic non-polar tail. There are four distinct classifications of surfactants based on the surface charge of the hydrophilic head: non-ionic (without any charge), anionic (carrying negative charge), cationic (carrying positive charge), and zwitterionic (carrying both negative and positive charges) (Massarweh and Abushaikha 2020). An important characteristic of a surfactant is the hydrophile-lipophile balance (HLB). The HLB is a number from 0 to 20, which shows the relative tendency of the surfactant to dissolve in oil or water. An HLB of 0 means a completely hydrophobic (lipophilic) molecule, while an HLB of 20 correlates with a very strong hydrophilic molecule. Micelle refers to the aggregate form of surfactant molecules in a solution (Massarweh and Abushaikha 2020). Critical micelle concentration (CMC) is a concentration above which surfactant molecules start to form micelle structures. Above the CMC, the surface tension does not reduce more by increasing the surfactant concentration. A knowledge of CMC is essential because CMC is the limiting concentration for meaningful use.

1.4.2 Surfactant Adsorption: Surfactant retention in porous media is one of the critical phenomena that can affect the economics of surfactant usage for EOR purposes. The main reason for surfactant retention is the adsorption on the surface of the rock. The adsorption process decreases the surfactant concentration in the solution and hence, reduces the effectiveness of surfactant in IFT reduction (Kamal et al. 2017). In oil-wet reservoirs, on the other hand, the adsorption might be beneficial in wettability alteration. The hydrophobic tail of the surfactant would attach to the rock surface, and the hydrophilic head is in contact with the solution. It will prevent further interaction of the oil phase with the rock surface. Therefore, the wettability of the rock changes to water wet. However, excessive surfactant adsorption can reduce the surfactant concentration in the solution and adversely impact the efficiency of the surfactant for the EOR purposes (Saxena et al. 2019). Surfactant structure determines the adsorption of surfactant on the rock surface. In general, anionic surfactant adsorption is higher on carbonate rocks with positive surface charges. Adsorption of cationic surfactants is also higher on sandstone rocks with negative surface charges.

1.5 Research Motivation

Here, we want to answer a simple but crucial question about why the steady-state method of permeability measurement in tight rocks is time-consuming. Knowing the answer can lead us to a faster method for the characterization of tight rocks. Based on the diffusivity equation, the duration of the transient period before reaching the steady-state condition depends on fluid viscosity (μ), rock and fluid compressibility (c), porosity ($\emptyset$), and rock permeability (k):

$$P_t = aP_{xx} + b(P_x)^2 \tag{1-17}$$

Here, $a = \frac{k}{\mu c \emptyset}$ and $b = \frac{k}{\mu \emptyset}$ where P_t and P_x are the first derivative of pressure with respect to time and space, respectively. P_{xx} is the second derivative of pressure with respect to space. The derivation of the diffusivity equation is shown in **Appendix A**.

Since the permeability of tight plugs is very low, the common perception is that the duration of the transient period is long and makes the steady-state method impractical (Cui et al. 2009; Hsieh et al. 1981). Yuan et al. (2021) measured the permeability of tight rock samples from the Montney Formation using a conventional core flooding device. They waited about 200 hours for each flowrate to reach steady-state conditions for a rock with micro-Darcy permeability. To model their experiments, we solve the diffusivity equation with corresponding initial and boundary conditions. A semi-analytical solution of the diffusivity equation (Eq. 1-17) is presented in Appendix B. Odeh and Babu (1988) presented a solution for a similar problem. **Figure 1-5** compares the modeled and measured results and shows a significant difference in the time required to reach steady-state conditions while matching the stabilized pressure values. The modeled pressure is stabilized 600 times faster than the measured one at the same flowrate. Based on the model results, low permeability is not the main reason the steady-state method is time-consuming.

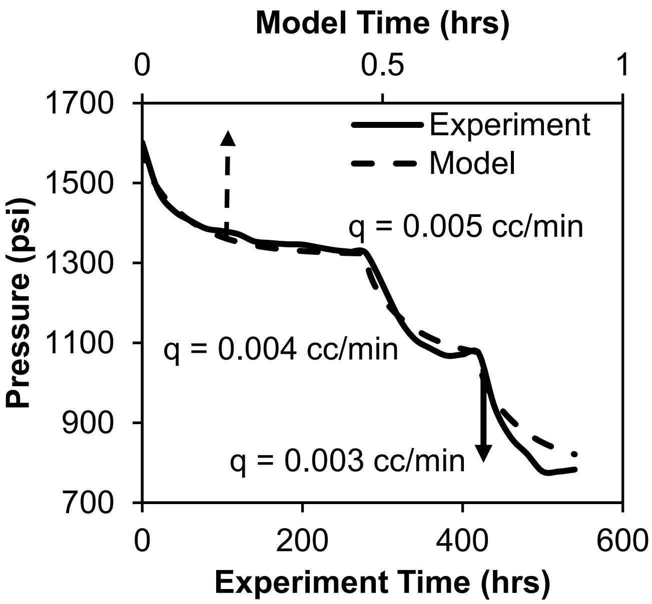

Figure 1-5: Comparison of the time required to reach steady-state condition between the model presented in appendix B and experiment results from Yuan et al. (2021).

1.6 Research Objectives

The main objectives of this research are:

- Proposing a mathematical model with modified initial and boundary conditions to capture the effect of compressibility-induced flow rate on the time scale of liquid permeability measurement of tight rocks.
- Designing a new experimental apparatus based on the proposed model results to validate the model results and reduce the time span of liquid permeability measurement in tight porous media.
- Proposing a mathematical model to explain the observed pressure hump during the two-phase immiscible displacement process in a plug sample. Using the proposed model to come up with a practical technique to determine the relative permeability of tight rock samples.
- Proposing a laboratory protocol to simulate leak-off and flowback processes to study the effect of different fracturing fluid additives on regained permeability.

1.7 Organization of Thesis

This work is divided into 5 chapters. Chapters 1 and 5 are the “General Introduction” and “Conclusions and Recommendations”.

Chapter 1 gives a general introduction and literature review on unconventional resources, permeability measurement methods, immiscible two-phase displacement process, and chemical EOR method.

Chapter 2 is about a model and measurement technique for liquid permeability of tight porous media based on the steady-state method. Some modifications are done on the Initial and Boundary conditions of the diffusivity equation based on an analogy from well testing. A semi-analytical solution is proposed that can model experimental data. Based on the lesson learned from the modeling, the conventional coreflooding device is modified to measure the tight rock permeabilities much faster than the conventional steady-state method.

Chapter 3 is about the modeling of two-phase flow in tight rocks. A mathematical model is developed to model the observed hump in the pressure profile during immiscible displacement. The developed model is used to calculate the relative permeability of the tight rock sample. The calculated relative permeability is used to tune the modified Brooks and Corey relative permeability model.

Chapter 4 is about a laboratory protocol that mimics the leak-off and flowback processes to evaluate the effectiveness of surfactant solutions in fracturing fluid on regained permeability. The chance of formation damage by surfactant particles blockage is also investigated using the particle size distribution of the structures in surfactant solution.

Chapter 5 provides key conclusions from this thesis and proposes recommendations for future studies.

The references from all chapters are combined and presented after Chapter 5. Appendices are presented after the references.

Chapter 2

A Model and Measurement Technique for Liquid Permeability of Tight Porous Media Based on the Steady State Method

2.1 Introduction

Characterization of fluid flow through tight formations is imperative for studies related to carbon capture utilization and storage (Xiao et al. 2020), hydrogen storage (Zivar et al. 2021), radioactive waste disposal (Scheer et al. 2021), geothermal energy recovery (Eggertsson et al. 2020), and oil and gas production from unconventional reservoirs (Sander et al. 2017). Characterizing petrophysical properties, in particular permeability, of tight and shale rock samples is important for long-term production forecast and optimizing completion design. Although permeability is an intrinsic rock property, previous studies show that type of working fluid used for testing influences the value of measured permeability (Dong et al. 2012; Wasaki and Akkutlu 2015). In the case of tight rocks, even Klinkenberg-corrected permeability is one to three orders of magnitude greater than the liquid permeability. A second-order correction is proposed to capture the flow behavior of gas in low-permeability media (Y. Chen et al. 2021). Besides the inconsistency between liquid permeability and corrected gas permeability, the results can also be affected by the type of gas used for the measurement. The gas adsorbs on the rock surface and causes rock swelling and permeability alteration (Day et al. 2012). The extent of permeability change depends on the type of gas used for the measurement. Coal is known to swell as gasses like CO2 or methane adsorb on its surface. Wang et al. (2010) reported 26% decrease of coal permeability after 4 days of methane adsorption. They reported 56% decrease in permeability in case CO2 adsorbed on the coal surface. For shale and tight rocks, permeability measurement is time consuming and needs accurate devices, making the choice of experimental method important. A comprehensive review of steady-state and transient methods for measuring permeability of tight rocks were presented by Sander et al. (2017) and Gensterblum et al. (2015). The steady-state method has been found to be accurate and reliable due to the simplicity of its experimental set-up and analytical solution (Boulin et al. 2012; Sinha et al. 2013; Amann-Hildenbrand et al. 2013; K. Wang et al. 2017). It can be accomplished by applying a constant pressure drop across a plug and measuring stabilized flowrate or injecting the working fluid at constant flowrate and measuring the stabilized pressure drop across the plug. Darcy's law can then be used to calculate the plug permeability. However, application of the steady-state method for tight rocks permeability measurement is challenging. If a constant pressure drop is applied across the plug, precise detection of small changes in flowrates is required. Since measurement error of flowmeters is much greater than the magnitude of fluctuations of low flowrates associated with tight rocks, practically it is not feasible to use the constant pressure mode of injection and measure the effluent flow rate unless a very accurate liquid flowmeter is available. On the other hand, when constant flowrate mode is applied for permeability measurement, it takes too long to arrive at equilibrium pressure (Hsieh et al. 1981; Cui et al. 2009; Metwally and Sondergeld 2011; Winhausen et al. 2021). Lasswell (2013) reported that 6 to 8 weeks is required until a reasonable flow equilibrium is achieved when a light oil is used for measurement of permeability in the range of nano-Darcy. Jones and Meredith (1998), Morrow and Lockner (1997), and El-Dieb and Hooton (1995) measured permeability of tight rocks in the range of nano-Darcy in 15 to 160 hours by applying only one pressure gradient across the sample. In all these studies, the core permeability is calculated based on only one flowrate value.

Due to time-consuming nature of steady-state method, transient techniques are often used for measuring permeability of tight rocks (Cui and Nassichuk 2018). Pulse-decay technique, which is a transient method, appears to be the most common method to measure permeability of tight rocks (Cao et al. 2016). Various analytical solutions have been proposed for calculating permeability using the measured pulse-decay data that may lead to non-unique results(Hsieh et al. 1981; Cui et al. 2009; Brace et al. 1968; Lin 1977; Dicker and Smits 1988; Jones 1997; Tinni et al. 2012). This method is also very sensitive to fluid leakage and temperature fluctuations(Sander et al. 2017; Jones and Meredith 1998). In addition, Lyu et al. (2020) and Sander et al. (2017) stated that the pulse-decay method may overestimate permeability compared to the steady-state method. Rushing et al. (2004) investigated the reason behind this discrepancy and concluded that this might be related to fundamental problems with the unsteady-state methodology. The errors might be either mechanical, numerical, or both.

In this work, we investigate the reason why the steady-state method using the conventional coreflooding apparatus is time consuming, and how it can be modified to be practical for measuring permeability of tight rocks. We also investigate why the diffusivity equation cannot predict the long time required to achieve steady-state conditions in laboratory permeability measurements. Then, we use an analogy from well testing methods to come up with a solution for the diffusivity equation that matches the experimental data. After that, we include the effect of pressure dependency of permeability on pressure profile. Based on findings of the proposed mathematical model, we modify the conventional core flooding device to measure permeability of tight rocks significantly faster than the conventional methods in a time span comparable with transient methods. To avoid all the mentioned complexities of using gas for permeability measurement, we use dead oil for all the measurements. A sensitivity analysis is also performed to investigate the effect of different parameters on the time span of the experiments and to find the most practical way to reduce the steady-state time. The modified device is used to measure the permeability of a tight rock sample and the model can match the measured data with a very good accuracy.

2.2 Why is the steady-state method time consuming?

Based on the diffusivity equation, duration of the transient period before reaching the steady-state condition depends on fluid viscosity (μ), fluid compressibility (c), porosity ($\emptyset$), and rock permeability (k):

$$P_t = aP_{xx} + b(P_x)^2 \qquad (2\text{-}1)$$

Here, $a = \frac{k}{\mu c \emptyset}$, $= \frac{k\acute{c}}{\mu c \emptyset}$, and $\acute{c} = c + \frac{1}{k}\left(\frac{\partial k}{\partial P}\right)$ where P_t and P_x are the first derivative of pressure with respect to time and space, respectively. P_{xx} is the second derivative of pressure with respect to space and $\acute{c}$ is the pseudo-compressibility. Here, rock compressibility (c_r) is considered negligible. When permeability is changing with pressure, a pseudo-compressibility term can be defined which is a function of compressibility and a term corresponding to the change of permeability with pressure. Derivation of general diffusivity equation with pseudo-compressibility term ($\acute{c}$) is shown in **Appendix A**.

Since permeability of tight plugs is very low, the common perception is that the duration of transient period is long and makes the steady-state method impractical (Hsieh et al. 1981; Cui et al. 2009). Yuan et al. (2021) measured permeability of tight rock samples from the Montney Formation using a conventional core flooding device. They waited around 200 hours for each flowrate to reach steady-state conditions for a rock with 1.79 microdarcy permeability. To model their experiments, we solve the diffusivity equation with corresponding initial and boundary conditions. A semi-analytical solution of the diffusivity equation (**Eq. 2-1**) is presented in **Appendix B**. Odeh and Babu (1988) presented a solution for a similar problem. **Figure 2-1a** compares the modelled and measured results and shows a significant discrepancy in the time required to reach steady-state conditions while matching the stabilized pressure values. The upper horizontal axis shows the model time span which took only 1 hour while the lower horizontal axis shows the experiment time of 600 hours. The modeled pressure is stabilized 600 times faster than the measured one at similar flowrate steps. Based on the model results, low permeability is not the main reason why the steady-state method is time consuming. The target is to have a model that could match the time span of the experiment as shown in **Figure 2-1b**.

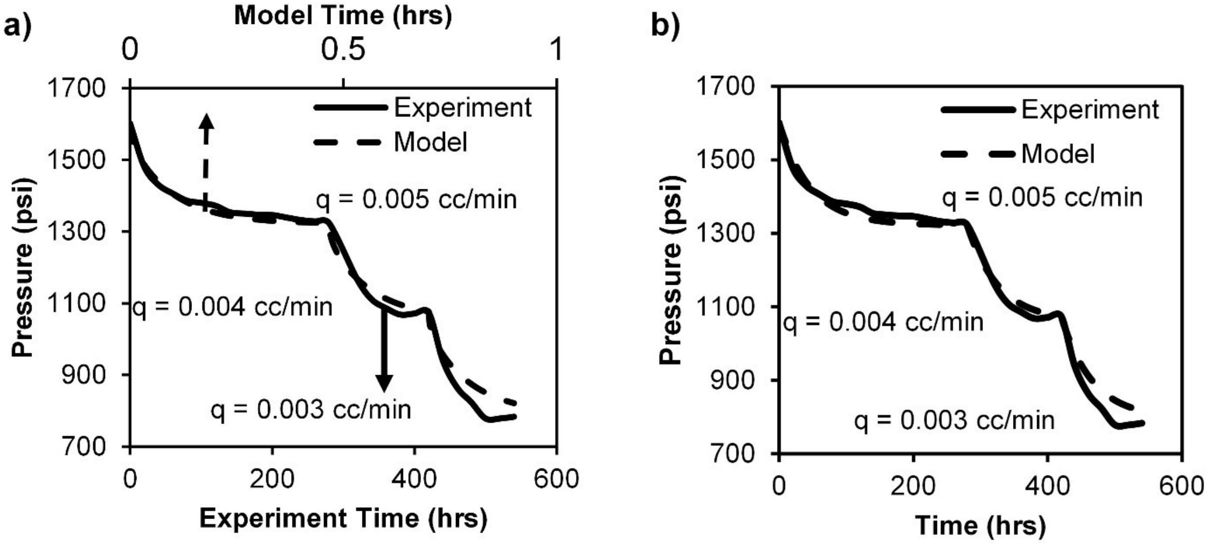

Figure 2-1: a) Comparison of the time required to reach steady-state condition between the model presented in appendix B and experiment results from Yuan et al. (2021). b) The pressure profile modelled using Eq. 2-4 with modified inlet boundary condition matches the pressure profile measured by Yuan et al. (2021).

To explain the difference in time scale between the modelled and measured pressure profiles, we use an analogy from well testing. When a well is open to flow or when it is shut in, the sand-face flowrate is not equal to surface flowrate. It takes some time for these two flowrates to become equal because of wellbore storage effect (Spivey and Lee 2013). The wellbore storage effect will cause a delay in the reservoir response that can be seen as a period during which surface and sand-face flowrates are not equal. The smaller the wellbore storage effect, the faster these two flowrates become equal. **Figure 2-2** shows a general schematic of the conventional coreflooding apparatus.

The injection fluid is inside an accumulator vessel and is pumped at a constant flowrate into the porous medium. The influx flowrate into the plug is lower than the pump-induced flowrate due to the accumulator "storage effect", analogous to "wellbore storage effect" in well testing. When injection pressure increases with time, the influx flowrate into the plug is lower than the pump-induced flowrate due to compression of the fluid in accumulator. On the other hand, when injection pressure decreases with time, the influx flowrate into the plug is higher than the pump-induced flowrate due to expansion of the fluid inside the accumulator. It takes some time for the influx flowrate to become equal to the pump-induced flowrate. The time span depends on the volume of accumulator vessel, fluid compressibility, and pump flowrate. This process can be conceptualized by considering a time-dependent (compressibility-induced) flowrate acting in parallel with the pump-induced flowrate:

$$c = -\frac{1}{V}\frac{\partial V}{\partial P} \Rightarrow q_{ind} = -cV\frac{\partial P}{\partial t} \tag{2-2}$$

Here, q_{ind} is compressibility-induced flowrate and V is accumulator volume.

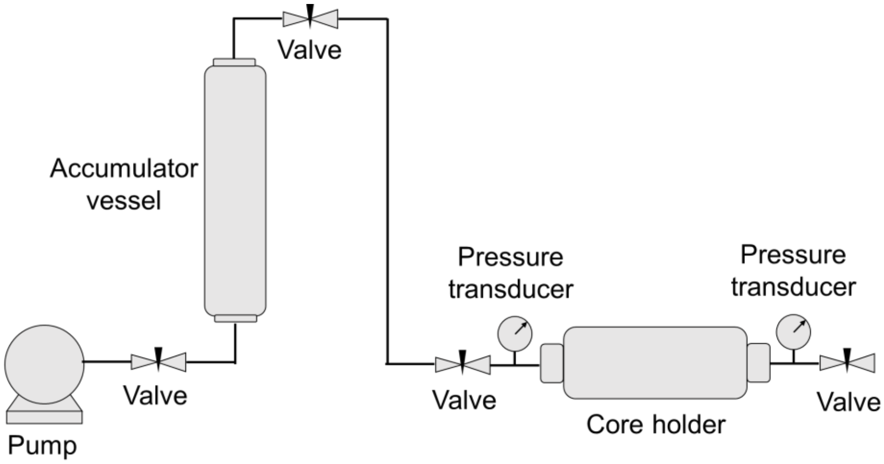

Figure 2-2: Schematic diagram of the conventional coreflooding apparatus.

During permeability measurement of conventional plugs using the core flooding apparatus, we deal with relatively low pressure drop and high flowrate values. Therefore, this compressibility-induced flowrate in upstream accumulator vessel is relatively lower than the pump flowrate and can be neglected. On the other hand, when dealing with low-permeability tight rocks, the compressibility-induced flowrate could be in the order of pump flowrate and cannot be neglected. To quantify the percentage of flowrate that is attributed to storage effect, we consider four equal-sized plugs with permeabilities of 1 microdarcy (μD) to 1 millidarcy (mD). The accumulator used for permeability measurement has 500 cc volume filled with a fluid with compressibility of 2×10^{-5} psi^{-1}. After half an hour injection with flowrate of 0.003 cc/min, the ratio of compressibility-induced flowrate to pump-induced flowrate is 0.3% and 99.2% for the 1 mD and 1 μD plugs, respectively. After 1 hour, the compressibility-induced flowrate totally vanishes for the 1 mD plug but only reduces to 98.6% for the 1 μD plug. **Figure 2-3** shows how quickly storage effect vanishes for different cases of permeabilities. Therefore, the main reason why the steady-state method is time consuming is that the influx flowrate into the porous medium is not constant and changes with time. **Eq. 2-2** shows the variable part of the influx flowrate which depends on the injection pressure. To validate this hypothesis, we build a mathematical model with modified boundary conditions to match the experimental results.

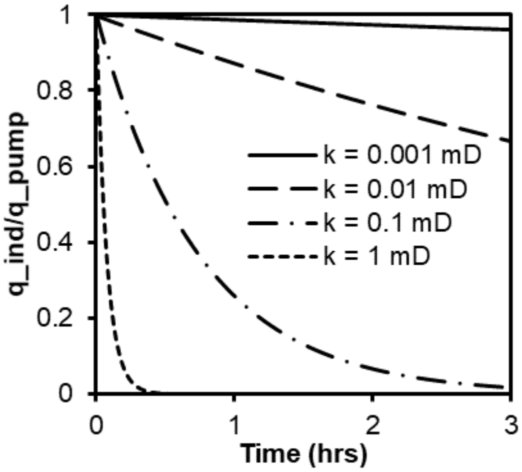

Figure 2-3: Ratio of compressibility-induced flowrate to pump-induced flowrate versus time at four different permeabilities.

2.3 Mathematical model

To model the pressure profile, we combine the continuity equation with Darcy law to arrive at the 1-D diffusivity equation for a porous medium (Eq. 2-1) (Spivey and Lee 2013; Dejam et al. 2017). We assume fluid compressibility and viscosity are constant. Since this model is used for tight rocks, the pressure gradient, P_x along the plug is not small, and thus, $(P_x)^2$ term in the diffusivity equation is not negligible. For now, it is assumed that permeability is constant with pressure, and thus, $\acute{c} = c$. Later, we will consider the permeability variation due to net overburden pressure change along the core. To solve Eq. 2-1, we need one initial condition and two boundary conditions.

2.3.1 Initial Condition: Based on experimental conditions and the implemented procedure, the initial condition might be the constant atmospheric pressure along the plug, or an established pressure profile along the plug when a steady-state flow has been fully developed. In previous studies (Hsieh et al. 1981; Odeh and Babu 1988; Dejam et al. 2017; Haskett et al. 1988) the initial condition is considered to be a constant pressure along the plug. In this study, since we change the flowrate after reaching steady-state condition, the initial condition for the second flowrate would not be a constant pressure along the plug. Solving the conventional diffusivity equation, where $(P_x)^2$ is negligible, gives a linear pressure profile along the plug at fully developed steady-state conditions. Here, we consider $(P_x)^2$ is not negligible. Solving the proposed diffusivity equation for tight rocks (Eq. 2-1), gives a logarithmic pressure profile along the plug at steady-state conditions, as explained in **appendix C**.

2.3.2 Boundary Conditions: The outlet boundary is assumed to be at constant atmospheric pressure. For the sake of mathematical simplification, we assume $x = 0$ at the plug outlet and $x = L$ at the inlet. In appendix B, we solve the diffusivity equation with inlet boundary condition of constant flowrate. Odeh and Babu (1988) presented an analytical solution for a similar problem. The results (Figure 2-1a) show a significant discrepancy in time span of the measured and modelled pressure profiles. Based on the previous discussions, although the pump injects the fluid at a constant flowrate, the influx flowrate into the plug is not constant due to accumulator “storage effect”. To overcome the inconsistency in time span of modelled and measured pressure profiles, we modify the inlet boundary condition as follows:

$$q_{pump} + q_{ind} = \frac{kA}{\mu} P_x \Rightarrow P_x|_{x=L} = \frac{q_{pump} \cdot \mu}{kA} - \frac{cV\mu}{kA} P_t|_{x=L} \tag{2-3}$$

Here, q_{pump} is pump-induced flowrate, q_{ind} is compressibility-induced flowrate, A is rock cross-sectional area, and V is accumulator volume.

A simple 1-D schematic of the proposed model is presented in **Figure 2-4**. Solution of the model presented in Figure 2-4 with the modified boundary condition (Eq. 2-3) in Laplace domain is given by

$$\tilde{U}(x,S) = \frac{w_4 \sinh\left(\sqrt{\frac{S}{a}}x\right)}{S\sqrt{\frac{S}{a}}\cosh(\sqrt{\frac{S}{a}}L) + S(Sw_3 - w_2)\sinh(\sqrt{\frac{S}{a}}L)} \tag{2-4}$$

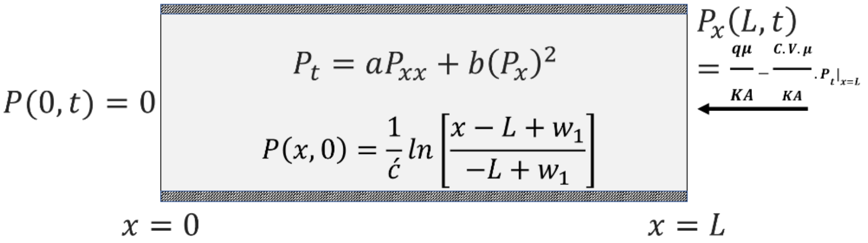

Figure 2-4: 1-D schematic of flow modeling using diffusivity equation with logarithmic initial condition and modified inflow boundary condition considering storage effect.

Definition of the terms used in Eq. 2-4 and mathematical derivations are presented in **Appendix D**. Stehfest's method is used to find the inverse of Laplace transform numerically (Stehfest 1970; Hassanzadeh and Pooladi-Darvish 2007). In previous solutions proposed for diffusivity equation (Hsieh et al. 1981; Odeh and Babu 1988; Walls et al. 1982; Haskett et al. 1988), logarithmic pressure profile as initial condition and pressure-dependent inflow boundary condition are not considered. Figure 2-1b compares the calculated pressure profile using the proposed model at $x = L$ with the one measured by Yuan et al. (2021). First row of **Table 2-1** summarizes the properties of the fluid and plug used in their experiments.

Table 2-1**.** properties of the plugs and fluid samples used for the permeability measurement.

Length (cm)	Area (cm^2)	Porosity (%)	Permeability (μD)	Oil Viscosity (cp)	Oil Compressibility (psi^{-1})	Accumulator Volume (cc)
6.12	11.28	6.14	1.79	3.56	2E-5	500
6.0	10.75	4.60	2.31	3.24	2E-5	10

As shown in Figure 2-1b, the proposed model can reasonably match the pressure versus time profiles. The match for the last injection flowrate (0.003 cc/min) is not as good as those for the other flowrates. The reason is that in each step of flowrate change, we assume that a steady-state regime is established at the previous flowrate, and thus, there is a logarithmic pressure profile along the plug as described in appendix C. However, the model results show that the steady-state condition is not fully established at the second flowrate. Therefore, the assumed initial condition for the last flowrate is not accurate, leading to the observed deviation between the measured and modelled data.

2.3.3 Pressure dependency of permeability: Fundamental relationships have been derived for porosity and permeability as functions of effective stress. Pressure dependency of the permeability has been observed in experimental works with shale rock samples (Akkutlu and Fathi 2012). McKee et al. (1988) presented an exponential relationship between permeability and effective stress as $k = me^{-nP_{nc}}$ where P_{nc} is the net confining pressure. We conducted a series of permeability measurements at different confining pressure (P_{con}) values to determine the parameters m and n of the empirical correlation. **Figure 2-5** shows the measured permeability vs. P_{nc}. P_{nc} is calculated as the difference between confining pressure and average pore pressure when flowrate is 0.001 cc/min. This flowrate is chosen because it was a common flowrate during permeability measurement tests at all different confining pressures.

Here, we assume that the same relationship can be used for permeability change with pressure along the plug. If pressure dependency of permeability is considered in Eq. 2-1, $\acute{c}$ can be modeled by summation of fluid compressibility (c) and the pressure-dependency exponent (n):

$$\acute{c} = c + \frac{1}{k}\left(\frac{\partial k}{\partial P}\right) = c - \frac{1}{k}\left(\frac{\partial k}{\partial P_{nc}}\right) = c + n \tag{2-4}$$

The solution presented in appendix D with the modified $\acute{c}$ value is used for modeling the pressure profile to account for permeability changes with pressure along the plug.

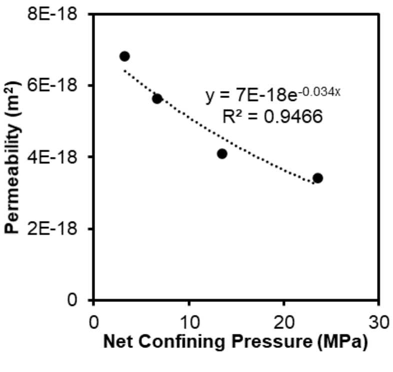

Figure 2-5: Exponential decline of measured permeability with increasing net confining pressure on the plug.

2.3.4 Sensitivity Analysis: Here, a sensitivity analysis is performed to identify the parameters controlling the time required to reach steady-state conditions after changing the inlet flowrate. Compressibility (*c*), accumulator vessel volume (*V*), pressure-dependency exponent (*n*), and permeability (*k*) are investigated for this purpose. **Figure 2-6 a-d** show how these parameters affect the shape of pressure profiles and the time span required to reach steady-state conditions. For the base case in each of the graphs we used $k = 1.79E\text{-}6\ D$, $V = 300\ cm^3$, $n = 0$, and $c = 2E\text{-}5\ psi^{-1}$. Figure 2-6a shows that increasing fluid compressibility does not affect the final stabilized pressure value but increases the time span required to reach the steady-state condition. The same trend is observed by increasing the accumulator volume in Figure 2-6b. Figure 2-6c shows that increasing pressure-dependency exponent increases the stabilized pressure but has no noticeable effect on the time span required to reach the steady-state condition. The same trend is observed for the permeability decline in Figure 2-6d. Therefore, for reducing the time span for the steady-state establishment, it is recommended to use a fluid with less compressibility inside an accumulator with less volume.

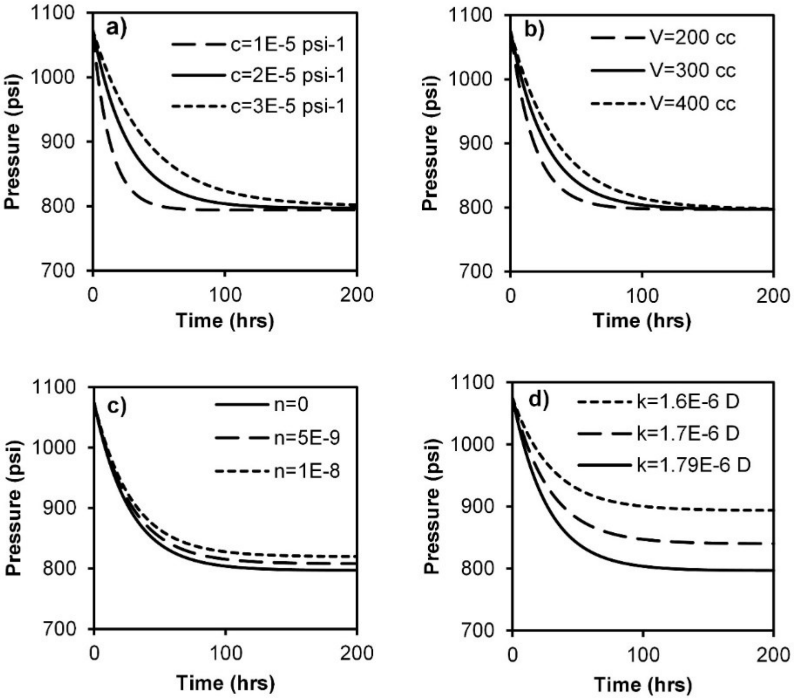

Figure 2-6: Sensitivity analysis to investigate the effects of a) fluid compressibility, b) accumulator vessel volume, c) pressure-dependency exponent, and d) permeability on the shape of pressure profile and time span required to reach steady-state conditions.

2.4 A new design for tight-rock permeability measurement

Modifying boundary conditions of the diffusivity equation enabled us to model the experimental results of Yuan et al. (2021). From the previous section, it is concluded that the accumulator "storage effect" is the main reason why the steady-state method is time consuming. The second term on the right-hand side of the modified boundary condition (Eq. 2-3) shows the parameters that affect the time needed for achieving steady-state conditions. The most practical way to reduce this parameter is to reduce the accumulator volume, V. Although it is possible to use a fluid with less viscosity and compressibility or increase the cross-sectional area of the plug, usually there are restrictions in changing these parameters.

We designed a new core flooding system by 1) decreasing the dead volume inside the core holder, and 2) reducing the accumulator volume by fiftyfold to around 10 cc. We applied the system to measure the permeability of a plug with microdarcy permeability to investigate the effects of the implemented modifications on the time required to achieve steady-state conditions (**Figure 2-7a**). For the case where $n = 0$, a constant permeability is considered for all injection flowrates which is calculated from the slope of the trendline in graph of flowrate vs. pressure drop (**Figure 2-7b**) using Darcy equation. For the case where permeability is considered pressure dependent, a value of $\mathrm{n} = 6.02 \times 10^{-8}$ is used in the model. This value is calculated using the exponential relationship between permeability calculated at each injection flowrate and effective stress calculated at corresponding average pore pressure. Second row of Table 2-1 summarizes the properties of the fluid and plug used in the experiments. Before the permeability measurement test, plug sample was washed with polar and nonpolar solvents and dried in an oven at 90 C. Then, plug was vacuumed for two days from both ends to make sure the air trapped inside pore space is minimized. After that, oil introduced into the sample. The sample kept under 1100 psi for about a week to make sure oil occupies all the accessible pore space. At the final stage of core preparation, 2 to 3 pore volumes of oil were injected to make sure oil displaces any other possible fluids presented inside the pore space. The fluid injection process for permeability measurement is carried out in two parts: In part 1, injection rate increases stepwise and in part 2 it decreases in the same steps. The proposed rate-change pattern allows checking repeatability of the measured pressure data at ultra-low flowrates. The perfect linear correlation in flowrate vs. differential pressure graph (Figure 2-7b) with $R^2 \approx 1$ suggests that oil flow in tight rocks can be described accurately by the Darcy equation. More data regarding the application of modified coreflooding device for permeability measurement of tight rocks can be found in following chapters.

Figure 2-7a shows the results of permeability-measurement test using the modified apparatus on the plug sample with petrophysical properties listed in second row of Table 2-1. Each flowrate change induces a pressure pulse that reaches the steady-state conditions after around 4 hours. Comparing the pressure-time profiles with the previous ones measured by Yuan et al. (2021) shows a fiftyfold decrease in the time required for steady-state establishment. A qualitative investigation of Figure 2-7a shows that when permeability is considered constant, there exists a difference between modeled and measured stabilized pressure at each injection flowrate. At low flowrates, the modeled stabilized pressure value is lower than the measured one. As flowrate increases, the modeled pressure approaches the measured value and finally it exceeds the measured value at high flowrates. This behavior confirms the pressure dependency of permeability. As flowrate increases, the average pore pressure increases, and thus, the net confining pressure decreases. Therefore, at higher flowrates the permeability is higher and thus the measured pressure is lower than the modeled one with the assumption of constant permeability. In order to quantify the goodness of the fit between the modeled and measured pressure profiles, we use mean absolute percentage error (MAPE) and root mean square error (RMSE) measures. In case of constant permeability, MAPE is 4% with RMSE of 10 psi while for the case of pressure-dependent permeability, MAPE is 3% with RMSE of 8.5 psi. Therefore, the assumption of constant permeability does not result in significant errors while making the model much simpler. In case of shale samples, since the pore compressibility is high (Lan et al. 2017), the effect of confining pressure on rock permeability is high. So, assumption of constant permeability along the plug may introduce a greater error compared to the presented case.

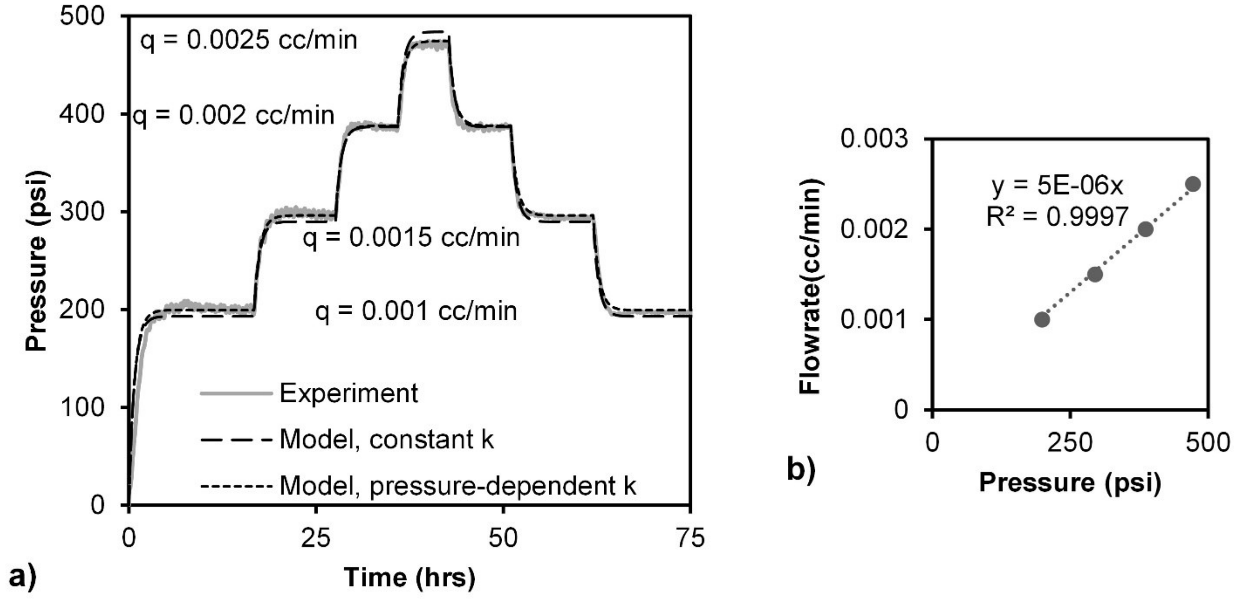

Figure 2-7: a) Measured and modeled pressure profiles during permeability measurement using the new design for tight rocks. Both pressure-dependent and constant permeability assumptions show an accurate prediction of pressure profile. B) Graph of flowrate vs. pressure drop. The slope of linear fit is used for permeability calculation using Darcy equation.

2.5 Implications and significance of the work

Unconventional resources have become an important source of energy because of recent developments in horizontal drilling and multistage hydraulic fracturing. During a hydraulic fracturing operation, a large volume of fracturing water is pumped into the formation and only a small portion of it comes back during flowback and post flowback periods. Imbibition of fracturing fluid into the formation is considered as a driving force for hydrocarbon production from tight rocks (Habibi et al. 2017). On the other hand, imbibition of fracturing fluid forms a water loaded zone near the fracture face that reduces hydrocarbon relative permeability and hinders hydrocarbon production (Bennion et al. 1996). To enhance imbibition oil recovery and reduce water trapping near fracture face, chemical additives such as surfactants are used in the fracturing fluid. To investigate the effectiveness of such chemicals, we must measure the permeability of the medium before leak-off and after flowback processes. It is not practical to use transient methods for this purpose since the measurement method should be part of the process. Transient methods usually use gas for measurement that limit their application for this purpose. Since permeability measurement of tight rocks with conventional steady-state methods is challenging and time consuming, researchers usually use relatively high-permeability outcrop samples to study the effects of chemical additives on imbibition oil recovery and water trapping removal (Liang et al. 2017; Yarveicy et al. 2018; Tangirala and Sheng 2019). Those results are not necessarily applicable to tight rocks since the pore structure and wettability of tight rocks are different than the outcrops. Using the modified core flooding device based on proposed model, it is possible to measure the liquid permeability before leak-off and after flowback processes to investigate the effects of chemical additive on regained permeability.

2.6 Summary

In this chapter, we used the diffusivity equation to explain why the steady-state method of permeability measurement is time consuming for low-permeability media. We altered the influx boundary condition to model the measured pressure data during permeability measurement of a tight rock sample with error of less than 5%. Based on the model results, we modified the conventional coreflooding device to reduce the time of permeability measurement of tight rock samples. The modified device is used to measure the permeability of a tight rock sample and the model can match the measured data with a very good accuracy. Here is the summary of the key findings:

- A new semi-analytical solution for diffusivity equation is presented which accounts for logarithmic pressure profile as initial condition, storage effect, pressure dependency of permeability, and high-pressure drawdown values in case of experiments done on low-permeability porous media.
- A device for permeability measurement of tight rocks is designed by modifying conventional coreflooding apparatus. The tests conducted using the modified device confirm the modeling results and shows a considerable decrease in time of experiments.
- The main reason that makes the steady-state method time consuming is the accumulator “storage effect”. When injection pressure increases (or decreases) with time, compaction (or expansion) of the fluid inside the accumulator induces an excess flowrate that causes the influx flowrate into the plug to be lower (or higher) than the pump-induced flowrate. It takes some time for the influx flowrate to become equal to the pump-induced flowrate.
- When dealing with low-permeability tight rocks, the compressibility-induced flowrate could be in the order of pump flowrate and cannot be neglected.

- Ignoring the pressure dependency of the rock permeability does not result in significant errors in the model while making the model much simpler.
- In the modified coreflooding device, reduction of accumulator volume from 500 cc to around 10 cc causes a fiftyfold decrease in the time required for steady state establishment.

Chapter 3

Modeling Two-Phase Flow in Tight Core Plugs with an Application for Relative Permeability Measurement

3.1 Introduction

The study of two-phase flow is important in many different engineering disciplines including petroleum engineering (Li and Horne 2006), hydrology (Li and Yu 2020), chemical engineering (Noël et al. 2019), carbon capture utilization and storage (Xiao et al. 2020), hydrogen storage (Zivar et al. 2021), radioactive waste disposal (Scheer et al. 2021), and geothermal energy recovery (Eggertsson et al. 2020). Modeling of immiscible two-phase flow is a challenging physical problem that has been studied by numerous researchers. The complexity of this problem comes from the multi-scale nature and nonlinearity of its governing equations. In micro-scale, rock and fluid interactions, the roughness of the pore walls, and the wetting affinity of the minerals covering the pore walls are important factors. In meso-scale, pore size distribution and capillary pressure are two dominant parameters. In macro-scale, uncertainty in permeability, heterogeneity, and geometry of the reservoir cast doubt on predictions based on the general equation of immiscible two-phase flow (Doster and Hilfer 2011).

The general equation governing two-phase immiscible displacement can be derived by combining the Darcy equation for each phase with the continuity equation and relating the pressure of the two phases by capillary pressure as shown in **Appendix E** (Peters 2006). This results in a second-order, nonlinear, parabolic partial differential equation that can be solved numerically using specific assumptions. To calculate the oil recovery from the general equation of two-phase immiscible displacement, constitutional relationships for capillary pressure and relative permeabilities are needed. Since measurement of these relationships is time-consuming and challenging, researchers measure the oil recovery versus time in laboratory experiments and use the two-phase flow equation to calculate capillary pressure and relative permeability values (Pini and Benson 2013). Buckley and Leverett (1942) dropped the capillary pressure term from the general equation and simplified it to a first-order parabolic partial differential equation. Welge (1952) extended their work and presented a simple but useful analytical tool to calculate oil recovery and the ratio of relative permeabilities (k_r) during an immiscible displacement experiment. Johnson et al. (1959) presented the JBN method to calculate individual relative permeabilities in a water flooding experiment on a relatively high-permeability porous medium. Jones and Roszelle (1978) adopted a graphical method based on the works of Johnson et al. (1959) and Welge (1952) to facilitate the calculations for relative permeability determination. Chen et al. (2016) extended the JBN method by adding pressure taps along the core and measuring local fluid saturations using computed tomography scanning. A comprehensive review of methods of k_r measurement can be found in Honarpour et al. (2018)'s book. In these methods, experimental flooding data are required to construct the fractional flow curve and calculate the k_r values. Researchers modified the mentioned methods to account for flowrate dependency of k_r curves (Valavanides et al. 2022), k_r dependence on viscosity ratio and capillary number (Suwandi et al. 2022), and also effects of dual wettability on immiscible displacement (Cha et al. 2022; Yassin et al. 2016). Currently, there is no standard laboratory technique for measuring relative permeability curves of tight and shale rocks due to measurement challenges and the long time needed for flow and pressure equilibration. The flowrate in coreflooding tests on tight rocks is usually in the range of microliter per minute (*µL/min*). Measurement of such low flowrates is erroneous if not impossible especially when two phases are comingled in the effluent. Due to these challenges, researchers tried to use unconventional methods for k_r determination. Alyafei and Blunt (2018) tried to obtain k_r curves using spontaneous imbibition tests. Lin et al. (2018) used imaging techniques to calculate relative permeability values. Ojha et al. (2017) used nitrogen-adsorption/desorption measurements and Peng (2019) used a gas expansion method for k_r measurement.

There are also mathematical approaches to calculating relative permeabilities from capillary pressure data. Purcell (1949) presented a mathematical relationship between permeability and capillary pressure. Burdine (1953) and Brooks and Corey (1966) extended Purcell's work to calculate k_r of each phase. Lake (1989) modified the Brooks and Corey k_r model to include the end-point k_r values in the model formulation. Recent researchers (Su et al. 2022; Standnes et al. 2017; Zhang et al. 2017; Yassin et al. 2016; Schmid et al. 2016) also presented mathematical models to account for dual wettability and nanoscale effects such as slippage and the effect of boundary layer on flow to predict k_r curves. Guler et al. (2003) utilized artificial neural networks to determine relative permeability curves. Lei et al. (2015) established a theoretical model for stress-dependent relative permeability based on fractal theory for porous media. Khorsandi et al. 2017) considered relative permeability as a state function and developed an equation of state to calculate relative permeability including hysteresis and wettability alteration. Schembre-McCabe et al. (2020) used the Lattice-Boltzmann simulation to model relative permeability curves. All these theoretical approaches need experimental data for validation and tuning of their parameters. Due to difficulties associated with testing on low-permeability tight rocks, there is a need for a practical method to measure k_r in such tight porous media to tune the theoretical models of k_r.

In this dissertation, we present a practical method to measure k_r curves of low-permeability tight-rock samples. The pressure profile measured during an immiscible displacement is used with some simplifying assumptions to tune the modified Brooks and Corey (MBC) k_r model presented by Lake (1989). We present a mathematical model based on frontal advance theory to model the pressure drop during a two-phase immiscible displacement at a constant injection flowrate. Several oil/water immiscible displacement tests are performed on tight-rock samples to provide the experimental data required for the proposed technique. At the end, we investigate the shape of the pressure profile during an immiscible displacement from the "flow work" perspective to gain insights for field implications.

3.2 Mathematical Modeling of Pressure Drop during a Two-Phase Immiscible Displacement

In this section, a simple mathematical technique is presented to model the pressure profile during immiscible displacement. We explain the characteristic feature of the pressure profile and investigate the factors affecting the shape of the profile. There are many studies in literature for modeling immiscible two-phase displacement (Lunowa et al. 2021; Pasquier et al. 2017; Tecklenburg et al. 2013; Liu et al. 2012). The JBN method is the most common method used for k_r measurement. In this method, water is injected into the rock sample at a constant flowrate to displace oil. The produced volume of oil and water is measured with time to calculate the effluent flowrates and construct the fractional flow curve. This curve is used for the calculation of k_r curves of oil and water. The pressure drop during the immiscible displacement is calculated using an integral term (Fassihi and Potter 2009; Johnson et al. 1959):

$$\Delta p = \frac{q_t . \mu_o}{k.A} \int_0^L \frac{f_o}{k_{ro}} dx \tag{3-1}$$

Since f_o and k_{ro} depend on the saturation profile which changes along the core length, the calculation of the integral term is not straightforward. Here, we propose a simplifying assumption to make the pressure drop calculation easier. We use values of f_o and k_{ro} at average water saturation ($\overline{S_w}$) behind the front instead of using their values at variable S_w along the core plug:

$$\Delta p = \frac{q_t . \mu_o}{k.A} \int_0^L \frac{f_o}{k_{ro}} dx = \frac{q_t . \mu_o . L}{k.A} . \frac{\overline{f_o}}{\overline{k_{ro}}} \tag{3-2}$$

This should be a reasonable assumption since the JBN method is derived based on the frontal advanced theory which assumes a constant $\overline{S_w}$ behind each saturation front during the immiscible displacement process. This assumption does not imply that the water saturation remains constant behind the front, but rather that the average water saturation behind each front is constant while the front is moving from inlet to outlet. The simplification made here is that, instead of using the integral term to calculate the $\frac{f_o}{k_{ro}}$, which would require knowledge of the water saturation profile along the core plug, the $\frac{f_o}{k_{ro}}$ is calculated at the average water saturation behind the front. Here, we derive a mathematical technique to model the pressure profile before and after breakthrough during the immiscible displacement of oil by water. We use our simplifying assumption that values of f_o and k_{ro} at $\overline{S_w}$ behind the front are constant. This technique can also be used to model the pressure response during a flowback process in which oil displaces the leaked off water in unconventional hydraulically fractured wells (Longoria et al. 2017; Yousefi et al. 2020). **Figure 3-1** shows the pressure profile during waterflooding at a constant flowrate of 0.06 cc/hr for a plug sample with a permeability of around 2 microDarcy saturated with oil at irreducible water saturation (S_{wirr}). The pressure recorded is the injection pressure at the inlet of the core sample, which is also the pressure drop across the plug since the outlet pressure is atmospheric. Details of the experimental work are presented in **Appendix F**. The pressure increases until it reaches the maximum point and declines afterward to stabilize at a final value. A similar pressure profile was also reported in the works of other researchers (Aslanidis et al. 2022; Kalaydjian 1992). The exhibited hump in the pressure profile is modeled here and investigated to find the factors affecting the magnitude of the pressure hump.

Figure 3-2 schematically illustrates the displacement of oil by water in a plug initially saturated with oil at S_{wirr}. For modeling the immiscible displacement of oil by water, we use the fundamental assumptions of frontal advance theory (Welge 1952; Johnson et al. 1952; Buckley and Leverett 1942). At time t before breakthrough time (t_{bt}), the water front is at distance l from the inlet. Behind the front, there is two-phase flow while ahead of it there is single-phase oil flow. The total pressure drop is divided into two parts: from the system inlet to the front, and from the front to the outlet. For the first part, based on the assumptions of the frontal advance theory, $\overline{S_w}$ behind the water front is constant. We use our simplifying assumption here and use **Eq. 3-2** for the calculation of pressure drop in this part. Either the oil or water phase can be used for pressure-drop calculations, but for simplicity, we use the water phase. For the first part from the inlet to the front we have

$$\Delta p_1 = \frac{q_t \overline{f_w} \mu_w l}{\overline{k_{rw}} k A} \tag{3-3}$$

Even though the flow in this section is not steady due to changes in local water saturation, we can still use the Darcy equation to calculate pressure drop because we have assumed a constant average water saturation behind the front. The f_w and k_{rw} terms are determined at this $\overline{\boldsymbol{S_w}}$. For the second part from front to the outlet we have

$$\Delta p_2 = \frac{q_t \mu_o (L - l)}{k_{ro}^{end} k A} \tag{3-4}$$

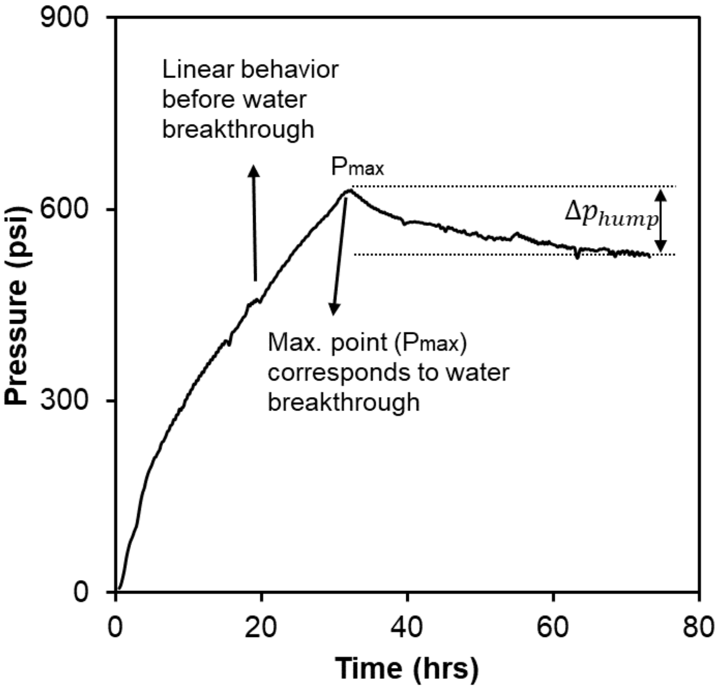

Figure 3-1: Observed hump in the pressure profile during a waterflooding experiment at a constant flowrate of 0.06 cc/hr. The maximum point corresponds to the water breakthrough. Before the breakthrough, the pressure changes linearly. Details of the experiment are mentioned in Appendix B.

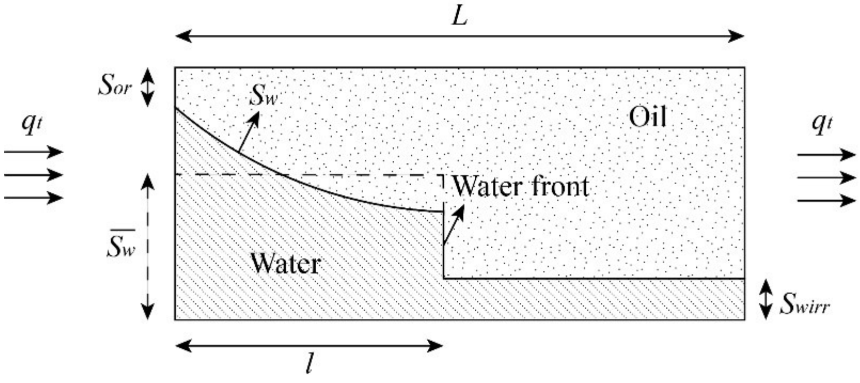

Figure 3-2: Immiscible displacement of oil by water in a plug at a constant injection flowrate.

Substituting $l = \frac{q_t t}{A\emptyset(\overline{S_w} - S_{wirr})}$ into **Eq. 3-3** and **Eq. 3-4** gives

$$\Delta p_1 = \frac{q_t \overline{f_w} \mu_w q_t t}{\overline{k_{rw}} k A^2 \emptyset (\overline{S_w} - S_{wirr})} \tag{3-5}$$

$$\Delta p_2 = \frac{q_t \mu_o L}{k_{ro}^{end} kA} - \frac{{q_t}^2 \mu_o t}{k_{ro}^{end} kA^2 \emptyset(\overline{S_w} - S_{wirr})} \tag{3-6}$$

The total pressure drop is the summation of Δp_1 and Δp_2:

$$\Delta p = \Delta p_1 + \Delta p_2 = \frac{q_t \mu_o L}{k_{ro}^{end} kA} + \frac{{q_t}^2 \mu_o}{kA^2 \emptyset(\overline{S_w} - S_{wirr})}\left[\frac{\mu_w}{\mu_o}\frac{\overline{f_w}}{\overline{k_{rw}}} - \frac{1}{k_{ro}^{end}}\right] \times t \tag{3-7}$$

Here, since we assumed constant saturation in space behind the water front, $\overline{S_w}$, $\overline{f_w}$, and $\overline{k_{rw}}$ are constant for part 1, and Δp is linearly correlated with time. It means Δp increases linearly until *t* reaches t_{bt}. The maximum pressure drop occurs at t_{bt} which is

$$\Delta p = \left.\frac{q_t \mu_w L \overline{f_w}}{kA\overline{k_{rw}}}\right|_{t=t_{bt}} = \left.\frac{q_t L}{kA} \cdot \frac{1}{M_w + M_o}\right|_{t=t_{bt}} \tag{3-8}$$

Eq. 3-8 is used to calculate pressure drop after breakthrough as well. Our simplifying assumption here is to calculate the mobility (k_r/μ) of each phase at constant $\overline{S_w}$ behind each saturation front after breakthrough. **Figure 3-3** shows the modeled pressure drop vs. the number of pore volumes of water injected (*PV-inj*) into a tight plug during an immiscible displacement process. The dashed line is the pressure calculated using Eq. 3-8, and the solid line is the pressure calculated using Eq. 3-1 used in the JBN method. In Figure 3-3a, with a favorable mobility ratio of 1, the mean absolute percentage error (MAPE) is 2.1% compared to MAPE of 6.4% for an unfavorable mobility ratio of 10 shown in Figure 3-3b. Thus, our assumption to use values of water and oil mobilities at the constant $\overline{S_w}$ does not introduce any significant error in the calculated pressure while it helps us to propose a practical method for k_r calculation.

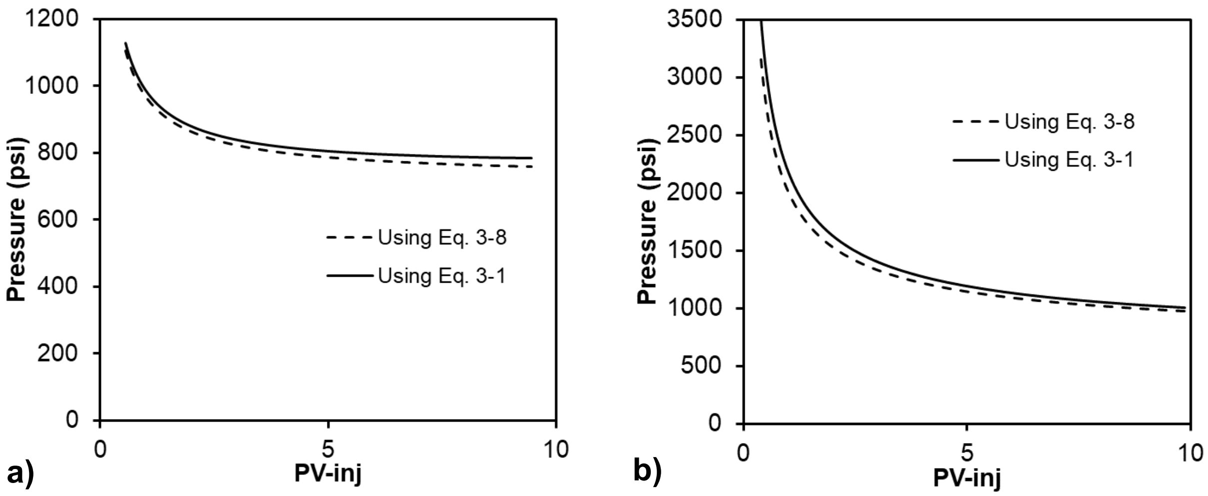

Figure 3-3: a) pressure drop calculated based on Eq. 3-8 compared to the one calculated using Eq. 3-1 for a) mobility ratio = 1, b) mobility ratio = 10.

At the end of water injection when a steady-state condition is achieved and oil saturation (S_o) reaches its residual value (S_{or}), the final pressure drop is $\Delta p = \left.\frac{q_t \mu_w L}{kAk_{rw}^{end}}\right|_{S_{or}}$. The difference between $\Delta p|_{t=t_{bt}}$ and $\Delta p|_{S_{or}}$ is defined as Δp_{hump} as shown in Figure 3-1:

$$\Delta p_{hump} = \Delta p|_{t=t_{bt}} - \Delta p|_{S_{or}} = \left.\frac{q_t \mu_w L f_w}{kAk_{rw}}\right|_{t=t_{bt}} - \left.\frac{q_t \mu_w L}{kAk_{rw}^{end}}\right|_{S_{or}} \tag{3-9}$$

Substituting $f_w = \frac{1}{1+\frac{k_{ro}\,\mu_w}{\mu_o\,k_{rw}}}$ into Eq. 3-9 gives

$$\Delta p_{hump} = \frac{q_t L}{kA}\left[\left.\frac{1}{M_w + M_o}\right|_{t=t_{bt}} - \left.\frac{1}{M_w}\right|_{S_{or}}\right] \tag{3-10}$$

The magnitude of the pressure hump is controlled by the two terms in the bracket that can be investigated under two conditions:

Case 1, $M_w < M_o$: In a homogeneous porous medium when the mobility of displacing fluid (water) is lower than the mobility of displaced fluid (oil), it is expected to have a piston-like displacement with maximum sweep efficiency (Azad and Trivedi 2020; Sorbie 2013). Therefore, behind the water front, $S_o \approx S_{or}$, $k_{ro}|_{t=t_{bt}} \approx 0$, and $k_{rw}|_{t=t_{bt}} \approx k_{rw}|_{S_{or}}$. So, $\Delta p_{hump} = 0$.

Case 2, $M_w > M_o$: When the mobility of displacing fluid (water) is higher than the mobility of displaced fluid (oil), it is expected to see viscous fingering (Green and Willhite 1998). Since $(M_o + M_w)|_{t=t_{bt}} < M_w|_{S_{or}}$ (Honarpour et al. 2018), $\Delta p_{hump} > 0$.

In general, when the mobility of the displacing phase becomes higher than that of the displaced phase, the displacement deviates from piston-like conditions and fingering phenomenon occurs, thus, it is expected to see a bigger pressure hump. In other word, the less stable the displacement front is, the bigger the observed hump in the pressure profile is. During an immiscible displacement, the stability of the front is controlled by the interplay of different factors such as viscosity ratio, frontal velocity, capillary forces, interfacial tension (IFT), and heterogeneity of the medium (Hornof and Morrow 1988). Hill (1952) showed that in homogeneous porous media, during horizontal immiscible displacement using two fluids with similar densities, microscopic heterogeneities can cause perturbations on the interface of the two immiscible fluids that can grow due to the unfavorable viscosity ratio at high injection velocities. Kueper and Frind (1988) showed that even if a displacement front is considered stable based on a homogeneous model, fingers might arise as a result of different flow conductivity in regions with different permeability. The fluid displacement in a heterogeneous porous medium is governed by capillary pressure which itself depends on the pore size distribution of the medium. Fingers will simply be initiated in high permeability regions that have the minimum breakthrough pressure. Hornof and Morrow (1988) showed that a moderate reduction of IFT will magnify the effect of heterogeneity on fingering. More reduction of IFT to very low values will vanish the effect of capillary pressure and hence heterogeneity. In the extreme case of miscible displacement, the dispersion phenomenon will also dampen the fingers.

The effects of viscosity ratio, frontal velocity, capillary forces, IFT, and pore-throat size distribution are all included in the pressure drop calculation. Some are explicitly mentioned in **Eq. 3-10** and some of them indirectly affect the relative permeability term in Eq. 3-10. Therefore, a careful analysis of the pressure profile can give us valuable insight into the displacement efficiency. In the next section, we use the maximum point of the measured pressure profile during a waterflooding process (P_{max} in Figure 3-1) to calculate k_r values of oil and water at $\overline{S_w}$ behind the water front using Eq. 3-8. We use these k_r values for tuning the MBC model parameters.

3.3 Tuning the Modified Brooks and Corey Relative Permeability Model

Measuring the k_r curves of a conventional plug sample is very time-consuming and challenging. It is even harder or somehow non-practical to measure k_r in low-permeability tight rocks using conventional methods (Peng 2020). Difficulties with experimental measurements led researchers toward mathematical modeling of k_r. Although these models make the calculation of k_r easier, they still need some experimental measurements for validation and tuning of their parameters. Here, we present a practical method based on the measured pressure profile during an immiscible displacement that can be used for tuning mathematical k_r models. Since the MBC model is the most common mathematical model in petroleum engineering for the calculation of k_r values (Goda and Behrenbruch 2004), we use this model in our work. The MBC model is expressed as

$$k_{rw} = k_{rw}^{end}(S)^{n_w} = k_{rw}^{end}\left(\frac{S_w - S_{wirr}}{1 - S_{wirr} - S_{or}}\right)^{n_w} \tag{3-11}$$

$$k_{ro} = k_{ro}^{end}(1 - S)^{n_o} = k_{ro}^{end}\left(\frac{1 - S_w - S_{or}}{1 - S_{wirr} - S_{or}}\right)^{n_o} \tag{3-12}$$

To use the MBC model, at least one more data point other than the end-point relative permeability values is needed to determine the empirical exponents of the model. **Figure 3-4** Shows how the three points necessary for the tuning of the MBC model are determined. End-point relative permeabilities at residual phase saturations are determined using the steady-state method presented in chapter two. The S_{wirr} and S_{or} values, which represent the end points of the relative permeability curve, are determined using a method known as gravimetric analysis. This involves injecting one fluid phase (either oil or water) into a plug that is fully saturated with the other fluid phase, and displacing the resident fluid to reach the residual saturation. The displacement is carried out at a constant flowrate, and the effect of changing the flowrate on the residual saturation is not considered in this study. Once the steady-state condition is reached, the end-point permeabilities are recorded and the weight of the plug is measured in order to calculate the residual saturations of the fluids. The third point on the k_r curve is calculated using Eq. 3-8. The P_{max} corresponds to the breakthrough time, which occurs at the minimum total mobility. It is assumed that this minimum point coincides with the intersection of two mobilities. Additional information about the third point on the k_r curve will be provided in the following paragraphs. The method is explained using a waterflooding test on a tight plug sample as an example. The rock and fluid properties used in calculations are listed in **Table 3-1**. The experimental procedure of waterflooding test is also mentioned in Appendix F. The displacement is done at a constant flowrate of 0.06 cc/hr. The measured pressure profile resulted from the waterflooding test on the plug is shown in **Figure 3-5**.

Table 3-1: Properties of the rock and fluid used in the waterflooding experiment for tuning the MBC model parameters.

L (cm)	6.7	μ_o (cp)	5.65
A (cm2)	11.34	S_{wirr}	0.2
Φ (%)	7	S_{or}	0.15
k_{abs} (md)	0.004	k_{ro}^{end}	0.685
μ_w (cp)	1.07	k_{rw}^{end}	0.048

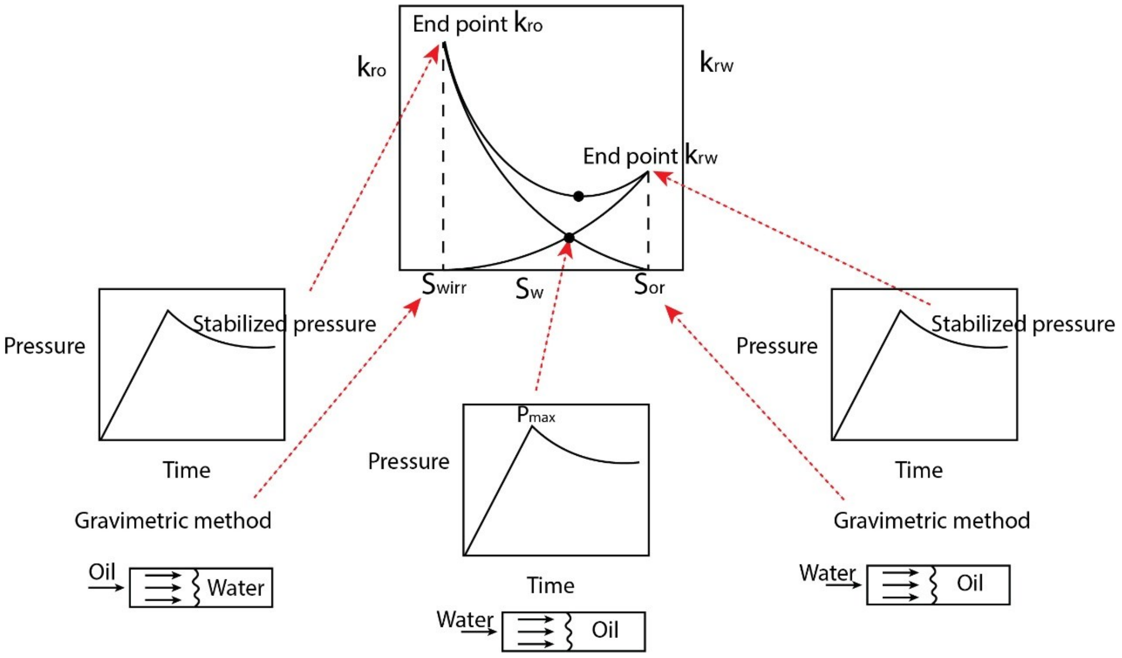

Figure 3-4: Top: Three points on each k_r curve which are needed for tuning of the MBC model parameters; Left: The end-point k_{ro} is determined from the stabilized pressure while oil is injected to displace water up to S_{wirr}. S_{wirr} is also determined using the gravimetric method; Right: The end-point k_{rw} is determined from the stabilized pressure while water is injected to displace oil up to S_{or}. S_{or} is

determined using the gravimetric method; Bottom: The saturation and k_r values at the point of intersection are determined using the method proposed in this paper.

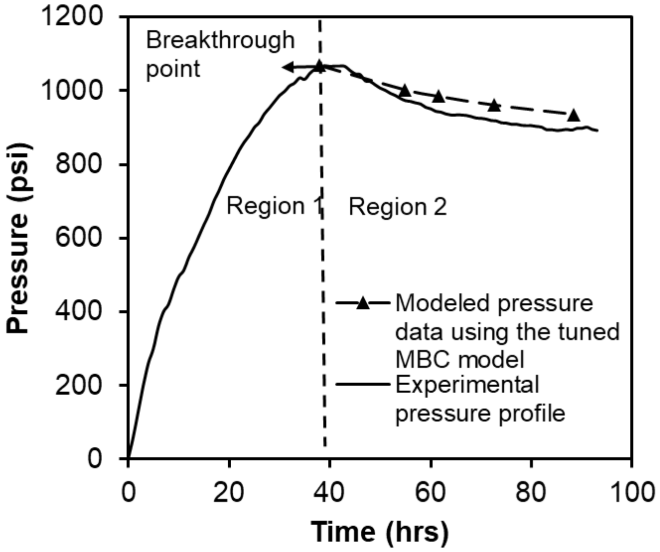

Figure 3-5: Modeled and measured pressure profiles resulted from a waterflooding test on a tight plug used for tuning the MBC model parameters. Region 1 is before the breakthrough, and region 2 is after the breakthrough. The maximum point on the pressure profile corresponds to the breakthrough point.

One of the assumptions of the JBN method is that the $\overline{S_w}$ behind the front is constant for each traveling front, while the front moves from inlet to outlet, during the displacement with a constant injection flowrate (Johnson et al. 1959). Therefore, during the displacement, a constant saturation and hence, a constant relative permeability, can be considered for the fluid flow behind each front in region 1 of Figure 3-5. In region 2 of Figure 3-5, we can have the same assumption of constant $\overline{S_w}$ behind the front of each saturation before its breakthrough. We also assume that the highest point in the pressure profile (P_{max}) corresponds to the water breakthrough time. Since the injection is at a constant flowrate, we can calculate $\overline{S_w}$ behind the front at the time of breakthrough. Based on Eq. 3-8, knowing $\overline{S_w}$ at P_{max}, we can calculate $M_o + M_w$ at that saturation. We need one more independent relationship between oil and water mobility values to determine each of them separately. Figure 3-6 shows M_o, M_w, and $M_o + M_w$ curves vs. S_w. Based on Figure 3-6, we make another assumption that S_w at the minimum point of the $M_o + M_w$ curve (point *O'*) coincides with the point of intersection between M_o and M_w curves (point *O*). We will talk about the error associated with this assumption later in this section. At the point of intersection, $M_o = M_w$. Using this equality relationship and the one derived from Eq. 3-8, we can calculate the k_r values at $\overline{S_w}$ behind the front:

$$\begin{cases} M_w + M_o|_{t=t_{bt},\ S_w=\overline{S_w}} = \dfrac{q_t L}{P_{max} k A} \\ M_w = M_o|_{t=t_{bt},\ S_w=\overline{S_w}} \end{cases}$$

This point on the k_r curves is used to tune the MBC model parameters and find the empirical exponents.

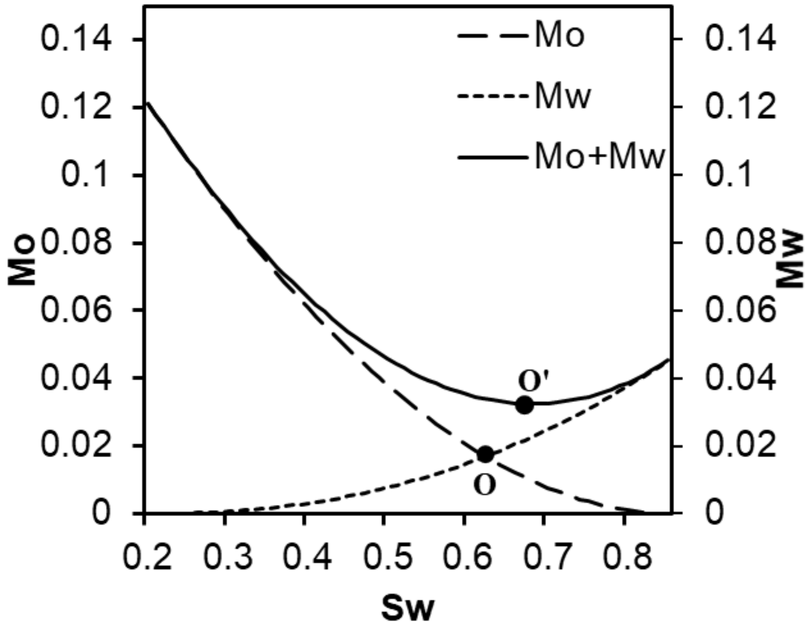

Figure 3-6: Graph of M_o, M_w, and $M_o + M_w$ curves vs. S_w for the rock and fluid system described in Table 3-1, using the MBC model. Point O is the point of intersection between the M_o and M_w curves. Point O' is the minimum point on $M_o + M_w$curve.

3.4 Verification of the Tuned MBC Model Based on the Experimental Results

In the water flooding experiment which was explained before (Table 3-1), the calculated empirical exponents are $n_o = 1.88$ and $n_w = 2.28$. We use the parameters of the tuned MBC model to predict the pressure after the breakthrough of water to confirm our method for k_r calculation. The predicted pressure values are shown in Figure 3-5. The mean absolute percentage error (MAPE) between modeled and measured pressure data is less than 3%.

Here, we investigate our assumption about the coincidence of S_w at points *O* and *O'* in Figure 3-6. The tuned MBC model for our waterflooding experiment is as follows

$$k_{rw} = 0.048\left(\frac{S_w - 0.2}{1 - 0.2 - 0.15}\right)^{2.28} \tag{3-13}$$

$$k_{ro} = 0.685\left(\frac{1 - S_w - 0.15}{1 - 0.2 - 0.15}\right)^{1.88} \tag{3-14}$$

Taking the derivative of $M_o + M_w$ with respect to S_w ($\frac{\partial(M_o+M_w)}{\partial S_w} = 0$), we find that the minimum point of the curve (point *O'*) is at $S_w = 0.68$ whereas, the intersection point of M_o and M_w curves (point *O*) happens at $S_w = 0.62$. The error corresponding to our assumption of coincidence of points *O* and *O'* is less than 10% for this waterflooding example. It should be noted that the more symmetric the mobility curves are (in terms of end-point relative permeabilities and Corey exponents), the closer the points *O* and *O'* would become.

3.5 Analysis of Two-Phase Flow Pressure Profile from "Flow Work" Perspective

In this part, we analyze the pressure profile during an immiscible displacement from the "flow work" perspective to understand the effect of the observed hump in the pressure profile on the efficiency of the displacement process. By definition, flow work is the work done by pressure, *P,* to displace volume *V* of a fluid through a cross-sectional area and is equal to *PV* (Berg et al. 2020; Akai et al. 2020). Since the displacement process takes place at a constant injection flowrate, time corresponds to the volume of injected fluid. Therefore, in the pressure profile, the area under the curve represents the flow work that has been done to displace a certain volume of fluid out of the plug sample (Ma et al. 1999; Khanamiri et al. 2018). Here, we investigate the effect of the added area as a result of a hump in the pressure profile, on the efficiency of the displacement process.

Figure 3-7 shows the pressure profile measured during a water flooding process to displace oil out of a tight plug with a permeability of around 1 microDarcy. The procedure for waterflooding experiment is shown in Appendix F. The rock and fluid properties used in this test are listed in

Table 3-2. It also shows the modeled pressure profile for a single-phase flow of water through a different plug that has a permeability similar to the end-point permeability of water in the water flooding case. The pressure modeling is done using the method proposed in chapter two. The flow work done during water flooding corresponds to the area under the curve of pressure profile. The constant injection flow rate means that this area can be considered as the actual work, when the time is multiplied by the injection flow rate. We consider the required work up to the time of pressure stabilization (points A and A' in Figure 3-7). It is evident that the two-phase flow needs more work to reach the stabilization state compared to the single-phase flow. We showed in previous chapter that even for a single-phase flow when a large accumulator is used for the injection of a fluid into the plug, extra work must be done on the fluid to compress it to the final pressure and that will cause an extra time to reach to the stabilized condition.

Table 3-2: Properties of the rock and fluid used in the waterflooding experiment for flow work analysis.

L (cm)	6.7	μ_o (cp)	3.54
A (cm^2)	11.34	μ_w (cp)	1.07
Φ (%)	7	k (md)	0.001

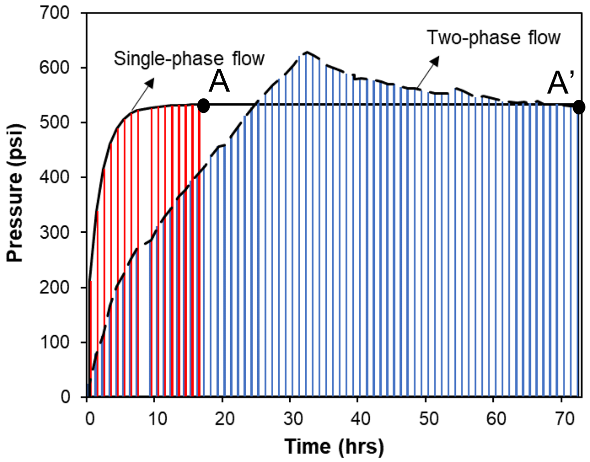

Figure 3-7: Flow work done during single-phase flow of water and two-phase flow during water flooding. Points A and A' show the time of pressure stabilization for single-phase and two-phase flow, respectively.

When we observe a bigger hump in a pressure profile or a longer time to reach a stabilized pressure, the displacement process requires more work. We reviewed different factors that affect the hump in the pressure profile in section 3.2. Here, we show the effect of S_{wi} and *IFT* on pressure profile and flow work using water flooding experiments done on a tight plug. **Figure 3-8a** shows the effect of S_{wi} on the pressure profile during the water flooding process from the perspective of flow work. In Figure 3-8a, it is shown that when S_{wi} of a porous medium is nonzero, the pressure slope is steeper, and a relatively bigger hump is observed as a result of reduced k_{ro}. On the other hand, we see a sooner pressure stabilization since there is less oil inside the pore space that needs to be displaced by water. **Figure 3-8b** shows the effect of *IFT* on the pressure profile during a flowback process where oil displaces the leaked off fluid out of a tight rock. In two separate tests, one pore volume of water with *IFT = 6 mN/m* and a surfactant solution with *IFT = 0.6 mN/m* are injected as the leak-off fluids and plugs are soaked for 1 day under pressure. After that, oil is injected at the constant flowrate of *0.06 cc/hr* to displace the leak-off fluid. The detailed experimental procedure of leak-off and flowback tests will be explained in the next chapter. Lowering IFT reduces capillary pressure and hence improves the relative permeability of both phases. So, the observed hump in the pressure profile is bigger when water with a higher IFT value is used as the leak-off fluid. The end part of the graph, which corresponds to the stabilized pressure at S_{wirr}, shows a minor improvement when IFT is reduced by one order of magnitude. This can be explained by the desaturation curve (Yeganeh et al. 2016; Lake 1989) showing that the residual saturation does not change significantly unless IFT is reduced to low values.

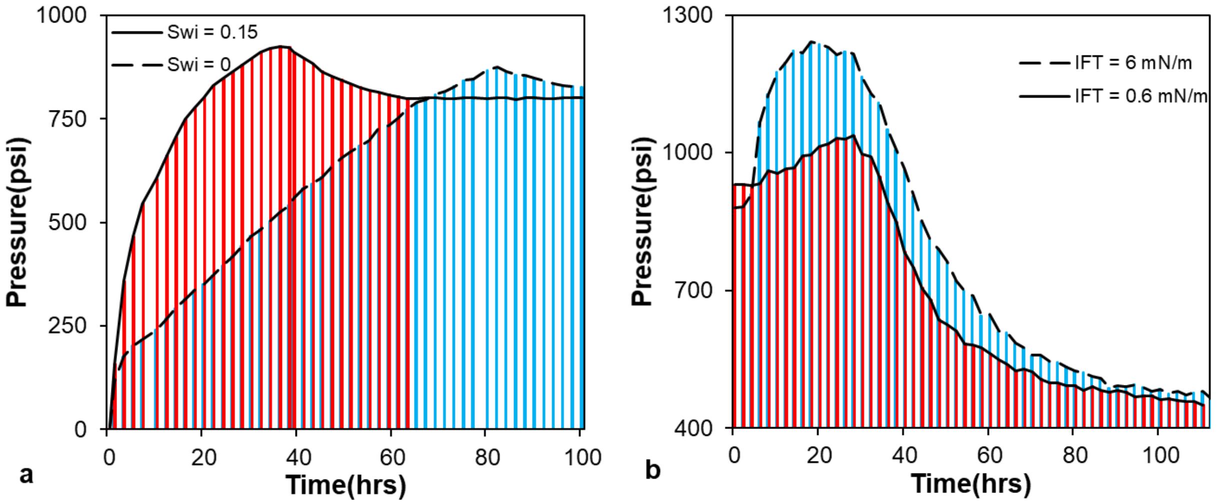

Figure 3-8: Effect of a) initial water saturation, and b) IFT on pressure profile during a two-phase displacement process.

3.6 Implications in Field-Scale Hydraulic Fracturing

The learnings from Figure 3-8b are applicable to a field-scale flowback process as well. It should be noted that in real field conditions, the constraint is not usually constant flowrate, but constant bottomhole pressure. In that case, a bigger pressure hump corresponds to a lower production flow rate. Therefore, the factors that accentuate the pressure hump will cause lower production flowrate. From work perspective, a certain amount of work is needed to displace the leaked off fluid out of the rock matrix. Since the reservoir pressure is finite, if the rock and fluid properties are not favorable (high mobility ratio, high capillary force, high IFT, and higher degree of plug heterogeneity causing a bigger hump), the reservoir pressure might not be adequate to maintain an economic production flowrate. Therefore, the leaked-off fluid forms a blockage that is hard to remove even at high imposed draw-down values. In this case, it would be crucial to use chemical additives to modify the rock and fluid properties in a way that reservoir pressure could maintain an economic production rate by removing the water blockage.

3.7 Summary

In this chapter, we presented a simple mathematical technique based on frontal advanced theory to model the pressure profile during a two-phase immiscible displacement in a tight porous medium. Combining this technique with the pressure profile measured during the displacement process and considering some simplifying assumptions, we measured the k_r values for the two phases. We used the measured k_r values to tune the parameters of the modified Brooks and Corey (MBC) relative permeability model. We performed waterflooding and leak-off/flowback experiments on tight rock samples to verify and show the application of the proposed method. We used the tuned MBC k_r model to predict the observed pressure profile after breakthrough during a waterflooding experiment. Comparing the modeled and measured pressure profiles shows a mean absolute percentage error (MAPE) of less than 3%. At the end, we investigated the shape of the pressure profile during an immiscible displacement from flow-work point of view. The effect of

S_{wi} and *IFT* on the amount of work needed during the displacement process was discussed. Here is the list of conclusions:

- In the JBN method, the pressure drop during the immiscible displacement is calculated using an integral term in which the change of k_r with S_w is considered. We proposed a simplifying assumption to calculate the pressure drop using k_r values at $\overline{S_w}$ behind each saturation front before its breakthrough. Using this assumption makes the pressure drop calculation much easier by introducing just 2% and 6% errors when the mobility ratio is 1 and 10, respectively.
- The proposed model for pressure drop explains the observed hump in the pressure profile during a two-phase immiscible displacement process. Any factor that disturbs the stability of the front, will cause a deviation from piston-like displacement, and hence, will cause a bigger hump in the pressure profile.
- We assume that the minimum point on the total mobility (M_o+M_w) curve coincides with the point of intersection between the M_o and M_w curves. The error associated with this assumption is less than 10% for the example mentioned in the manuscript. The more symmetric the mobility curves are, the less the error associated with this assumption is. This assumption enables us to determine k_r values for both oil and water phases from a measured pressure profile during an immiscible displacement process.
- We conducted a waterflooding experiment on a tight rock sample, used *the* P_{max} of the pressure profile to calculate k_r values for oil and water, and used those values to tune the MBC k_r model. We used the tuned model to predict the pressure profile after the water breakthrough. The mean absolute percentage error (MAPE) between modeled and measured pressure data is less than 3%.
- We proposed a new explanation for the shape of the pressure profile from flow-work perspective. A bigger hump in the pressure profile suggests more work is required for the displacement process. We used the measured data of leak-off and flowback tests done on a low-permeability tight plug for this analysis. A bigger pressure hump in our tests corresponds to a lower production rate for a well that produces under constant bottomhole pressure. Therefore, factors such as high mobility ratio, high capillary force, high IFT, and

a higher degree of rock heterogeneity causing a bigger hump, will cause a lower production flowrate for the well.

- Using the flow-work concept, a new explanation was presented regarding the effect of IFT reduction on water blockage removal

Chapter 4

A Laboratory Protocol for Surfactant Screening in Hydraulic Fracturing Operations

4.1 Introduction

Due to improvements in horizontal drilling and hydraulic fracturing, unconventional resources such as tight and shale reservoirs have seen significant growth in recent years. According to the Energy Information Administration's annual energy outlook (Nalley and LaRose 2022), tight oil production in the US is expected to increase from 8.2 million barrels per day in 2022 to 9.1 million barrels per day in 2050, making up over 70% of total US oil production. Additionally, tight and shale gas production is expected to increase from 31.7 trillion cubic feet in 2022 to 39.2 trillion cubic feet in 2050, comprising more than 92% of all US natural gas production.

During hydraulic fracturing operations, a large volume of fracturing fluid is pumped into the well to create and extend fractures. Some part of the injected fluid remains in the fracture system and some part of it leaks-off into the rock matrix. At the end, pressure is released to let the well flow. During flowback and post flowback periods, usually 5-50% of the injected fluid will be recovered (Bertoncello et al. 2014). The remaining leaked-off fracturing fluid will form a water-loaded zone near the fracture face that hinders oil production (Bennion et al. 1996). On the other hand, the imbibition of fracturing fluid into the rock matrix can be considered as a production mechanism that pushes the oil out of the rock matrix (Habibi et al. 2017; Kathel and Mohanty 2013). This dual effect of fracturing fluid led researchers to seek a balance in which the oil recovery due to imbibition is maximized and the water blockage near the fracture face is minimized. Chemical additives such as surfactant solutions, microemulsions, and nanoparticles have been introduced in an effort to achieve this balance (Sheng 2015; Olayiwola and Dejam 2019; Habibi et al. 2020;

Zargartalebi et al. 2014). Evaluating the impact of these additives on regained permeability and post-flowback well performance is necessary for their potential use in field applications.

Oil recovery can be enhanced by using surfactants through mechanisms such as 1) interfacial tension (IFT) reduction, 2) wettability alteration towards more water-wet condition, and 3) detachment of adsorbed oil (Abdulelah et al. 2018; Akbarabadi et al. 2017; Alvarez and Schechter 2016; Bui et al. 2016). Different kinds of surfactants have been used for enhancing imbibition oil recovery in tight rocks (Park and Schechter 2020; Alvarez and Schechter 2016; Nguyen et al. 2014; Wang et al. 2012).

Anionic surfactants are the most commonly-used type in chemical EOR, particularly for sandstone reservoirs (Kamal et al. 2017). These surfactants have a negatively charged hydrophilic head, such as sulfonate (SO_3^-), sulfate (SO_4^{2-}), or carboxylates (COO^-). Sulfonate surfactants are stable at high temperatures but can precipitate in high-salinity environments, while sulfate surfactants are more resistant to high salinity but can decompose at high temperatures (Gbadamosi et al. 2019).

Cationic surfactants have a positively charged hydrophilic head and are therefore attracted to the negatively charged surfaces. They are particularly effective at changing the wettability of carbonate rocks (Massarweh and Abushaikha 2020). The positive charge on the surface of the carbonate rocks repels the polar head of the surfactant, causing the nonpolar tail to orient towards the rock surface. This leaves the polar, hydrophilic head of the surfactant in contact with water at the rock-fluid interface, resulting in a more water-wet condition (Castro Dantas et al. 2014). Cationic surfactants are generally more expensive than anionic surfactants due to the high pressure hydrogenation reaction required in their synthesis (Kumar et al. 2016).

Zwitterionic or amphoteric surfactants have both positive and negative charges on their hydrophilic head. They exhibit both anionic and cationic properties upon their dissociation in water. They have attracted attention because they tolerate high-temperature and high-salinity conditions. These surfactants are more expensive compared to other types of surfactants. A typical example of amphoteric surfactant is betaine (Kamal et al. 2017; Gbadamosi et al. 2019).

Non-ionic surfactants have a wide range of applications in pesticides, medicine, the food industry (Xia et al. 2020), detergents (Cheng et al. 2020), and EOR processes (Bustamante-Rendón et al. 2020). Unlike anionic and cationic surfactants, non-ionic surfactants do not ionize in aqueous solutions and are soluble due to hydrogen bonds and van der Waals interactions. They are highly tolerant at high-salinity environments but have a lower ability to reduce the interfacial tension (IFT) compared to ionic surfactants (Kamal et al. 2017). Non-ionic surfactants are often preferred for field applications due to their lower incompatibility issues with other chemicals commonly used in fracturing fluids, such as friction reducers or clay stabilizers, and due to their lower sensitivity to the salinity of reservoir brine (Habibi et al. 2020; He and Xu 2018).

Several studies have been conducted to examine the use of surfactant solutions in increasing imbibition oil recovery and decreasing water trapping using various methods (Habibi et al. 2020; Tangirala and Sheng 2019; Abdulelah et al. 2018; Liang et al. 2017; Bui et al. 2016; Nguyen et al. 2014). However, it is difficult to measure liquid permeability (k_L) of ultra-tight rocks, so these studies often use relatively high-permeability outcrop samples. For example, Liang et al. (2017) used outcrop samples from Indiana limestone with permeabilities in the milli-Darcy range in core flooding experiments to assess the impact of surfactants and shut-in time on water blockage during and after flowback processes. They found that surfactants and shut-in can improve hydrocarbon permeability after flowback, but the extent of improvement depends on petrophysical properties of the rock and initial saturation state. Tangirala and Sheng (2019) used outcrop Berea sandstone plugs from an upper Devonian Formation and Crab Orchard plugs from Pennsylvanian Formation with milli-Darcy permeabilities in both spontaneous imbibition and core flooding experiments to measure regained k_L. They concluded that a surfactant that performs well in an imbibition test, may not produce optimum results in a core-flow test.

Difficulties in tight rock permeability measurement led the researchers to limit their studies either to imbibition study of tight rocks or flow study in relatively high permeability outcrops. However, in a recent study (Yousefi and Dehghanpour 2022), we developed a model and measurement technique for k_L of tight rocks based on the steady-state method in a shorter time frame. This technique allows for the measurement of k_L in tight plugs before leak-off (LO) and after flowback (FB), enabling to propose a comprehensive laboratory protocol to study the effect of various chemical additives on the regained k_L after flowback. This protocol is used to investigate the effect of surfactant type and polarity, surfactant adsorption, IFT, and wettability on the regained permeability to screen different surfactant solutions used in hydraulic fracturing operations.

In this study, we aim to investigate the impact of various surfactant solutions on the regained k_L of tight plugs from the Montney Formation with micro-Darcy permeabilities. To do this, we compare k_L before leak-off and after flowback. Since the plug sample used here is composed of sandstone and siltstone, we focus on anionic and non-ionic surfactants. We test surfactants with different polarities, which result in different wettability alteration potentials and different IFT values with the oil sample. We investigate the effect of these parameters on the efficiency of the surfactant solution on retaining regained k_L. We also measure the particle size distribution of the structures formed in the surfactant solution used as the leak-off fluid. Then, we compare it with the pore-throat size distribution of the plug obtained from the mercury injection capillary pressure (MICP) test to evaluate the possibility of pore-throat blockage by the surfactant solutions. Finally, we examine the effect of initial water saturation (S_{wi}) on the performance of the surfactant solution in enhancing regained k_L after the flowback process.

4.2 Materials

Here, we describe the properties of the fluid samples and core plugs used in this study.

4.2.1 Fluid samples: We conducted the experiments using a dead oil sample from the Montney Formation, a synthetic brine with a high concentration of dissolved solids (130,000 ppm TDS), and various surfactant solutions at a concentration of 1 gpt (gallons of chemical per 1000 gallons of water) in deionized water. Since the produced brine is mixed with additives used during fracturing operations, we prepare a synthetic brine using the chemical composition of the reservoir brine. Both the oil and brine were filtered through a 10-micron filter to remove any impurities that could potentially block pores. The process of preparing the brine followed the ASTM D1141 standard and is described in **Appendix A**. **Table 4-1** provides a detailed breakdown of the ionic composition of the synthetic brine used in the experiments.

Table 4-1: Ionic composition of the synthetic brine.

Ion	Na^+	K^+	Ca^{2+}	Mg^{2+}	Cl^-	$SO4^{2-}$
Concentration in brine (mg/L)	49,750	1,220	1,120	596	81,379	623

Table 4-2 presents the physical properties of both the oil sample and synthetic brine at 25ºC. The measurement accuracy for viscosity and density are also included in the table.

Table 4-2: Physical properties of the crude oil and synthetic brine.

Properties	Crude oil	Brine
Viscosity (cp)	5.65±0.02	1.33±0.02
Density (gr/cm^3)	0.840±0.001	1.088±0.001

The crude oil composition is listed in **Table 4-3**.

Table 4-3: Dead oil composition.

Component	CO2	C1	C2	C3	IC4	NC4	IC5	NC5	C6	C7+
Mole fraction	0.0023	0.0573	0.0293	0.0446	0.0120	0.0453	0.0242	0.0382	0.0645	0.6823

In this study, 7 different surfactant solutions with a concentration of 1 gpt are used. These surfactant solutions were chosen in a way to cover a wide range of IFT, contact angle, and adsorption. The physical properties of the solutions are reported in **Table 4-4**.

Table 4-4: Physical properties of the surfactant solutions used in this study.

Properties	SS-1	SS-2	SS-3	SS-4	SS-5	SS-6	SS-7
Viscosity (cp)	1.13	1.07	1.08	1.05	1.07	1.11	0.98
Density (gr/cm^3)	0.994	0.994	0.993	0.993	0.993	0.994	0.994
Surfactant Type	Anionic	Slightly Anionic	Non-ionic	Non-ionic	Non-ionic	Anionic	Anionic

For this study, we selected non-ionic and anionic surfactants with varying degrees of polarity. Cationic and amphoteric surfactants are relatively more expensive than anionic and non-ionic surfactants, so their use is limited. In addition, we also considered the degree to which the surfactants changed the IFT with oil and the wettability of the rock. The IFT of the different surfactant solutions with oil ranged from 0.9 mN/m to 8.75 mN/m, providing a wide range of values. The surfactant solutions were selected to cover a wide range of contact angles, from 45 degrees, which makes the rock water-wet, to around 90 degrees, resulting in a neutral wet rock, to

124 degrees, which maintains the rock's oil-wet state. The measured IFT and contact angle values of the selected surfactant solutions will be presented in the results and discussion section.

4.2.2 Core Samples:

For this study, we used a core plug from a well drilled in the Montney Formation, a stratigraphic unit of the Lower Triassic age in the Western Canadian Sedimentary Basin (WCSB) located in British Columbia and Alberta (Davies et al. 1997). The Montney Formation is primarily a low-permeability siltstone reservoir. As shown in **Table 4-5**, the x-ray diffraction analysis indicates that the plug is dolomitic siltstone with a small amount of clay minerals, including Illite-Smectite (I/S) mixed-layer. The I/S mixed layer has 20-25% interlayered (expandable) smectite, which means less than 1% of this mixed layer could be expandable, suggesting that the core plug is not particularly sensitive to fresh water.

Table 4-5: Mineralogy of the plugs determined from the XRD method.

Sample ID	Quartz (wt%)	K-feldspar (wt%)	Plagioclase (wt%)	Calcite (wt%)	Dolomite (wt%)	Pyrite (wt%)	Illite (wt%)	Total Clay (wt%)
1	35.8	16.5	2.8	0.8	41.9	0.8	1.3	1.4

The XRD and SEM analyses were performed on an offset core plug taken from a depth 10 cm above the depth of the target core plug. **Figure 4-1** shows Scanning Electron Microscopy (SEM) images of a thin section sample. Figure 4-1a shows that the sample has a mixed granular to microcrystalline texture. Figure 4-1b shows that intergranular pores (yellow arrows) are mainly surrounded by quartz grains. Dolomite is a cementing component and is distributed throughout the sample. Figure 4-1c shows that authigenic illite coats the surface of quartz grains and partially fills the pores. Trace amounts of detrital chlorite flakes are also observed. Organic matter is rare in this sample.

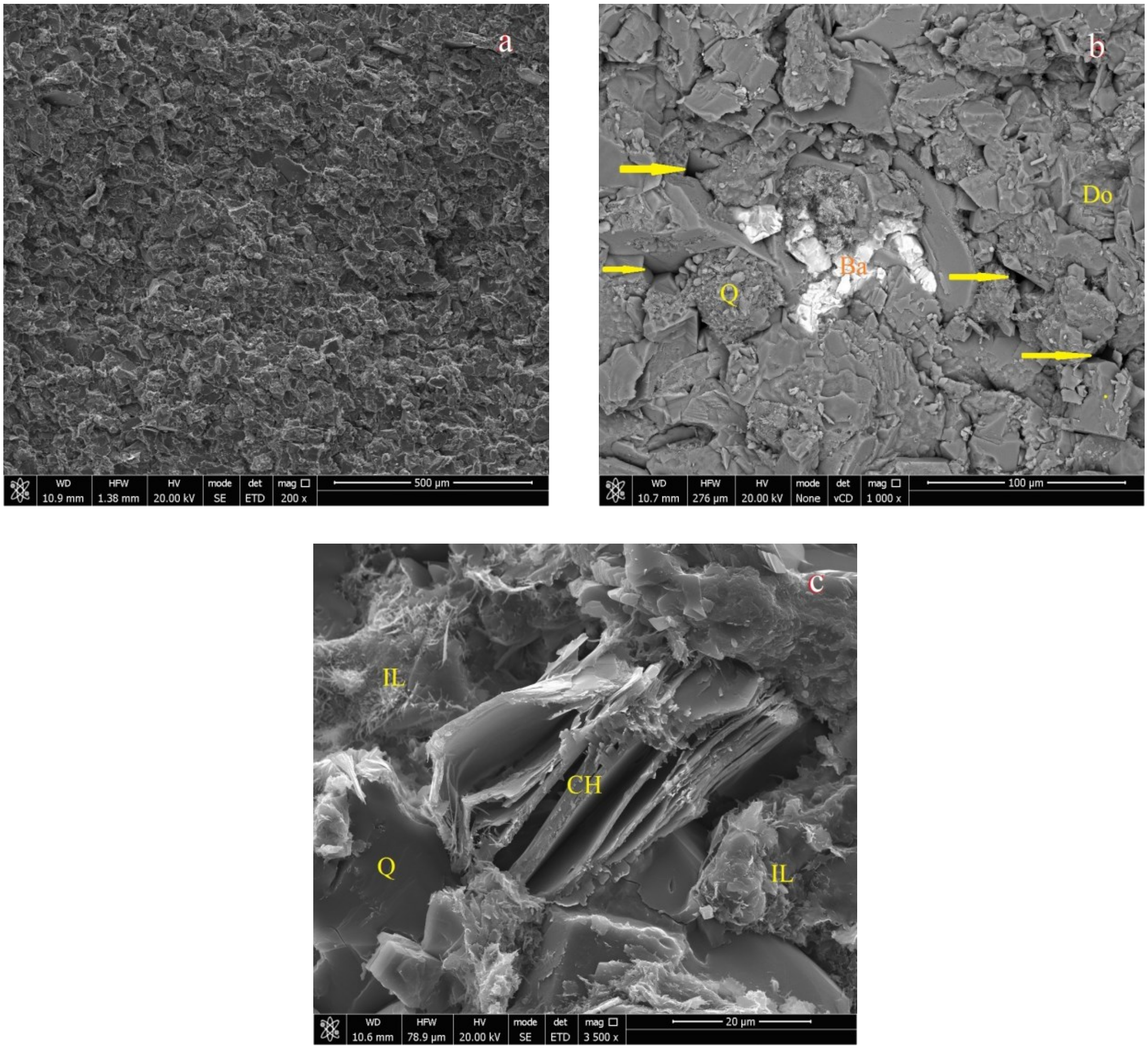

Figure 4-1: SEM images of the thin section sample. a: Sample has mixed granular to microcrystalline texture; b: framework grains are mainly quartz. Dolomite as a cement component is abundant. Intergranular pores (yellow arrows) are the most common pore type; c: Illite coats grains and/or partially fills pores. Trace amounts of detrital chlorite flakes are also present.

Figure 4-2 shows the pore-throat size distribution of the plug obtained by the Mercury Intrusion Capillary Pressure (MICP) analysis. International Union of Pure and Applied Chemistry (IUPAC) (Rouquerol et al. 1994) suggests pores can be categorized according to their size:

i. Micropores: pores< 2 nm

ii. Mesopores: 2 nm< pores <50 nm

iii. Macropores: pores> 50 nm

According to this classification and Figure 4-2, 20% and 80% of the pore throats in this core plug are categorized as mesopores and macropores, respectively. The median pore-throat size, defined as the pore-throat diameter at 50% mercury intrusion, is 280 nm for this plug.

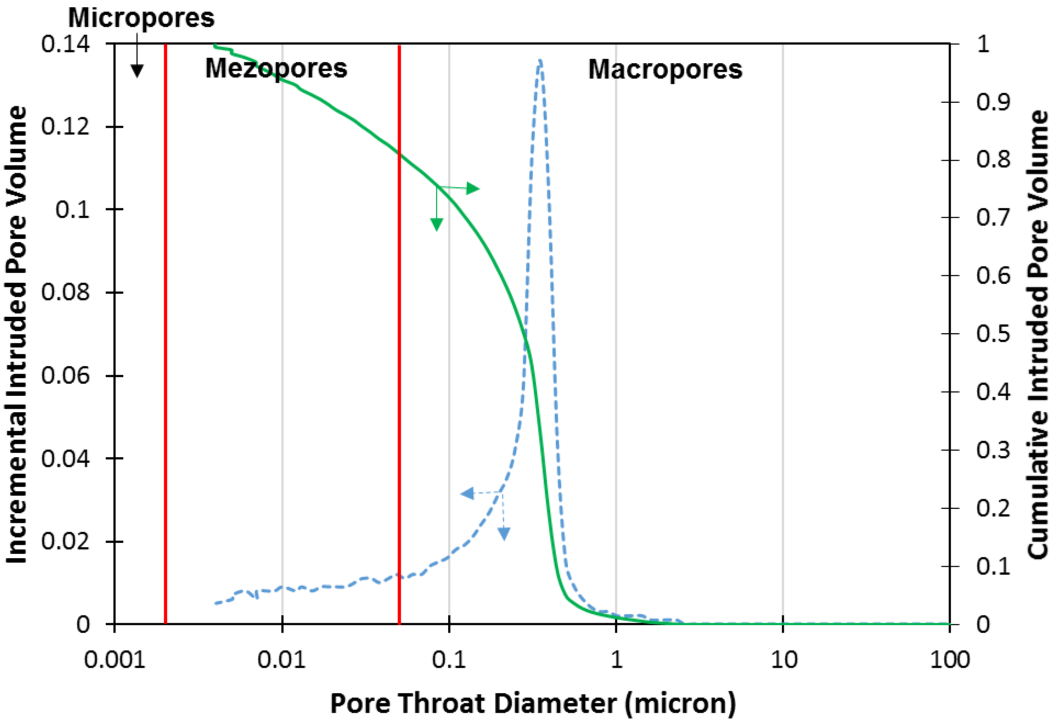

Figure 4-2: Pore-throat size distribution of the core sample based on MICP data; 20% and 80% of pore throats are classified as mesopores and macropores, respectively.

The physical properties of the core plugs are listed in **Table 4-6**.

Table 4-6: Properties of the Montney plug.

Sample	Depth (m)	Diameter (cm)	Length (cm)	Bulk Volume (cm3)	Porosity (fraction)
1	2531.3	3.8	6.65	75.42	0.055

4.3 Methodology

Different surfactant solutions in fracturing fluid employ various methods to boost oil recovery through imbibition and reduce water trapping near the fracture face. For instance, it is crucial to keep IFT from dropping to extremely low levels as per the Young-Laplace equation, this could eliminate capillary imbibition, a mechanism for oil production in tight and shale reservoirs. By testing the properties of these surfactant solutions in a laboratory protocol, we can better understand their behavior and select the most suitable ones for use in hydraulic fracturing operations. This study examines the following surfactant properties: the surfactant type and its surface charge, the level of surfactant adsorption on the rock surface, the change in IFT, and the alteration in wettability. The ultimate metric to compare various surfactant solutions is the regained permeability after flowback.

In this laboratory protocol, as depicted in **Figure 4-3**, we simulate the leak-off, soaking, and flowback processes that occur during a hydraulic fracturing operation in an unconventional shale or tight reservoir. We measure the k_L of the sample before introduction of the surfactant fluid as the base permeability. After flowback we again measure the k_L and compare it to the base permeability to find out about the efficiency of the surfactant solution on permeability retention. In this laboratory protocol, we study how different surfactant solutions impact the regained k_L of tight rocks. We utilize non-ionic and anionic surfactants with different polarities, which provide a wide range of IFT and contact angle in the presence of oil and rock surface. The protocol involves using different surfactant solutions as leak-off fluids to examine their effect on regained permeability after the flowback stage.

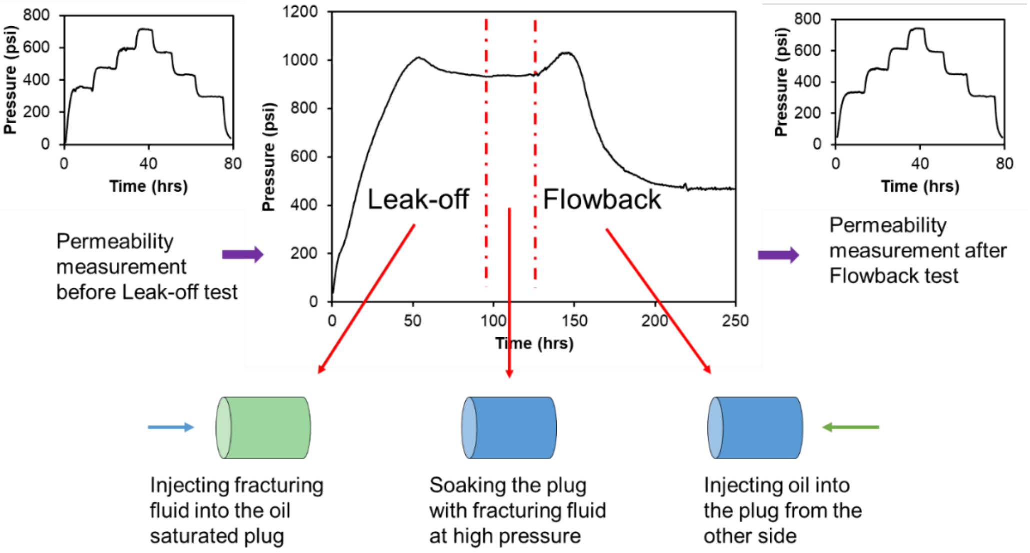

Figure 4-3: Schematic of proposed protocol to investigate the effect of different surfactant solutions on regained permeability.

4.3.1 IFT Measurement: We measure the IFT between oil and various surfactant solutions using a spinning drop tensiometer, which consists of a capillary tube that spins around its long axis. The capillary tube is filled with the heavier phase (surfactant solution) and a droplet of the lighter phase (oil) is elongated at the center due to centrifugal force. A software captures the curvature of the oil droplet and uses the Vonnegut (1942) equation to calculate the IFT value. Each IFT measurement is repeated three times, and the mean value is reported. The device has an accuracy of 1×10^{-6} mN/m for IFT measurement.

4.3.2 Contact Angle Measurement: We use an optical tensiometer to measure the liquid-liquid contact angle (*CA*) and investigate the wettability of the rock sample in the presence of oil and different surfactant solutions. The device consists of a camera, a light source, and a droplet dispenser. To prepare the sample, we first polish the surface of the sample to make it smooth, then saturate it with oil and keep it immersed in the oil for 1 week. After this, the oil-saturated sample is immersed in the surfactant solution. A fixed-volume oil droplet (10 μL) is placed on the rock surface using the droplet dispenser, and the camera records the shape of the oil droplet. The tensiometer software uses the Young-Laplace equation to calculate the equilibrated *CA*. Each test is repeated three times, and the mean value is reported. The device has an accuracy of 0.1 degrees for CA measurements.

4.3.3 Particle Size Measurement: Depending on the type and concentration of the surfactants, they may agglomerate and form bigger structures in the solution. These structures include lamellar sheets, vesicles, cylindrical micelles, spherical micelles, or reverse micelles (Massarweh and Abushaikha 2020; Cornwell 2018). To measure the size of these structures in the surfactant solution, we use a particle size distribution (PSD) measurement device, the Malvern Zetasizer Nano ZS, which utilizes the dynamic light scattering method. This method allows us to measure particle sizes ranging from 0.3 nm to 1 μm with an accuracy of ±0.1 nm. The device works by detecting changes in the intensity of light as it is scattered by the particles in the solution, which constantly undergo Brownian motion. By recording these intensity changes over time, we can obtain information about the movement of the particles on a time scale and plot a particle size profile. We repeat each measurement three times at ambient conditions and report the mean value. We compare the PSD of different surfactant solutions to the pore-throat size distribution of the rock sample to assess the potential for pore-throat blockage.

4.3.4 SEM Imaging: We use SEM imaging to study surfactant adsorption on the surface of the rock sample. We use a Field Emission Scanning Electron Microscope (FE-SEM) to examine the surface topography of the rock sample. Prior to the analysis, the rock sample is polished with a grinder, a polisher, and sandpapers with Grades P400, P800, P1200, and P2400 in sequence to get a smooth surface. After polishing, the sample is ion milled to further reduce the surface roughness. Then, the sample is coated with gold to eliminate the charging effects using a sputter coater. Once these steps are complete, the sample is ready for SEM imaging. As a reference, we use a clean rock sample and compare the images to those of a rock sample in contact with a surfactant solution.

4.3.5 Critical Micelle Concentration (CMC) Measurement: According to IUPAC, the critical micelle concentration (CMC) is the surfactant concentration at which micelles form and any additional surfactants will not alter the properties of the solution, but will simply create more micelles (Hu et al. 2010). The CMC can be determined from a plot of surface tension versus surfactant concentration, and it represents a point where an increase in surfactant concentration does not affect the surface tension. There are various methods for measuring CMC, including tensiometry, conductivity, spectrophotometry, and fluorometry (Khan et al. 2020). In this study, we use the surface tension method (Belhaj et al. 2021), which involves measuring the forces exerted on a platinum probe placed at the liquid surface. The probe is connected to a highly sensitive balance, and the liquid surface is brought into contact with the probe. The force measured by the balance as the probe interacts with the liquid surface can be used to calculate the surface tension. Each surface tension measurement is repeated six times for each sample, and the average value is reported.

4.3.6 Surfactant Adsorption Test: We conduct static adsorption tests to assess the adsorption behavior of surfactant mixtures on rock surfaces (Zeng et al. 2020; Yekeen et al. 2019; Xu et al. 2018). The rock sample is first crushed and sieved using a 140 mesh sieve (125 µm). The resulting rock powder is mixed with DI water at a 1:20 ratio and stirred for 1 day to fully hydrate the rock particles. The surfactant sample is then added to the mixture at a concentration of 1 gpt and stirred for additional 2 days to allow the surfactant particles to interact with the rock powder. After two days, the mixture is filtered to prepare it for the surfactant concentration measurement. The concentration of surfactant after mixing is compared with that before performing the adsorption test to measure the amount of surfactant loss due to adsorption. The amount of surfactant adsorption per unit weight of rock powder can be calculated by (Belhaj et al. 2022):

$$\Gamma\left({}^{mg}/_{g}\right) = \frac{\left[C_0\left({}^{mg}/_{L}\right) - C\left({}^{mg}/_{L}\right)\right].V(mL)}{M(g)} \times 10^{-3} \tag{4-1}$$

Here, Γ represents surfactant adsorption, C_0 is the initial surfactant concentration, C is the final surfactant concentration, V is the sample volume, and M is the mass of crushed rock. A force tensiometer is used to measures the surface tension of the filtered mixture. To determine the surfactant concentration in the filtered mixture, a calibration curve is created by plotting the solution surface tension versus known surfactant concentrations. The surface tension of the surfactant solution after the adsorption test is then compared to this curve to obtain surfactant concentration.

4.3.7 Core Plug Preparation: The following procedure is carried out on a core plug in order to prepare it for flooding experiments and ensure that the mineralogy and petrophysical properties of the rock do not affect the results.

1. Clean the rock sample using a polar (methanol) and a non-polar (toluene) solvent to remove all the residual fluids inside the sample (McPhee et al. 2015). Since the organic matter and expandable clay content of the rock sample are negligible, the cleaning procedure does not induce damage to the structure of the porous medium.
2. Put the plug inside an oven at 90°C for 2-5 days. Monitor the plug's weight with time to ensure it is completely dry.
3. Mount the plug into a core holder, vacuum it for one day, and then inject brine to saturate it. Keep the plug under 1100 psi pore pressure for two days while the confining pressure is 1800 psi. Then, inject approximately two pore volumes (*PV*) of brine to ensure the plug is fully saturated with brine.
4. Weigh the saturated plug and compare it with the dry weight to calculate the pore volume.
5. Inject 4-5 *PV* of oil at a constant flowrate (Q) of 0.06 cc/hr to displace the brine out of the plug and reach irreducible water saturation (S_{wirr}). We assume the plug is at S_{wirr} when no

more brine is produced and the injection pressure profile is stable. The established S_{wirr} is considered initial water saturation (S_{wi}) for the next tests.

6. Keep the oil-saturated plug at 1100 psi pore pressure in the coreholder for one week for aging.

When a plug with $S_{wi} = 0$ is needed for a test, we use oil instead of brine in step 3 for saturation and skip step 5 as it is unnecessary.

4.3.8 Liquid Permeability Measurement Before Leak-off Test: After preparing the core plug, we measure its k_L using a modified coreflooding system and method described in our previous paper (Yousefi and Dehghanpour 2022). This method allows us to measure k_L of tight rocks much faster than the conventional methods. We inject oil at four different flowrates (0.06, 0.09, 0.12, and 0.15 cc/hr) and wait for the injection pressure to become stable before moving on to the next flow rate. The outlet port is open to the atmosphere, so the injection pressure reflects the pressure drop (ΔP) across the plug sample. After injecting oil at the highest Q (0.15 cc/hr), we repeat the process at the same flow rates to test for repeatability of the pressure readings at each Q. The k_L value is calculated using the Darcy equation and the slope of a straight line fit to the plot of Q vs. ΔP.

4.3.8.1 uncertainty analysis: To determine the uncertainty of a measured parameter $F(X_1,\ldots, X_n)$ which is a function of independent variables $X_1,\ldots, X_n$, a standard uncertainty, $U(F)$, is used

$$U^2(F) = \sum_{i=1}^{n}\left[\left(\frac{\partial F}{\partial X_i}\right)^2 u^2(X_i)\right] \tag{4-2}$$

where $u(X_i)$ is the standard uncertainty of variable X_i:

$$u^2(X_i) = \frac{s^2(X_i)}{N} + u_e^2(X_i) \tag{4-3}$$

$s^2(X_i)$ is the variance (square of standard deviation) of X_i, N is the number of measurements of X_i, and $u_e(X_i)$ is the standard uncertainty of X_i due to the measurement system. Standard deviation itself is expressed as:

$$s^2(X_i) = \frac{1}{N-1}\sum_{j=1}^{n}\left(X_{ij} - \bar{X_\iota}\right)^2 \tag{4-4}$$

Here, X_i is the value of each of the N measurements and X_i is the mean value of the N measurements (Bodaghia et al. 2014).

Using the Darcy equation and Eq. 4-2, the combined standard uncertainty of permeability can be written as:

$$\begin{aligned} U^2(k) = \left(\frac{\partial k}{\partial Q}\right)^2 u^2(Q) + \left(\frac{\partial k}{\partial \mu}\right)^2 u^2(\mu) + \left(\frac{\partial k}{\partial L}\right)^2 u^2(L) + \left(\frac{\partial k}{\partial P}\right)^2 u^2(P) \\ + \left(\frac{\partial k}{\partial A}\right)^2 u^2(A) \end{aligned} \tag{4-5}$$

For variables obtained by single measurements, their variances do not exist, so the standard uncertainty is determined only by the uncertainty due to the measurement system used. Thus Eq. 4-3 can be recast as

$$u^2(X_i) = u_e^2(X_i) \tag{4-6}$$

To calculate the uncertainty in permeability, we must determine each term of Eq. 5. We use a Chemix pump with a flowrate accuracy of 0.35% of the reading value. For pressure reading, we use a sensor with 0.1% of full scale (340 bar) reading accuracy. Length and Diameter measurements are done using a caliper with an accuracy of 0.01 cm. The viscosity measurement is done using a Brookfield viscometer with an accuracy of 0.02cp. Taking a derivative of k with respect to each parameter while the other ones are constant results in $\left(\frac{\partial k}{\partial Q}\right) = \frac{\mu L}{A\Delta P}$, $\left(\frac{\partial k}{\partial \mu}\right) = \frac{QL}{A\Delta P}$, $\left(\frac{\partial k}{\partial L}\right) = \frac{Q\mu}{A\Delta P}$, $\left(\frac{\partial k}{\partial \Delta P}\right) = -\frac{Q\mu L}{A(\Delta P)^2}$, and $\left(\frac{\partial k}{\partial D}\right) = -\frac{2*4*Q\mu L}{\pi\Delta P(D)^3}$. So,

$$\begin{aligned} U^2(k) = \left(\frac{\mu L}{A\Delta P}\right)^2 * \left(\frac{0.35}{100}Q\right)^2 + \left(\frac{QL}{A\Delta P}\right)^2 * (0.02)^2 + \left(\frac{Q\mu}{A\Delta P}\right)^2 * (0.01)^2 \\ + \left(-\frac{Q\mu L}{A(\Delta P)^2}\right)^2 * \left(\frac{0.1}{100}\Delta P\right)^2 + \left(-\frac{2*4*Q\mu L}{\pi\Delta P(D)^3}\right)^2 * (0.01)^2 \end{aligned} \tag{4-7}$$

Dividing both sides by k^2 gives

$$\left(\frac{U(k)}{k}\right)^2 = \left(\frac{0.35}{100}\right)^2 + \left(\frac{0.02}{\mu}\right)^2 + \left(\frac{0.01}{L}\right)^2 + \left(\frac{0.1}{100}\right)^2 + \left(\frac{2*0.01}{D}\right)^2 \tag{4-8}$$

$\frac{U(k)}{k}$ shows the relative error of the measured permeability. For our permeability measurement experiments, we use an oil sample with a viscosity of 5.65 cp, a core plug sample with a length of 6.7 cm, and a diameter of 3.8 cm. So, the relative error is $\frac{U(k)}{k} = 0.0185$. In other words, the accuracy of permeability measurement is approximately 2% of the reading value. For example, if the calculated the value of permeability is 2 µD, the measurement accuracy is 0.04 µD.

4.3.9 Leak-off, soaking, and flowback tests: We develop and apply an experimental protocol to simulate the leak-off, soaking, and flowback processes in the laboratory. **Figure 4-4** shows a schematic of a hydro-fractured horizontal well. The magnified section in Figure 4-4 shows the region next to the fracture face. The fracturing fluid (FF) leaks off into the matrix through the fracture face.

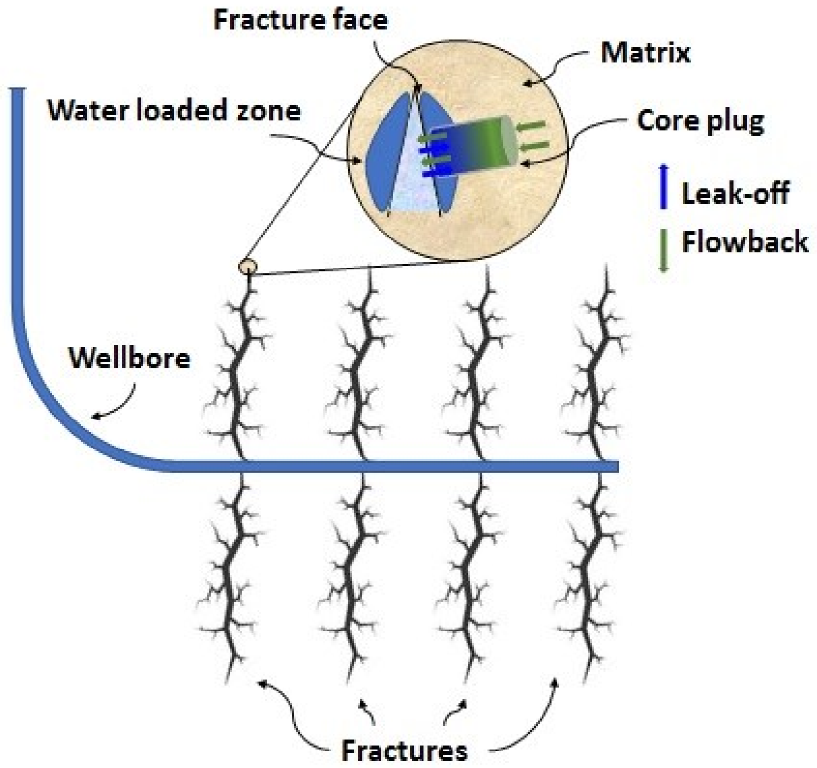

Figure 4-4: Schematic illustration of a hydro-fractured horizontal well (Yousefi et al. 2020).

During the flowback process, oil displaces the invaded fracturing fluid out of the rock matrix. Some part of the fracturing fluid is trapped inside the matrix and forms a water-loaded zone. The oil relative permeability is reduced in this area which hinders the oil production from the well. The use of surfactant solutions in fracturing fluids aims to remove this water blockage and to enhance oil production during the flowback and post-flowback stages. To simulate these processes in the laboratory, a plug sample is used with one side representing the fracture face through which the fracturing fluid leaks off into the matrix. We inject 1 PV of the surfactant solution into the plug at a constant Q of 0.06 cc/hr. Then, we close the outlet valve and soak the plug for one day at a pressure equal to the final pressure value reached at the end of the leak-off process. This step simulates the shut-in period in the field. Then, we inject oil at a constant Q of 0.06 cc/hr from the other end of the plug to displace the leaked off fluid and simulate the flowback process. We continue oil injection until no aqueous phase is produced and injection pressure becomes stable.

4.3.10 Liquid Permeability Measurement After Flowback Test: At the end of flowback test, we have an oil-saturated plug at residual aqueous-phase saturation. We use a similar method as described in section 3.8 to calculate k_L after the flowback process. We inject oil at four different flowrates and measure the stabilized ΔP at each Q. k_L is calculated from the slope of the straight line fit to the plot of Q vs. ΔP using the Darcy equation. The obtained k_L in this stage is referred to as regained k_L and will be compared to the k_L before the leak-off test to investigate the effect of different surfactant solutions on permeability of the core plug.

4.4 Results and Discussion

In this section, we present the results of the tests conducted based on our proposed laboratory protocol. We first present the results of IFT and CA measurements, and then, particle size distribution (PSD) measurements for various surfactant solutions and compare them to the pore-throat size distribution of the core plug to evaluate pore-throat blockage. We also present the critical micelle concentration (CMC) measurement and adsorption test results for four selected surfactant solutions and show scanning electron microscopy (SEM) images of the rock surface in the presence of these solutions for qualitative assessment of surfactant adsorption. Finally, we present the results of flooding experiments conducted through 9 defined tests to investigate the effect of S_{wi}, surfactant type and polarity, adsorption, IFT, and wettability on the pressure profile during the leak-off and flowback processes, as well as their effect on regained permeability.

4.4.1 IFT and Contact Angle Measurement: The results of IFT and CA measurements for the oil and surfactant solutions are shown in **Table 4-7**. The SS- 5 and SS-2 surfactant solutions with IFT values of 0.92 mN/m and 8.75 mN/m have the lowest and highest IFT values, respectively. The surfactants have been chosen in a way to cover a wide range of IFT values.

Table 4-7: IFT and CA measurement Results for oil and different surfactant solutions.

	Tap Water	SS-1	SS-2	SS-3	SS-4	SS-5	SS-6	SS-7
IFT (mN/m)	13 ±0.35	5.35 ±0.32	8.75 ±0.13	3.9 ±0.11	5.52 ±0.36	0.92 ±0.31	2.37 ±0.02	6.34 ±0.14
CA	115 ±3.5	45.5 ±4.2	98.1 ±3.1	72.7 ±2.5	82.9 ±1.3	-	124 ±0.6	53.1 ±0.5

The CA of tap water-oil-rock system is around 115°, indicating that the rock, which has been aged in oil, is preferentially oil wet when no chemical is used to alter its wettability. SS-6 surfactant solution has no significant effect on CA. SS-1, SS-3, and SS-7 make the rock water wet, while SS-2 and SS-4 make the rock neutral wet. The CA measurement of SS-5 solution was not successful because the droplet of oil quickly spreads on the rock surface due to low IFT of SS-5 solution. The chosen surfactants can create a wide range of wettability from oil wet to neutral wet to water wet state.

4.4.2 Particle Size Distribution Measurement: **Figure 4-5** illustrates the particle size distribution for the structures formed inside different surfactant solutions, as well as the pore-throat size distribution of the plug sample for comparison. These structures may include lamellar sheets, vesicles, cylindrical micelles, spherical micelles, or reverse micelles (Massarweh and Abushaikha 2020; Cornwell 2018). The figure shows that, except for SS-7, the probability of formation damage caused by blockage of the pore-throats by the structures inside the surfactant solutions is minimal, as the structures are much smaller than the average pore-throat size.

However, the coreflooding results for SS-7 indicate that it may cause blockage of the pore throats of the core sample during the leak-off stage due to the particles being approximately the same size as the pore throats. **Figure 4-6** shows the pressure profile measured during leak off the SS-7 solution. The leak off test was stopped after 1 day because of pore throat blockage and rapid pressure increase. The other surfactant solutions do not result in pore-throat blockage because the structures inside the injected solution are much smaller than the pore throats.

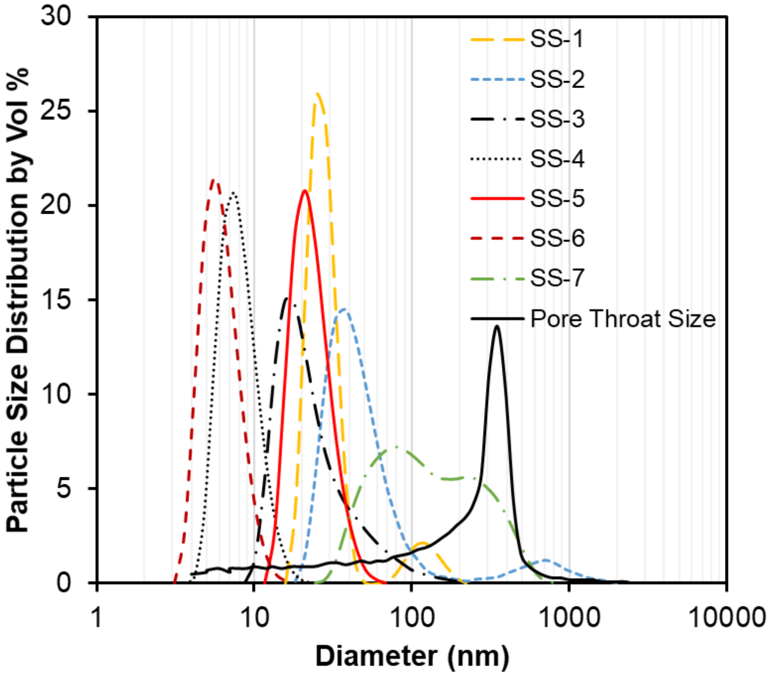

Figure 4-5: Particle size distribution of structures formed inside surfactant solutions compared to the pore-throat size distribution of the rock sample.

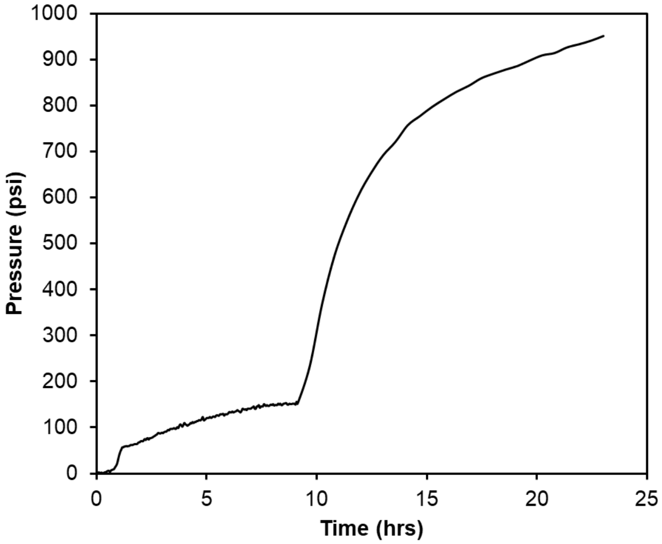

Figure 4-6: Pressure profile during leak-off process using SS-7. The test was stopped after 1 day because of the rapid pressure increase.

4.4.3 Critical Micelle Concentration Measurement and Surfactant Adsorption Tests:

The interaction between surfactant solution and the rock surface depends on the surfactant charge and the type of minerals presented in the rock. Here, we test the effect of surfactant polarity on adsorption on the surface of our rock sample by using different surfactants with varying polarities. We choose SS-1 (anionic), SS-2 (slightly anionic), SS-3 (non-ionic), and SS-5 (non-ionic) for adsorption tests. As discussed before, we use the surface tension measurement technique to measure surfactant concentration inside a solution (Belhaj et al. 2021). We prepare solutions with different concentrations of surfactant and measure the surface tension. From these measurements, we create a calibration curve that shows the relationship between surface tension and surfactant concentration. We find the CMC of the surfactant solution from that calibration curve. The concentration after which the surface tension remains constant is the CMC of that surfactant solution (Hu et al. 2010). **Figure 4-7** depicts the calibration curve which shows the change of surface tension with concentration of the four surfactant solutions. The CMC of SS-1 is around 2 gpt while the CMC of SS-2, SS-3, and SS-5 are around 1gpt.

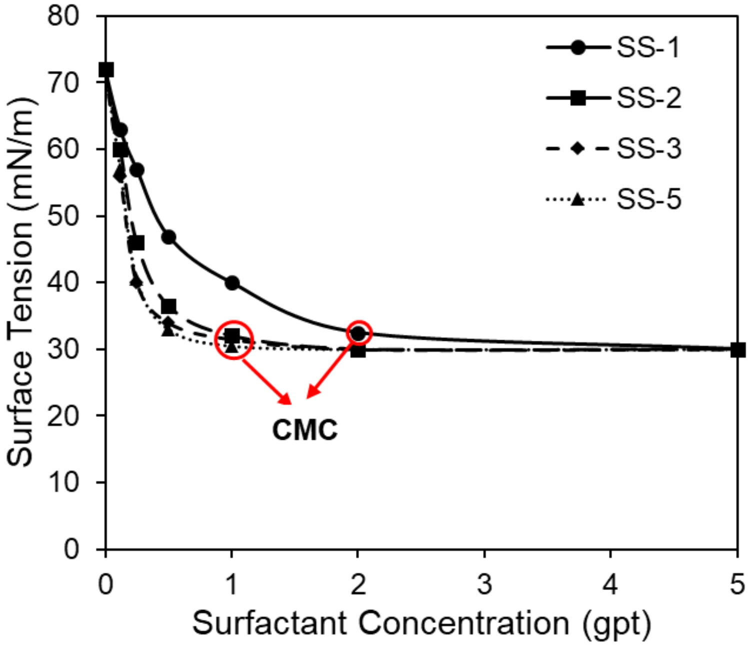

Figure 4-7: Calibration curve which shows the surface tension vs. surfactant concentration to relating the measured surface tension to the concentration of surfactant in the solution.

We perform the surfactant adsorption tests on these four surfactant solutions as described in section 4.3.6. After the adsorption test, we filter the solutions and measure their surface tension again. The calibration curve in Figure 4-7 relates the measured surface tension to the concentration of remaining surfactant in the solution after adsorption. **Table 4-8** lists the surface tension values of the surfactant solutions before and after the adsorption tests. Using the concentration difference from the calibration curve, we calculate the amount of adsorption (mg of surfactant per gr of rock powder) for each surfactant. SS-3, a non-ionic surfactant, has the highest adsorption among the tested surfactants, while SS-1, an anionic surfactant, has the lowest. The low adsorption of SS-1 may be due to the electrochemical repulsion between the hydrophilic head of the surfactant and the negatively charged quartz minerals on the rock surface, which make up 40% of the rock minerals (Liu et al. 2020). Non-ionic surfactants, on the other hand, do not have surface charges and their adsorption is driven by van der Waals attraction and hydrogen bonds, which could explain the high adsorption of SS-3 (Kamal et al. 2017).

Table 4-8: Surfactant adsorption test results for 4 different surfactant solutions.

Properties	SS-1	SS-2	SS-3	SS-5
Surfactant Type	Anionic	Slightly Anionic	Non-ionic	Non-ionic
Surface Tension before Adsorption (mN/m)	32±0.8	40±0.3	31.5±0.3	30.5±1.7
Surface Tension after Adsorption (mN/m)	34±0.5	43.1±0.1	32.9±0.4	31.7±0.6
Adsorption (mg/g)	4	4.3	5.5	4.5

4.4.4 SEM Imaging:

We use SEM imaging to observe the surfactant adsorption on the rock surface. We use 3 pieces of the rock sample and wash them with toluene and methanol. Then, we dry them inside the oven at 90°C. One of the samples serves as a reference case representing the clean rock surface, while the second and third samples are saturated with SS-1 and SS-3, respectively. SS-1 shows the lowest surfactant adsorption and SS-3 shows the highest. After saturation with surfactant solutions, the samples were dried in the oven again. **Figure 4-8** shows the surface of a rock at the same level of magnification in three different scenarios. Figure 4-8a depicts a clean rock surface with no attached agglomerated structures. In contrast, Figure 4-8b illustrates that certain areas of the rock surface are covered in white structures resulting from adsorption of SS-1 onto the rock surface. Lastly, Figure 4-8c displays the scenario with the greatest amount of surfactant adsorption, where nearly the entire rock surface is covered with adsorbed surfactant SS-3.

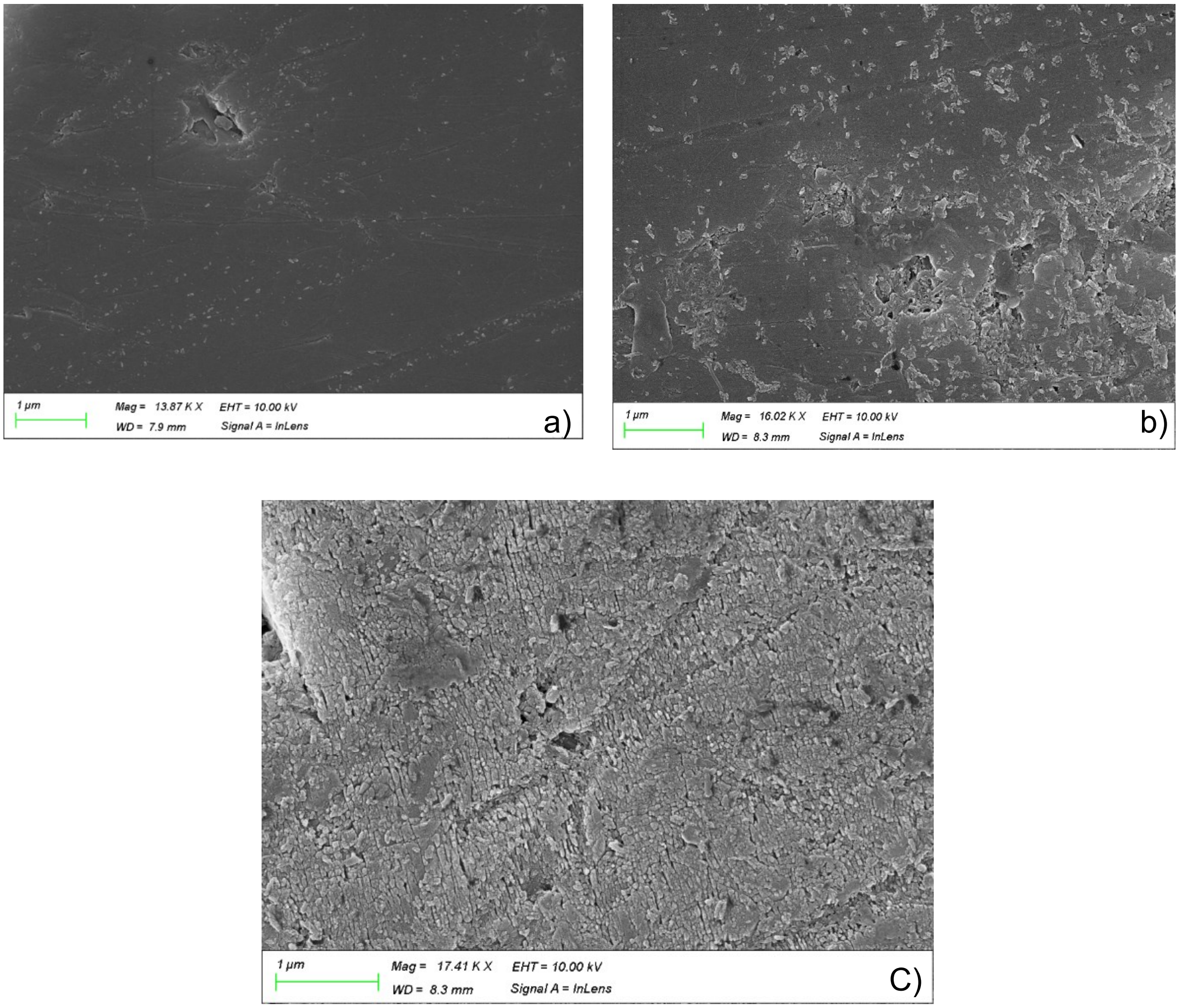

Figure 4-8: SEM images of rock surface. a) clean surface of the rock as a reference case. b) low adsorption of SS-1 on the rock surface. c) high adsorption of SS-3 on the rock surface.

4.4.5 Leak-off and Flowback Tests: In this study, we conduct 9 leak-off and flowback tests using 7 different surfactant solutions at different S_{wi} values to investigate the effect of S_{wi}, surfactant type and polarity, surfactant adsorption, IFT and wettability on regained permeability after flowback. We also use tap water without any surfactant as the base case. To investigate the effect of S_{wi}, we prepare the core plugs either with no S_{wi} or with $S_{wi} \approx 30\%$. The later S_{wi} is established after injecting 3 to 5 PV of oil into the brine-saturated sample. It should be noted that the observed results are for tests on our core plug sample with the mineralogy shown in Table 4-5. If a different rock sample is used for tests, different results might be obtained. The results observed are also limited to the surfactants used in this study and can not be generalized for other surfactants.

4.4.5.1 Effect of Initial Water Saturation: In this part, we examine the impact of S_{wi} on the regained permeability by comparing the results of flooding experiments using tap water at two different initial water saturations. The workflow of the tests is shown in Figure 4-3.

4.4.5.1.1 Test 1, tap water as leak-off fluid, $S_{wi} = 0$: After cleaning and drying the core sample, we saturate it with oil and measure the oil permeability of the fully saturated plug. **Figure 4-9** shows the result of permeability measurement at 4 different flowrates using the dead oil sample. We use the slope of the straight line in the graph of Q vs. ΔP, oil viscosity, and the plug dimensions to calculate the absolute permeability of the plug. Based on the Darcy equation, the permeability of plug 1 is $k = 3.2\ \mu D$. After initial permeability measurement, we inject 1 PV of tap water as the leak-off fluid. Then, we soak the plug at high pressure for one day. After that, we inject the oil from the other side of the plug to simulate the flowback process. **Figure 4-10** shows the pressure profile during the leak-off, soaking, and flowback processes for plug 1.

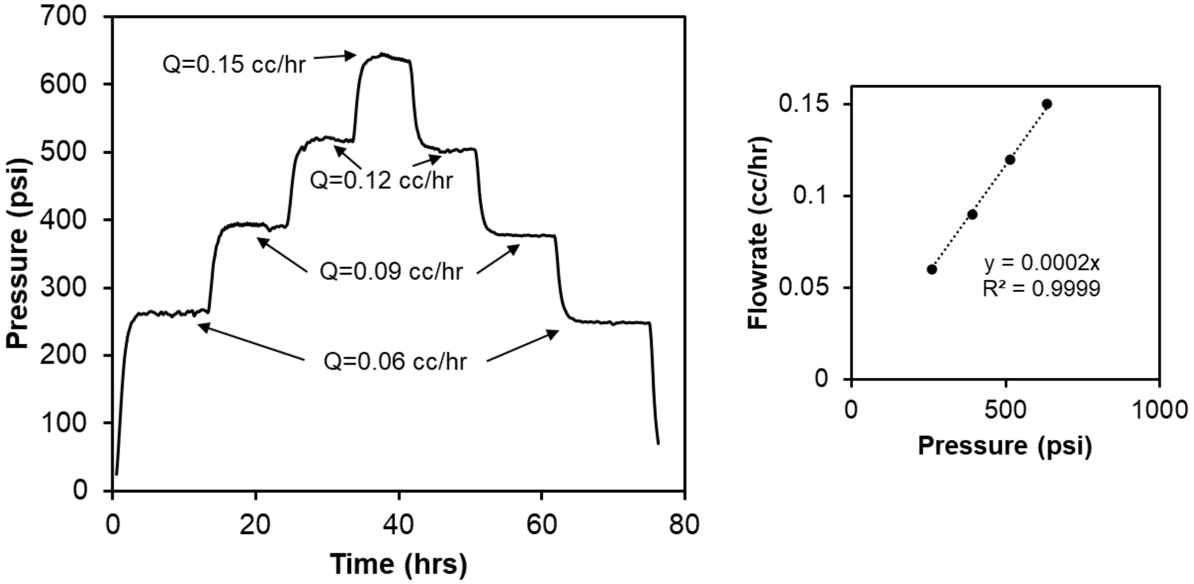

Figure 4-9: Initial permeability measurement of the plug for Test 1 using oil at $S_{wi} = 0$.

During the leak-off and flowback periods, the mobility of two phases decreases since two phases flow alongside inside the core plug. Therefore, to maintain a constant flowrate, the injection pressure must increase. In test 1, the observed hump in pressure is bigger in flowback period compared to the one in leak-off stage. The contact-angle value (*CA = 115°*) indicates that the rock is oil-wet, because during the preparation stage, the plug was saturated with oil and aged for 1 week at a relatively high pore pressure (*P = 1200 psi*). Wettability dictates the pore-scale fluid distribution. The wetting phase occupies small pores and coats the surface of the grains, while the nonwetting phase occupies larger pores and is located at the center of the pores (Peters 2006). Therefore, the oil phase, which is the wetting phase, preferentially occupies smaller pores and covers the surface of the rock. During the leak off process, tap water, which is the nonwetting phase, occupies relatively larger pores. During the flowback process, the injected oil flows through smaller pores, which require a higher entry pressure. Some part of the tap water becomes also trapped in large pores through the snap-off mechanism, which reduces the oil permeability. As a result, the injection pressure increases to maintain the constant injection flowrate of the oil.

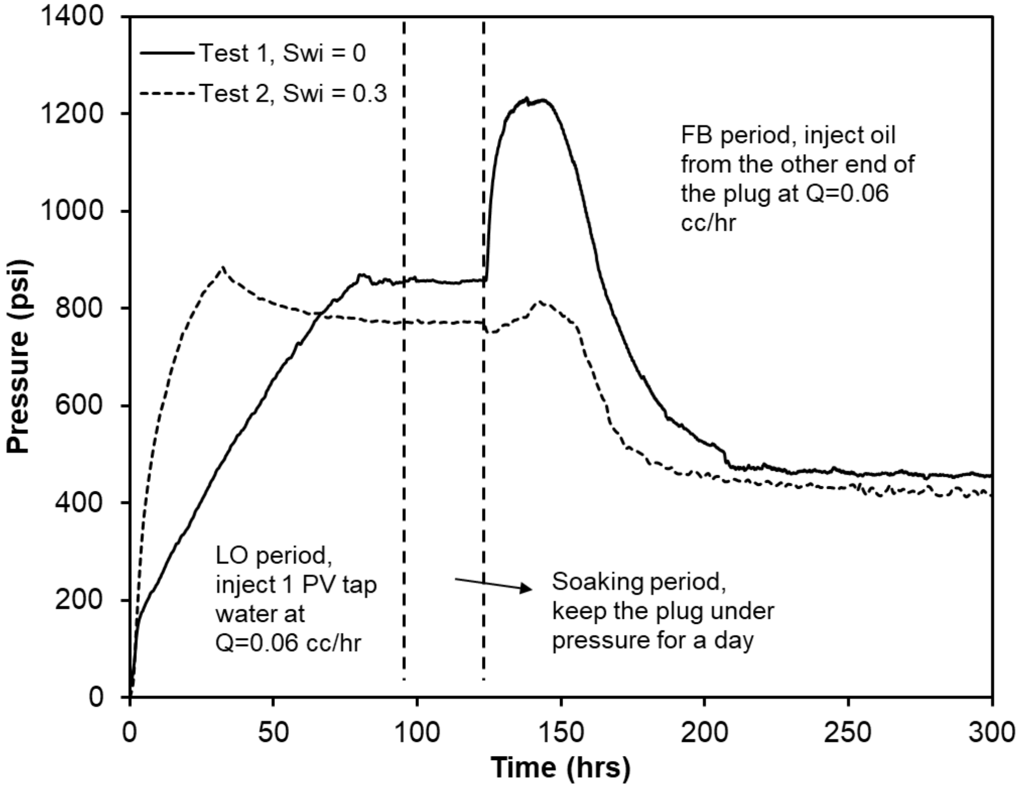

Figure 4-10: The pressure profiles measured during leak off, soaking, and flowback processes for Tests 1 and 2.

At the end of the flowback period, when the pressure becomes stable, we measure the permeability of the rock sample again. The regained permeability for this test is *2.5 μD.* To compare the regained

k_L with the initial k_L, we introduce a regained permeability index as:

$$I_k = \frac{\text{regained } k_L}{\text{initial } k_L} \tag{4-9}$$

For test 1, $I_k = 0.78$, which shows a reduction of 22% in permeability. The main cause of the permeability reduction is the increase in water saturation in the rock due to water trapping. Initially, the plug has no S_{wi}, but after flowback, S_{Wirr} is around 30%. The increase in S_w reduces the effective permeability to the oil phase.

4.4.5.1.2 Test 2, tap water as leak-off fluid, $S_{wi} \approx 30\%$: For Test 2, the preparation steps for the plug are slightly different from those for Test 1. After cleaning and drying the plug, we saturate it with brine and age it under pressure for 1 week. We then inject oil at a constant flowrate of $Q = 0.06\ cc/hr$ to displace the brine out of the plug. The injection is stopped when the pressure stabilizes, and S_w reaches its irreducible value of $S_{wirr} = 30\%$.

Now, we measure the permeability with oil at S_{wi}, as we did in Test 1. The permeability before the leak-off process for plug 1 is $2.2\ \mu D$. We then use tap water as the leak-off fluid and inject 1 PV of it into the plug at a constant flowrate of $Q = 0.06\ cc/hr$, followed by soaking the sample at the pore pressure reached at the end of leak-off period for one day. After soaking, we inject oil from the other end of the plug to displace the water. Figure 4-10 shows the pressure profile during the leak off, soaking, and flowback processes for Test 2. In test 2, the plug is initially saturated with brine and aged at 1200 psi for 1 week. The contact angle value ($CA = 105°$) suggests that the rock is close to neutral wet when the core plug is initially saturated with brine. Since the wettability affects the pore-scale fluid distribution, the irreducible water will cover the rock surface. During the leak-off process, the water is injected into the core plug at a constant flowrate. The water phase may occupy parts of the pore-network with high surface to volume ratio such as the continuous path of water film on the rock surface and smaller pores. On the other hand, the water flows at a higher saturation compared to Test 1, which means a higher water relative permeability and a lower injection pressure. These two factors mask each other's effect in a way that the injection pressure is just slightly higher at breakthrough time and drops after that due to higher water saturation. During the flowback, oil is injected at a constant flowrate. The measured wettability condition suggests that oil flows through parts of the pore network with relatively lower surface to volume ratio like larger pores. Therefore, the hump in the pressure profile during the flowback is smaller than the hump observed in Test 1.

At the end of the flowback period when pressure becomes stable, we measure the permeability of the rock sample once more. The regained permeability for this test is *1.9 μD.* Comparing the regained k_L with the initial k_L shows I_k = 0.86 which means a reduction of 14% in permeability. When we compare the leak-off periods of Tests 1 and 2, we see that the leak-off fluid has a faster breakthrough in Test 2 because there is already an irreducible water saturation inside the plug.

4.4.5.2 Effect of Surfactant Polarity: In this part, we examine the impact of surfactant polarity on the regained permeability by comparing the results of flooding experiments using an anionic (SS-1), a slightly anionic (SS-2), and a non-ionic (SS-3) surfactant as leak-off fluids. We do not include the cationic and zwitterionic surfactants in our analysis due to their limited applications for EOR purposes. For Test 3, we use an anionic surfactant to be injected during the leak-off period. The permeability before leak-off test is 2.6 μD which decreases to 2.1 μD after the flowback process *(*I_k = 0.81). Anionic surfactants have negatively charged hydrophilic heads. Generally, they are used in sandstone reservoirs where the rock surface is negatively charged. The methodology for all the upcoming tests is similar to that for Test 2. The only difference is the type of leak-off fluid. For Test 4, we use a surfactant with a weaker surface charge to compare it with Test 3 to investigate the effect of surface charge density. Here, we use SS-2 which is a slightly anionic surfactant. The initial permeability before leak-off stage is 2.6 μD which increases to 2.6 μD after flowback *(*I_k = 1). For Test 5, we use a non-ionic surfactant (SS-3) to be injected during leak-off period. The permeability changes from 2.6 μD before the leak off period to 2.6 μD after the flowback process *(*I_k = 1).

Figure 4-11 shows the pressure profile during the leak of, soaking, and flowback processes for Tests 3, 4, and 5. The SS-1 reduces the IFT to 5.35 mN/m and makes the rock water wet with contact angle of 45°. Comparing the pressure profile during flowback period with that of test 2 shows a smaller hump when SS-1 is used. It could be due to IFT reduction and wettability alteration toward water-wet condition. SS-2 reduces the IFT to 8.75 mN/m and alters the wettability toward neutral wet (CA = 98°). SS-2 has the lowest adsorption, slightly less than that of SS-1 (4 mg/gr for SS-2 vs. 4.3 mg/gr for SS-1). The interesting observation is that the regained permeability does not decrease after the flowback process. We do not observe a hump in pressure profile during flowback and pressure decreases with time as oil displaces the leak-off fluid out of the core plug. SS-3 has the highest adsorption value (5.5 mg/gr). It reduces the IFT value to 3.9 mN/m and changes the wettability toward water-wet conditions (CA = 73°). Although we observe a hump in the pressure profile, which might suggest the water blockage, the regained permeability after the flowback process is bigger than that before the leak-off. Reducing IFT to lower values is responsible for reducing the capillary pressure and better displacement of water out of the core plug during the flowback process. The results suggest that surfactant adsorption does not have a detrimental effect on regained permeability.

Comparison of the pressure profiles for Tests 3, 4, and 5 suggests that surface charges of the surfactants have a negative effect on the regained permeability. The case with the least permeability damage after flowback is the one with non-ionic surfactant whereas the worst one is Test 3 with anionic surfactant used as the leak-off fluid.

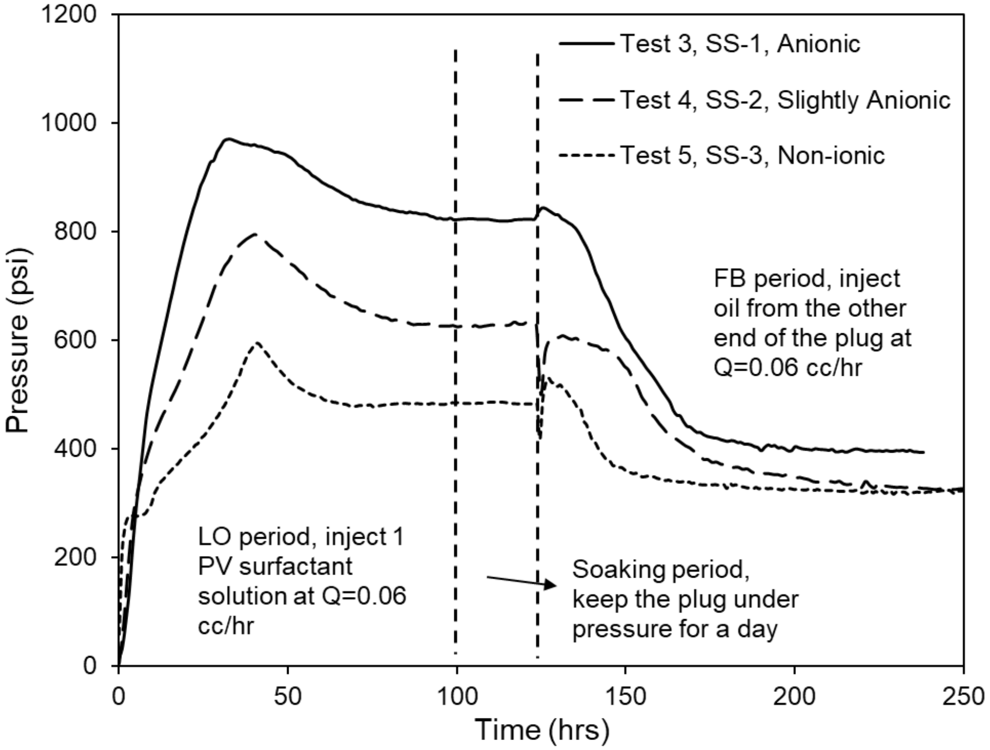

Figure 4-11: The pressure profile during the LO, soaking, and FB processes for Tests 3, 4, and 5. An anionic, slightly anionic, and a non-ionic surfactant are used for Tests 3, 4, and 5, respectively.

4.4.5.3 Effect of Surfactant Adsorption: In this part, we examine the impact of surfactant adsorption on the regained permeability. We conduct the surfactant adsorption test on three surfactant solutions of SS-1, SS-2, and SS-3 using the methodology discussed in section 4.3.6. SS-3 which is a non-ionic surfactant has the highest adsorption value of 5.5 mg/gr. SS-1 which is an anionic surfactant has an adsorption value of 4.3 mg/gr compared to the 4 mg/gr of SS-2 surfactant solution. Figure 4-11 shows the pressure profile during leak-off, soaking, and flowback for these three surfactant solutions. The results suggest negligible effects of surfactant adsorption on regained permeability.

4.4.5.4 Effect of Interfacial Tension and Contact Angle: In this part, we present Tests 6, 7, and 8 using SS-4, SS-5, and SS-6 respectively.

4.4.5.4.1 Test 6, SS-4 as the leak-off fluid, $S_{wi} \approx 30\%$: For the Test 6 we use a non-ionic surfactant as the leak-off fluid. **Figure 4-12** shows the pressure profile during leak-off, soaking, and flowback for Test 6.

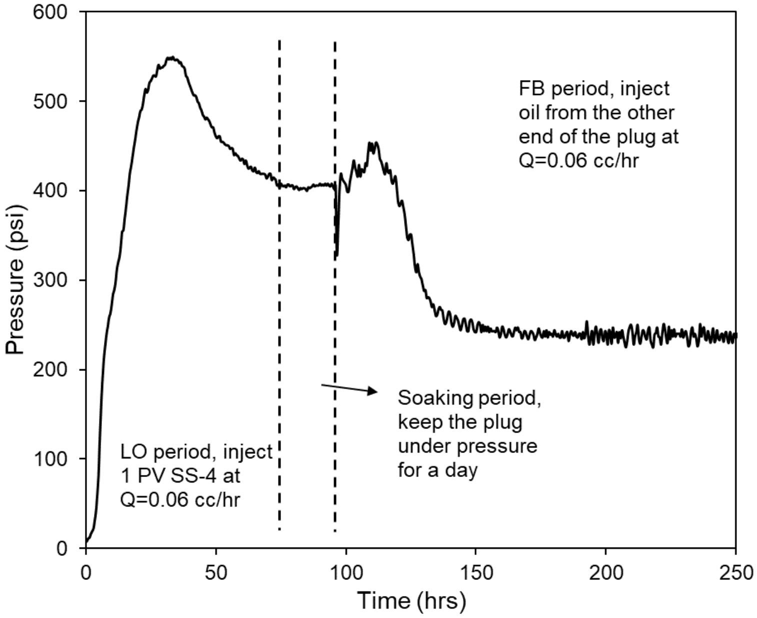

Figure 4-12: The measured pressure profile during leak-off, soaking, and flowback processes for Test 6.

SS-4 reduces the IFT value to 5.5 mN/m and changes the wettability toward neutral-wet conditions (*CA = 83°*). The regained permeability after flowback is equal to the permeability before leak-off stage (*k = 2.6 µD)*. The hump in pressure profile during the flowback process is smaller than that during the leak off process.

4.4.5.4.2 Test 7, SS-5 as the leak-off fluid, $S_{wi} \approx 30\%$: For the Test 7, we use another anionic surfactant (SS-5) for the leak-off period. SS-5 reduces the IFT to a very low value (IFT = 0.92 mN/m). Since the IFT is very low, the small oil droplets quickly spread on the rock surface, making the contact angle measurement unsuccessful. The adsorption value is also moderate (4.5 mg/gr).

Figure 4-13 shows the pressure profile measured during leak off, soaking, and flowback of Test 7. Low IFT is responsible for very small observed hump in the pressure profile during the flowback process. The regained permeability after flowback is equal to that before the leak-off stage (*k = 2.6 μD)*.

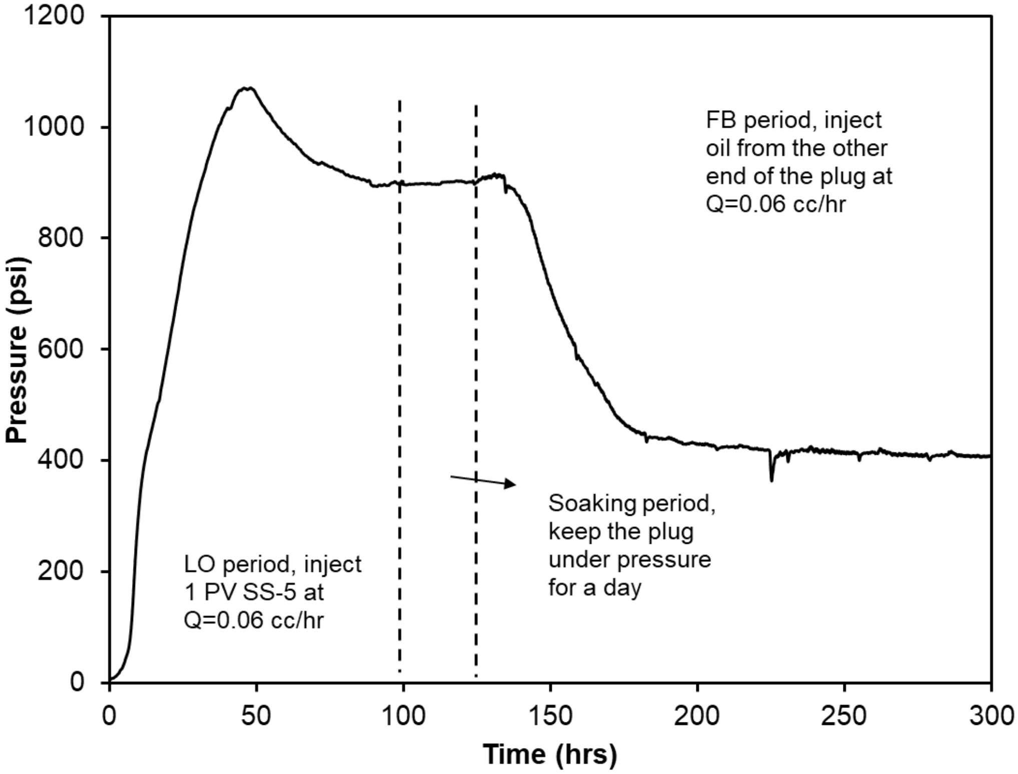

Figure 4-13: The measured pressure profile during leak off, soaking, and flowback processes for Test 7.

4.4.5.4.3 Test 8, SS-6 as leak off fluid, Swi ≈ 30%: For the Test 8 we use another anionic surfactant (SS-6) to be injected during leak off period. SS-6 reduces the IFT to 2.37 mN/m and changes the wettability toward oil wet (*CA = 124°*). **Figure 4-14** shows the pressure profile during leak off, soaking, and flowback for Test 8. The permeability decreases from *2.7 μD* before leak-off to *2.4 μD* after flowback. The pressure hump observed during flowback is bigger than that during leak off.

Surfactant solution SS-2, SS-3, and SS-4 changed the wettability towards neutral wet state. These surfactant solutions do not cause any reduction on regained permeability. On the other hand, SS-1 solution changed wettability toward water-wet state and SS-6 changed the wettability toward oil-wet state. Both of these surfactant solutions decreased the regained permeability. The effect of IFT on regained permeability is not straightforward to observe. For example, SS-4 with IFT = 5.52 mN/m and SS-5 with IFT = 0.92 mN/m have not reduced the regained permeability after flowback.

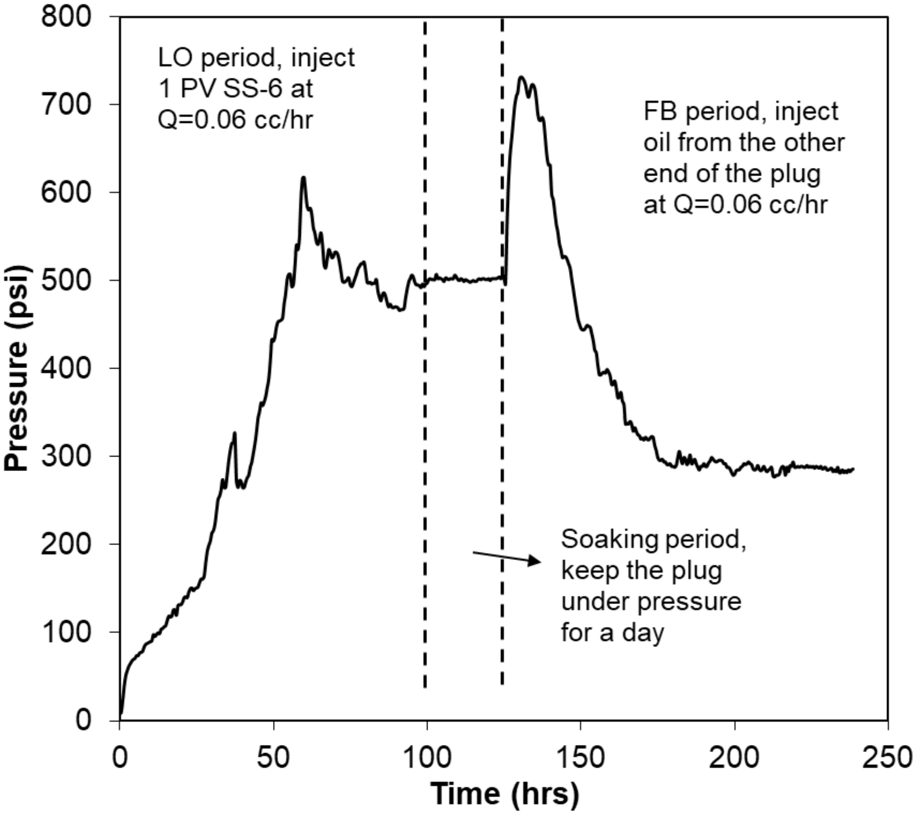

Figure 4-14: Pressure profile during leak off, soaking, and flowback processes for Test 8.

The effects of IFT and CA can be combined in the dimensionless capillary number (N_{ca}) as shown in Eq. 10.

$$N_{ca} = \frac{\mu . V}{\sigma . \cos(CA)} \tag{4-10}$$

Table 4-9 shows the calculated N_{ca} and regained permeability index (I_k) for Tests 3 to 8 where 7 different surfactant solutions are used for injection into the core sample.

Table 4-9: Calculated N_{ca} and I_k for Tests 3 to 8 using SS-1 to 6.

Surfactant Solution	SS-1	SS-2	SS-3	SS-4	SS-5	SS-6
N_{ca}	0.44×10^{-8}	1.28×10^{-8}	1.37×10^{-8}	2.26×10^{-8}	1.71×10^{-8}	1.23×10^{-8}
I_k	0.81	1	1	1	1	0.92

Using the N_{ca} combines the effects of IFT and CA that shows a clear trend between N_{ca} and I_k. At Nca > 1.23×10^{-8}, No damage to the permeability of the rock sample is observed while at Nca < 1.23×10^{-8}, the smaller the N_{ca}, the higher the magnitude of the permeability damage.

4.5 Summary

In this study, we developed and applied a comprehensive laboratory protocol on a core plug from the Montney Formation for screening surfactant solutions used in hydraulic fracturing operations. In this protocol, we simulate leak-off and flowback processes under reservoir pressure and saturation conditions. First, we investigated the effects of initial water saturation (S_{wi}) on water blockage and phase trapping. Then, we investigate the effect of surfactant polarity, surfactant adsorption, IFT, and contact angle on regained permeability after the flowback process. We used 7 different surfactant solutions as the leak-off fluids and compared the regained permeability after the flowback process with the permeability before the leak-off process to investigate each surfactant solution's effectiveness on removing water blockage. We also used tap water for the leak-off process as the reference case for comparative analysis. We also measured the mean size of structures formed in the surfactant solutions and compared it with the pore-throat size distribution of the plug to investigate the possibility of pore-throat blockage. Here is the summary of the key findings:

- Mean size of particles formed in all the surfactant solutions except SS-7 are less than 100 nm. Analyzing the pore-throat size distribution of the plug from MICP test shows that more than 90% of pore throats are bigger than the size of formed structures inside the surfactant solutions. So, there is minimal chance of pore-throat blockage by adding those surfactant solutions in water. SS-7 with bigger particles, plugged the core sample during leak-off process and caused a rapid pressure increase, leading to the test failure. Therefore, particle size of surfactants should be compared to the pore throat sizes available as a screening criterion to omit the surfactants that have a higher chance of plugging. This is an important step that should be done before any other experiments.
- All the non-ionic surfactants (SS-3, SS-4, SS-5) and even the slightly anionic surfactant (SS-2) led to minimum permeability damage. The regained permeabilities for those surfactants were equal to the initial permeability before the leak-off stage. On the other hand, all the anionic surfactants (SS-1, SS-6, SS-7) caused damage and reduced the

regained permeability. So, the type of the surfactant used in the fracturing fluid can Significantly affect on the regained permeability. It should be noted that, the observed results are for the core plug with reported mineralogy in the text. Other rock samples may show different results using similar surfactant solutions. The effect of different surfactant types with different polarities should be investigated using flooding experiments as a screening step for choosing proper surfactant solutions for a specific rock type.

- The selected non-ionic surfactants showed higher surfactant adsorptions while they did not decrease the regained permeability. Surfactant adsorption for investigated surfactant solutions on the specific rock sample in this study showed that surfactant adsorption was not detrimental to the surfactant's functionality.
- The effect of IFT on regained permeability was not straightforward. The effect of IFT should be seen in conjunction with other aspects of the surfactants. For example, SS-6 reduced the IFT to 2.39 mN/m, much lower than the IFT of SS-2, but its regained permeability index was smaller since it changed the wettability toward the oil-wet state.
- The non-ionic surfactants (SS-3 and SS-4) and also the slightly anionic surfactant (SS-2) changed the wettability toward neutral-wet conditions. These surfactants exhibited minimum damage with maximum regained permeability index. It suggests that surfactants that change the wettability towards neutral-wet conditions have higher regained permeability index.
- Combining the effect of IFT and wettability in dimensionless parameter of N_{ca} shows that for $N_{ca} > 1.23\times10^{-8}$, the regained permeability index is equal to one, which means no damage to the permeability. Below that threshold, the smaller the N_{ca}, the smaller the regained permeability index, which means more damage to the permeability.
- In Test 1 with $S_{wi} = 0$, regain permeability dropped 22% compared to the initial permeability while in Test 2 with $S_{wi} = 0.3$, regained permeability dropped 14% compared to its initial value. We used tap water as the leak off fluid for the two tests. If a reservoir is at sub-irreducible water saturation conditions, the surfactant solutions may reduce the regain permeability because of an increase in water saturation inside the rock after leak-off and flowback processes. Therefore, when screening tests are done on a surfactant solution for a specific reservoir, the initial water saturation should be considered in the test design.

Chapter 5

Conclusions and Recommendations

In this thesis, we develop new methods for tight rock characterizations. We used them to study single-phase and two-phase flow through tight rocks with the aim of permeability and relative permeability determination. After that we proposed a comprehensive experimental protocol to mimic leak-off and flowback processes during hydraulic fracturing. This protocol can be used to screen different chemical additives in the fracturing fluid.

In chapter 2, we used the diffusivity equation to explain why the steady-state method of permeability measurement is time consuming for low-permeability media. We altered the influx boundary condition to model the measured pressure data during permeability measurement of a tight rock sample with error of less than 5%. Based on the model results, we modified the conventional coreflooding device to reduce the time of permeability measurement of tight rock samples. The modified device is used to measure the permeability of a tight rock sample and the model can match the measured data with a very good accuracy. Here is the summary of the key findings:

- A new semi-analytical solution for diffusivity equation is presented which accounts for logarithmic pressure profile as initial condition, storage effect, pressure dependency of permeability, and high-pressure drawdown values in case of experiments done on low-permeability porous media.
- A device for permeability measurement of tight rocks is designed by modifying conventional coreflooding apparatus. The tests conducted using the modified device confirm the modeling results and shows a considerable decrease in time of experiments.
- The main reason that makes the steady-state method time consuming is the accumulator “storage effect”. When injection pressure increases (or decreases) with time, compaction (or expansion) of the fluid inside the accumulator induces an excess flowrate that causes the influx flowrate into the plug to be lower (or higher) than the pump-induced flowrate. It takes some time for the influx flowrate to become equal to the pump-induced flowrate.
- When dealing with low-permeability tight rocks, the compressibility-induced flowrate could be in the order of pump flowrate and cannot be neglected.

- Ignoring the pressure dependency of the rock permeability does not result in significant errors in the model while making the model much simpler.
- In the modified coreflooding device, reduction of accumulator volume from 500 cc to around 10 cc causes a fiftyfold decrease in the time required for steady state establishment.

In chapter 3, we presented a simple mathematical technique based on frontal advanced theory to model the pressure profile during a two-phase immiscible displacement in a tight porous medium. Combining this technique with the pressure profile measured during the displacement process and considering some simplifying assumptions, we measured the k_r values for the two phases. We used the measured k_r values to tune the parameters of the modified Brooks and Corey (MBC) relative permeability model. We performed waterflooding and leak-off/flowback experiments on tight rock samples to verify and show the application of the proposed method. We used the tuned MBC k_r model to predict the observed pressure profile after breakthrough during a waterflooding experiment. Comparing the modeled and measured pressure profiles shows a mean absolute percentage error (MAPE) of less than 3%. At the end, we investigated the shape of the pressure profile during an immiscible displacement from flow-work point of view. The effect of S_{wi} and *IFT* on the amount of work needed during the displacement process was discussed. Here is the list of conclusions:

- In the JBN method, the pressure drop during the immiscible displacement is calculated using an integral term in which the change of k_r with S_w is considered. We proposed a simplifying assumption to calculate the pressure drop using k_r values at $\overline{\mathrm{S_w}}$ behind each saturation front before its breakthrough. Using this assumption makes the pressure drop calculation much easier by introducing just 2% and 6% errors when the mobility ratio is 1 and 10, respectively.
- The proposed model for pressure drop explains the observed hump in the pressure profile during a two-phase immiscible displacement process. Any factor that disturbs the stability of the front, will cause a deviation from piston-like displacement, and hence, will cause a bigger hump in the pressure profile.
- We assume that the minimum point on the total mobility (M_o+M_w) curve coincides with the point of intersection between the M_o and M_w curves. The error associated with this

assumption is less than 10% for the example mentioned in the manuscript. The more symmetric the mobility curves are, the less the error associated with this assumption is. This assumption enables us to determine k_r values for both oil and water phases from a measured pressure profile during an immiscible displacement process.

- We conducted a waterflooding experiment on a tight rock sample, used *the* P_{max} of the pressure profile to calculate k_r values for oil and water, and used those values to tune the MBC k_r model. We used the tuned model to predict the pressure profile after the water breakthrough. The mean absolute percentage error (MAPE) between modeled and measured pressure data is less than 3%.
- We proposed a new explanation for the shape of the pressure profile from flow-work perspective. A bigger hump in the pressure profile suggests more work is required for the displacement process. We used the measured data of leak-off and flowback tests done on a low-permeability tight plug for this analysis. A bigger pressure hump in our tests corresponds to a lower production rate for a well that produces under constant bottomhole pressure. Therefore, factors such as high mobility ratio, high capillary force, high IFT, and a higher degree of rock heterogeneity causing a bigger hump, will cause a lower production flowrate for the well.
- Using the flow-work concept, a new explanation was presented regarding the effect of IFT reduction on water blockage removal.

In Chapter 4, we developed and applied a comprehensive laboratory protocol on a core plug from the Montney Formation for screening surfactant solutions used in hydraulic fracturing operations. In this protocol, we simulate leak-off and flowback processes under reservoir pressure and saturation conditions. First, we investigated the effects of initial water saturation (S_{wi}) on water blockage and phase trapping. Then, we investigate the effect of surfactant polarity, surfactant adsorption, IFT, and contact angle on regained permeability after the flowback process. We used 7 different surfactant solutions as the leak-off fluids and compared the regained permeability after the flowback process with the permeability before the leak-off process to investigate each surfactant solution's effectiveness on removing water blockage. We also used tap water for the leak-off process as the reference case for comparative analysis. We also measured the mean size of structures formed in the surfactant solutions and compared it with the pore-throat size distribution of the plug to investigate the possibility of pore-throat blockage. Here is the summary of the key findings:

- Mean size of particles formed in all the surfactant solutions except SS-7 are less than 100 nm. Analyzing the pore-throat size distribution of the plug from MICP test shows that more than 90% of pore throats are bigger than the size of formed structures inside the surfactant solutions. So, there is minimal chance of pore-throat blockage by adding those surfactant solutions in water. SS-7 with bigger particles, plugged the core sample during leak-off process and caused a rapid pressure increase, leading to the test failure. Therefore, particle size of surfactants should be compared to the pore throat sizes available as a screening criterion to omit the surfactants that have a higher chance of plugging. This is an important step that should be done before any other experiments.
- All the non-ionic surfactants (SS-3, SS-4, SS-5) and even the slightly anionic surfactant (SS-2) led to minimum permeability damage. The regained permeabilities for those surfactants were equal to the initial permeability before the leak-off stage. On the other hand, all the anionic surfactants (SS-1, SS-6, SS-7) caused damage and reduced the regained permeability. So, the type of the surfactant used in the fracturing fluid can Significantly affect on the regained permeability. It should be noted that, the observed results are for the core plug with reported mineralogy in the text. Other rock samples may show different results using similar surfactant solutions. The effect of different surfactant types with different polarities should be investigated using flooding experiments as a screening step for choosing proper surfactant solutions for a specific rock type.
- The selected non-ionic surfactants showed higher surfactant adsorptions while they did not decrease the regained permeability. Surfactant adsorption for investigated surfactant solutions on the specific rock sample in this study showed that surfactant adsorption was not detrimental to the surfactant's functionality.
- The effect of IFT on regained permeability was not straightforward. The effect of IFT should be seen in conjunction with other aspects of the surfactants. For example, SS-6 reduced the IFT to 2.39 mN/m, much lower than the IFT of SS-2, but its regained permeability index was smaller since it changed the wettability toward the oil-wet state.

- The non-ionic surfactants (SS-3 and SS-4) and also the slightly anionic surfactant (SS-2) changed the wettability toward neutral-wet conditions. These surfactants exhibited minimum damage with maximum regained permeability index. It suggests that surfactants that change the wettability towards neutral-wet conditions have higher regained permeability index.
- Combining the effect of IFT and wettability in dimensionless parameter of N_{ca} shows that for $N_{ca} > 1.23\times10^{-8}$, the regained permeability index is equal to one, which means no damage to the permeability. Below that threshold, the smaller the N_{ca}, the smaller the regained permeability index, which means more damage to the permeability.
- In Test 1 with $S_{wi} = 0$, regain permeability dropped 22% compared to the initial permeability while in Test 2 with $S_{wi} = 0.3$, regained permeability dropped 14% compared to its initial value. We used tap water as the leak off fluid for the two tests. If a reservoir is at sub-irreducible water saturation conditions, the surfactant solutions may reduce the regain permeability because of an increase in water saturation inside the rock after leak-off and flowback processes. Therefore, when screening tests are done on a surfactant solution for a specific reservoir, the initial water saturation should be considered in the test design.

Bibliography

Abdulelah, Hesham, Syed M Mahmood, and Ahmed Al-Mutarreb. 2018. “Effect of Anionic Surfactant on Wettability of Shale and Its Implication on Gas Adsorption/Desorption Behavior.” *Energy & Fuels* 32 (2): 1423–32.

Ahmed, Usman, and D Nathan Meehan. 2016. *Unconventional Oil and Gas Resources: Exploitation and Development*. CRC Press.

Akai, Takashi, Qingyang Lin, Branko Bijeljic, and Martin J Blunt. 2020. “Using Energy Balance to Determine Pore-Scale Wettability.” *Journal of Colloid and Interface Science* 576: 486–95.

Akbarabadi, Morteza, Soheil Saraji, Mohammad Piri, Dan Georgi, and Mohammad Delshad. 2017. “Nano-Scale Experimental Investigation of in-Situ Wettability and Spontaneous Imbibition in Ultra-Tight Reservoir Rocks.” *Advances in Water Resources* 107: 160–79.

Alvarez, J O, and D S Schechter. 2016. “Altering Wettability in Bakken Shale by Surfactant Additives and Potential of Improving Oil Recovery during Injection of Completion Fluids.” In *SPE Improved Oil Recovery Conference*. OnePetro.

Alyafei, Nayef, and Martin J Blunt. 2018. “Estimation of Relative Permeability and Capillary Pressure from Mass Imbibition Experiments.” *Advances in Water Resources* 115: 88–94.

Amann-Hildenbrand, Alexandra, Pieter Bertier, Andreas Busch, and Bernhard M Krooss. 2013. “Experimental Investigation of the Sealing Capacity of Generic Clay-Rich Caprocks.” *International Journal of Greenhouse Gas Control* 19: 620–41.

Aslanidis, P, S Strand, T Puntervold, K K Yeboah, and I Souayeh. 2022. “Oil Recovery by Low-Rate Waterflooding in Low-Permeability Water-Wet Sandstone Cores.” *SPE Reservoir Evaluation & Engineering*, 1–13.

Azad, Madhar S, and Japan J Trivedi. 2020. “Does Polymer’s Viscoelasticity Influence Heavy-Oil Sweep Efficiency and Injectivity at 1 Ft/D?” *SPE Reservoir Evaluation & Engineering* 23 (02): 446–62.

Belhaj, Ahmed Fatih, Khaled Abdalla Elraies, Juhairi Aris Shuhili, Syed Mohammad Mahmood, Raj Deo Tewari, and Mohamad Sahban Alnarabiji. 2022. “Static Adsorption Evaluation for Anionic-Nonionic Surfactant Mixture on Sandstone in the Presence of Crude Oil at High Reservoir Temperature Condition.” *SPE Reservoir Evaluation & Engineering* 25 (02): 261–72.

Bennion, D B, F B Thomas, and R F Bietz. 1996. “Low Permeability Gas Reservoirs: Problems, Opportunities and Solutions for Drilling, Completion, Stimulation and Production.” In *SPE Gas Technology Symposium*. OnePetro.

Berg, Carl Fredrik, Per Arne Slotte, and Hamid Hosseinzade Khanamiri. 2020. “Geometrically Derived Efficiency of Slow Immiscible Displacement in Porous Media.” *Physical Review E* 102 (3): 33113.

Berne, Bruce J, and Robert Pecora. 2000. *Dynamic Light Scattering: With Applications to Chemistry, Biology, and Physics*. Courier Corporation.

Bertoncello, Antoine, Jon Wallace, Chris Blyton, M Honarpour, and C S Kabir. 2014. “Imbibition and Water Blockage in Unconventional Reservoirs: Well-Management Implications during Flowback and Early Production.” *SPE Reservoir Evaluation & Engineering* 17 (04): 497–506.

Bodaghia, M, P Goncalves, and N C Correia. 2014. “A Quantitative Evaluation of the Uncertainty of Permeability Measurements in Constant Thickness Fibre Reinforcements (RTM).” In *16th European Conference on Composite Materials*.

Boulin, P F, Pierre Bretonnier, Nicolas Gland, and Jean-Marc Lombard. 2012. “Contribution of the Steady State Method to Water Permeability Measurement in Very Low Permeability Porous Media.” *Oil & Gas Science and Technology–Revue d’IFP Energies Nouvelles* 67 (3): 387–401.

Brace, W_F, J B Walsh, and W T Frangos. 1968. “Permeability of Granite under High Pressure.” *Journal of Geophysical Research* 73 (6): 2225–36.

Brooks, Royal Harvard, and Arthur T Corey. 1966. “Properties of Porous Media Affecting Fluid Flow.” *Journal of the Irrigation and Drainage Division* 92 (2): 61–88.

Buckley, S.E., and M.C. Leverett. 1942. "Mechanism of Fluid Displacement in Sands." *Transactions of the AIME* 146 (01). https://doi.org/10.2118/942107-g.

Bui, Khoa, I Yucel Akkutlu, Andrei Zelenev, Hasnain Saboowala, John R Gillis, and James A Silas. 2016. "Insights into Mobilization of Shale Oil by Use of Microemulsion." *SPE Journal* 21 (02): 613–20.

Burdine, NeT. 1953. "Relative Permeability Calculations from Pore Size Distribution Data." *Journal of Petroleum Technology* 5 (03): 71–78.

Bustamante-Rendón, R A, E Pérez, and A Gama Goicochea. 2020. "Comparing the Efficiency of Pure and Mixed Cationic and Nonionic Surfactants Used in Enhanced Oil Recovery by Mesoscopic Simulations." *Fuel* 277: 118287.

Cao, Cheng, Tiantai Li, Juntai Shi, Lei Zhang, Shunxun Fu, Botao Wang, and Hui Wang. 2016. "A New Approach for Measuring the Permeability of Shale Featuring Adsorption and Ultra-Low Permeability." *Journal of Natural Gas Science and Engineering* 30: 548–56.

Castro Dantas, T N, P J Soares A, A O Wanderley Neto, A A Dantas Neto, and E L Barros Neto. 2014. "Implementing New Microemulsion Systems in Wettability Inversion and Oil Recovery from Carbonate Reservoirs." *Energy & Fuels* 28 (11): 6749–59.

Cha, Luming, Qihong Feng, Sen Wang, Shiqian Xu, and Chiyu Xie. 2022. "Pore-Scale Modeling of Immiscible Displacement In Porous Media: The Effects of Dual Wettability." *SPE Journal*, 1–12.

Chen, Xiongyu, Amir Kianinejad, and David A DiCarlo. 2016. "An Extended JBN Method of Determining Unsteady-state Two-phase Relative Permeability." *Water Resources Research* 52 (10): 8374–83.

Chen, Yufei, Changbao Jiang, Juliana Y Leung, Andrew K Wojtanowicz, Dongming Zhang, and Chuanyao Zhong. 2021. "Second-Order Correction of Klinkenberg Equation and Its Experimental Verification on Gas Shale with Respect to Anisotropic Stress." *Journal of Natural Gas Science and Engineering* 89: 103880.

Cheng, Kai Cong, Zhi Sheng Khoo, Newton Well Lo, Wei Jie Tan, and Nishanth G Chemmangattuvalappil. 2020. "Design and Performance Optimisation of Detergent Product

Containing Binary Mixture of Anionic-Nonionic Surfactants." *Heliyon* 6 (5): e03861.

Cornwell, P A. 2018. "A Review of Shampoo Surfactant Technology: Consumer Benefits, Raw Materials and Recent Developments." *International Journal of Cosmetic Science* 40 (1): 16–30.

Cui, Xiaojun, A M M Bustin, and Robert M Bustin. 2009. "Measurements of Gas Permeability and Diffusivity of Tight Reservoir Rocks: Different Approaches and Their Applications." *Geofluids* 9 (3): 208–23.

Cui, Xiaojun, and Brent Nassichuk. 2018. "Permeability of the Montney Formation in the Western Canada Sedimentary Basin: Insights from Different Laboratory Measurements." *Bulletin of Canadian Petroleum Geology* 66 (2): 394–424.

Darcy, Henry. 1856. *Les Fontaines Publiques de La Ville de Dijon: Exposition et Application Des Principes à Suivre et Des Formules à Employer Dans Les Questions de Distribution d'eau: Ouvrage Terminé Par Un Appendice Relatif Aux Fournitures d'eau de Plusieurs Villes, Au Filt*. Vol. 2. V. Dalmont.

Davies, Graham R, Thomas F Moslow, and Mike D Sherwin. 1997. "The Lower Triassic Montney Formation, West-Central Alberta." *Bulletin of Canadian Petroleum Geology* 45 (4): 474–505.

Day, Stuart, Robyn Fry, and Richard Sakurovs. 2012. "Swelling of Coal in Carbon Dioxide, Methane and Their Mixtures." *International Journal of Coal Geology* 93: 40–48.

Dejam, Morteza, Hassan Hassanzadeh, and Zhangxin Chen. 2017. "Pre-Darcy Flow in Porous Media." *Water Resources Research* 53 (10): 8187–8210.

Dicker, A I, and R M Smits. 1988. "A Practical Approach for Determining Permeability from Laboratory Pressure-Pulse Decay Measurements." In *International Meeting on Petroleum Engineering*. OnePetro.

Dong, Mingzhe, Zhaowen Li, Shuliang Li, and Jun Yao. 2012. "Permeabilities of Tight Reservoir Cores Determined for Gaseous and Liquid CO2 and C2H6 Using Minimum Backpressure Method." *Journal of Natural Gas Science and Engineering* 5: 1–5.

Doster, Florian, and R Hilfer. 2011. “Generalized Buckley–Leverett Theory for Two-Phase Flow in Porous Media.” *New Journal of Physics* 13 (12): 123030.

Eggertsson, G H, Y Lavallée, J E Kendrick, and S H Markússon. 2020. “Improving Fluid Flow in Geothermal Reservoirs by Thermal and Mechanical Stimulation: The Case of Krafla Volcano, Iceland.” *Journal of Volcanology and Geothermal Research* 391: 106351.

Eghbalvala, Maryam, Lin Yuan, Ali Habibi, and Hassan Dehghanpour. 2022. “A Laboratory Workflow to Screen Nanodroplet Additives for Enhanced Oil Recovery from Tight Rocks.” *Sustainable Energy Technologies and Assessments* 53: 102392.

El-Dieb, A S, and R D Hooton. 1995. “Water-Permeability Measurement of High Performance Concrete Using a High-Pressure Triaxial Cell.” *Cement and Concrete Research* 25 (6): 1199–1208.

Fassihi, Mohammad Reza, and Gary Frank Potter. 2009. “Analysis of Transient Data during Relative Permeability Measurements Using Steady-State Technique.” In *SPE Annual Technical Conference and Exhibition*. OnePetro.

Gbadamosi, Afeez O, Radzuan Junin, Muhammad A Manan, Augustine Agi, and Adeyinka S Yusuff. 2019. “An Overview of Chemical Enhanced Oil Recovery: Recent Advances and Prospects.” *International Nano Letters* 9 (3): 171–202.

Gensterblum, Yves, Amin Ghanizadeh, Robert J Cuss, Alexandra Amann-Hildenbrand, Bernhard M Krooss, Christopher R Clarkson, John F Harrington, and Mark D Zoback. 2015. “Gas Transport and Storage Capacity in Shale Gas Reservoirs–A Review. Part A: Transport Processes.” *Journal of Unconventional Oil and Gas Resources* 12: 87–122.

Goda, H M, and P Behrenbruch. 2004. “Using a Modified Brooks-Corey Model to Study Oil-Water Relative Permeability for Diverse Pore Structures.” In *SPE Asia Pacific Oil and Gas Conference and Exhibition*. OnePetro.

Green, Don W, and G Paul Willhite. 1998. “Enhanced Oil Recovery: Richardson, Tex.: Henry L. Doherty Memorial Fund of AIME.” *Society of Petroleum Engineers*, 42–51.

Guler, B, T Ertekin, and A S Grader. 2003. “An Artificial Neural Network Based Relative Permeability Predictor.” *Journal of Canadian Petroleum Technology* 42 (04).

Habibi, Ali, Yussef Esparza, Yaman Boluk, and Hassan Dehghanpour. 2020. “Enhancing Imbibition Oil Recovery from Tight Rocks by Mixing Nonionic Surfactants.” *Energy & Fuels* 34 (10): 12301–13.

Habibi, Ali, Mahmood Reza Yassin, Hassan Dehghanpour, and Donald Bryan. 2017. “Experimental Investigation of CO2-Oil Interactions in Tight Rocks: A Montney Case Study.” *Fuel* 203: 853–67.

Haskett, Steven E, Gene M Narahara, and Stephen A Holditch. 1988. “A Method for Simultaneous Determination of Permeability and Porosity in Low-Permeability Cores.” *SPE Formation Evaluation* 3 (03): 651–58.

Hassanzadeh, Hassan, and Mehran Pooladi-Darvish. 2007. “Comparison of Different Numerical Laplace Inversion Methods for Engineering Applications.” *Applied Mathematics and Computation* 189 (2): 1966–81.

He, Kai, and Liang Xu. 2018. “Unique Mixtures of Anionic/Cationic Surfactants: A New Approach to Enhance Surfactant Performance in Liquids-Rich Shale Reservoirs.” *SPE Production & Operations* 33 (02): 363–70.

Hill, S. 1952. “Channeling in Packed Columns.” *Chemical Engineering Science* 1 (6): 247–53.

Honarpour, M., Koederitz, L., & Harvey, A. H. 2018. *Relative Permeability of Petroleum Reservoirs*. CRC press.

Hornof, V, and N R Morrow. 1988. “Flow Visualization of the Effects of Interfacial Tension on Displacement.” *SPE Reservoir Engineering* 3 (01): 251–56.

Hsieh, P A, J V Tracy, C E Neuzil, J D Bredehoeft, and Stephen E Silliman. 1981. “A Transient Laboratory Method for Determining the Hydraulic Properties of ‘Tight’Rocks—I. Theory.” In *International Journal of Rock Mechanics and Mining Sciences & Geomechanics Abstracts*, 18:245–52. Elsevier.

Johnson, E F, D P Bossler, and V O Bossler. 1959. “Calculation of Relative Permeability from Displacement Experiments.” *Transactions of the AIME* 216 (01): 370–72.

Jones, Colin, and P Meredith. 1998. “An Experimental Study of Elastic Wave Propagation an

Isotropy and Permeability an Isotropy In an Illitic Shale." In *SPE/ISRM Rock Mechanics in Petroleum Engineering*. OnePetro.

Jones, S C. 1997. "A Technique for Faster Pulse-Decay Permeability Measurements in Tight Rocks." *SPE Formation Evaluation* 12 (01): 19–25.

Jones, S C, and W O Roszelle. 1978. "Graphical Techniques for Determining Relative Permeability from Displacement Experiments." *Journal of Petroleum Technology* 30 (05): 807–17.

Kalaydjian, FJ-M. 1992. "Dynamic Capillary Pressure Curve for Water/Oil Displacement in Porous Media: Theory vs. Experiment." In *SPE Annual Technical Conference and Exhibition*. OnePetro.

Kamal, Muhammad Shahzad, Ibnelwaleed A Hussein, and Abdullah S Sultan. 2017. "Review on Surfactant Flooding: Phase Behavior, Retention, IFT, and Field Applications." *Energy & Fuels* 31 (8): 7701–20.

Kathel, P, and K K Mohanty. 2013. "Wettability Alteration in a Tight Oil Reservoir." *Energy & Fuels* 27 (11): 6460–68.

Khan, Mudeha Shafat, Adil Amin Wani, Tabasum Ismail, Sajad Ahmad Bhat, Feroz Ahmad Sofi, and Mohsin Ahmad Bhat. 2020. "Eureka Moment: An Archimedean Alternative for the Determination of Cmc of Surfactants via Weight Measurements." *ACS Omega* 5 (49): 31640–43.

Khanamiri, Hamid Hosseinzade, Carl Fredrik Berg, Per Arne Slotte, Steffen Schlüter, and Ole Torsæter. 2018. "Description of Free Energy for Immiscible Two-fluid Flow in Porous Media by Integral Geometry and Thermodynamics." *Water Resources Research* 54 (11): 9045–59.

Khorsandi, Saeid, Liwei Li, and Russell T Johns. 2017. "Equation of State for Relative Permeability, Including Hysteresis and Wettability Alteration." *SPE Journal* 22 (06): 1915–28.

Klinkenberg, L J. 1941. "The Permeability of Porous Media to Liquids and Gases." *Am. Petrol. Inst., Drilling and Production Practice* 2: 200–213.

Kueper, Bernard H, and Emil O Frind. 1988. "An Overview of Immiscible Fingering in Porous Media." *Journal of Contaminant Hydrology* 2 (2): 95–110.

Kumar, Sunil, Priyanka Panigrahi, Rohit Kumar Saw, and Ajay Mandal. 2016. "Interfacial Interaction of Cationic Surfactants and Its Effect on Wettability Alteration of Oil-Wet Carbonate Rock." *Energy & Fuels* 30 (4): 2846–57.

Lake, Larry W. 1989. "Enhanced Oil Recovery."

Lan, Yuzheng, Davud Davudov, and Rouzbeh Ghanbarnezhad Moghanloo. 2017. "Interplay between Permeability and Compressibility in Shale Samples." *Journal of Petroleum Science and Engineering* 159: 644–53.

Lasswell, Pat. 2013. "Steady-State Permeability Analysis in Unconventional Plays." *Geoconvention 2013: Integration*, 1–10.

Lei, Gang, Pingchuan Dong, Zishen Wu, Shaoyuan Mo, Shaohua Gai, Chao Zhao, and Z K Liu. 2015. "A Fractal Model for the Stress-Dependent Permeability and Relative Permeability in Tight Sandstones." *Journal of Canadian Petroleum Technology* 54 (01): 36–48.

Li, Kewen, and Roland N. Horne. 2006. "Comparison of Methods to Calculate Relative Permeability from Capillary Pressure in Consolidated Water-Wet Porous Media." *Water Resources Research* 42 (6). https://doi.org/10.1029/2005WR004482.

Li, Yi, and Qingchun Yu. 2020. "Rock-Core Scale Modeling of Initial Water Saturation Effects on CO2 Breakthrough Pressure in CO2 Geo-Sequestration." *Journal of Hydrology* 580: 124234.

Liang, Tianbo, Rafael A Longoria, Jun Lu, Quoc P Nguyen, and David A DiCarlo. 2017. "Enhancing Hydrocarbon Permeability after Hydraulic Fracturing: Laboratory Evaluations of Shut-Ins and Surfactant Additives." *Spe Journal* 22 (04): 1011–23.

Lin, Qingyang, Branko Bijeljic, Ronny Pini, Martin J Blunt, and Samuel Krevor. 2018. "Imaging and Measurement of Pore-scale Interfacial Curvature to Determine Capillary Pressure Simultaneously with Relative Permeability." *Water Resources Research* 54 (9): 7046–60.

Lin, W. 1977. "Compressible Fluid Flow through Rocks of Variable Permeability." California

Univ., Livermore (USA). Lawrence Livermore Lab.

Liu, Haihu, Albert J Valocchi, and Qinjun Kang. 2012. "Three-Dimensional Lattice Boltzmann Model for Immiscible Two-Phase Flow Simulations." *Physical Review E* 85 (4): 46309.

Longoria, Rafael A, Tianbo Liang, Uyen T Huynh, Quoc P Nguyen, and David A DiCarlo. 2017. "Water Blocks in Tight Formations: The Role of Matrix/Fracture Interaction in Hydrocarbon-Permeability Reduction and Its Implications in the Use of Enhanced Oil Recovery Techniques." *SPE Journal* 22 (05): 1393–1401.

Lunowa, Stephan B., Carina Bringedal, and Iuliu Sorin Pop. 2021. "On an Averaged Model for Immiscible Two-Phase Flow with Surface Tension and Dynamic Contact Angle in a Thin Strip." *Studies in Applied Mathematics* 147 (1): 84–126. https://doi.org/10.1111/sapm.12376.

Lyu, Qiao, Jindong Shi, and Ranjith Pathegama Gamage. 2020. "Effects of Testing Method, Lithology and Fluid-Rock Interactions on Shale Permeability: A Review of Laboratory Measurements." *Journal of Natural Gas Science and Engineering* 78: 103302.

Ma, S M, X Zhang, N R Morrow, and X Zhou. 1999. "Characterization of Wettability from Spontaneous Imbibition Measurements." *Journal of Canadian Petroleum Technology* 38 (13).

Massarweh, Osama, and Ahmad S Abushaikha. 2020. "The Use of Surfactants in Enhanced Oil Recovery: A Review of Recent Advances." *Energy Reports* 6: 3150–78.

McKee, Chester R, Amar C Bumb, and Robert A Koenig. 1988. "Stress-Dependent Permeability and Porosity of Coal and Other Geologic Formations." *SPE Formation Evaluation* 3 (01): 81–91.

McPhee, Colin, Jules Reed, and Izaskun Zubizarreta. 2015. *Core Analysis: A Best Practice Guide*. Elsevier.

Metwally, Yasser M, and Carl H Sondergeld. 2011. "Measuring Low Permeabilities of Gas-Sands and Shales Using a Pressure Transmission Technique." *International Journal of Rock Mechanics and Mining Sciences* 48 (7): 1135–44.

Mirchi, Vahideh, Soheil Saraji, Lamia Goual, and Mohammad Piri. 2015. “Dynamic Interfacial Tension and Wettability of Shale in the Presence of Surfactants at Reservoir Conditions.” *Fuel* 148: 127–38.

Morrow, C A, and D A Lockner. 1997. “Permeability and Porosity of the Illinois UPH 3 Drillhole Granite and a Comparison with Other Deep Drillhole Rocks.” *Journal of Geophysical Research: Solid Earth* 102 (B2): 3067–75.

Nalley, Stephen, and Angelina LaRose. 2022. “Annual Energy Outlook 2022 (AEO2022).” *Energy Information Agency*, 23.

Nguyen, Duy, Dongmei Wang, Aderaje Oladapo, Jin Zhang, Jeffrey Sickorez, Ray Butler, and Brian Mueller. 2014. “Evaluation of Surfactants for Oil Recovery Potential in Shale Reservoirs.” In *SPE Improved Oil Recovery Symposium*. OnePetro.

Noël, Timothy, Yiran Cao, and Gabriele Laudadio. 2019. “The Fundamentals behind the Use of Flow Reactors in Electrochemistry.” *Accounts of Chemical Research* 52 (10): 2858–69.

Odeh, A S, and D K Babu. 1988. “Comparison of Solutions of the Nonlinear and Linearized Diffusion Equations.” *SPE Reservoir Engineering* 3 (04): 1202–6.

Ojha, Shiv Prakash, Siddharth Misra, Ali Tinni, Carl Sondergeld, and Chandra Rai. 2017. “Relative Permeability Estimates for Wolfcamp and Eagle Ford Shale Samples from Oil, Gas and Condensate Windows Using Adsorption-Desorption Measurements.” *Fuel* 208: 52–64.

Olayiwola, Saheed Olawale, and Morteza Dejam. 2019. “A Comprehensive Review on Interaction of Nanoparticles with Low Salinity Water and Surfactant for Enhanced Oil Recovery in Sandstone and Carbonate Reservoirs.” *Fuel* 241: 1045–57.

Park, Kang Han, and David S Schechter. 2020. “Investigation of the Interaction of Surfactant at Variable Salinity with Permian Basin Rock Samples: Completion Enhancement and Application for Enhanced Oil Recovery.” *SPE Drilling & Completion* 35 (01): 100–113.

Pasquier, Sylvain, Michel Quintard, and Yohan Davit. 2017. “Modeling Two-Phase Flow of Immiscible Fluids in Porous Media: Buckley-Leverett Theory with Explicit Coupling Terms.” *Physical Review Fluids* 2 (10). https://doi.org/10.1103/PhysRevFluids.2.104101.

Peng, Sheng. 2019. “Gas Relative Permeability and Its Evolution during Water Imbibition in Unconventional Reservoir Rocks: Direct Laboratory Measurement and a Conceptual Model.” *SPE Reservoir Evaluation & Engineering* 22 (04): 1346–59.

———. 2020. “Gas-Water Relative Permeability of Unconventional Reservoir Rocks: Hysteresis and Influence on Production after Shut-In.” *Journal of Natural Gas Science and Engineering* 82: 103511.

Peters, Ekwere J. 2006. “Petrophysics.” *Department of Petroleum and Geosystems Engineering, University of Texas at Austin*.

Pini, Ronny, and Sally M Benson. 2013. “Simultaneous Determination of Capillary Pressure and Relative Permeability Curves from Core-flooding Experiments with Various Fluid Pairs.” *Water Resources Research* 49 (6): 3516–30.

Purcell, W R. 1949. “Capillary Pressures-Their Measurement Using Mercury and the Calculation of Permeability Therefrom.” *Journal of Petroleum Technology* 1 (02): 39–48.

Reynolds, M M, R C Bachman, and W E Peters. 2014. “A Comparison of the Effectiveness of Various Fracture Fluid Systems Used in Multi-Stage Fractured Horizontal Wells: Montney Formation, Unconventional Gas.” In *SPE Hydraulic Fracturing Technology Conference*. OnePetro.

Rouquerol, J, D Avnir, C W Fairbridge, D H Everett, J M Haynes, N Pernicone, J D F Ramsay, K S W Sing, and K K Unger. 1994. “Recommendations for the Characterization of Porous Solids (Technical Report).” *Pure and Applied Chemistry* 66 (8): 1739–58.

Rushing, J A, K E Newsham, P M Lasswell, J C Cox, and T A Blasingame. 2004. “Klinkenerg-Corrected Permeability Measurements in Tight Gas Sands: Steady-State versus Unsteady-State Techniques.” In *SPE Annual Technical Conference and Exhibition*. OnePetro.

Sander, Regina, Zhejun Pan, and Luke D Connell. 2017. “Laboratory Measurement of Low Permeability Unconventional Gas Reservoir Rocks: A Review of Experimental Methods.” *Journal of Natural Gas Science and Engineering* 37: 248–79.

Saxena, Neha, Amit Kumar, and Ajay Mandal. 2019. “Adsorption Analysis of Natural Anionic Surfactant for Enhanced Oil Recovery: The Role of Mineralogy, Salinity, Alkalinity and

Nanoparticles." *Journal of Petroleum Science and Engineering* 173: 1264–83.

Scheer, Dirk, Holger Class, and Bernd Flemisch. 2021. "Nuclear Energy and Waste Disposal." In *Subsurface Environmental Modelling Between Science and Policy*, 179–92. Springer.

Schembre-McCabe, Josephina, Jairam Kamath, Andrew Fager, and Bernd Crouse. 2020. "Estimation of Gas-Condensate Relative Permeability Using a Lattice Boltzmann Modeling Approach." *Petrophysics-The SPWLA Journal of Formation Evaluation and Reservoir Description* 61 (02): 206–16.

Schmid, Karen S, Nayef Alyafei, Sebastian Geiger, and Martin J Blunt. 2016. "Analytical Solutions for Spontaneous Imbibition: Fractional-Flow Theory and Experimental Analysis." *SPE Journal* 21 (06): 2308–16.

Sheng, James J. 2015. "Status of Surfactant EOR Technology." *Petroleum* 1 (2): 97–105.

Sinha, S, E M Braun, M D Determan, Q R Passey, S A Leonardi, J A Boros, A C Wood, T Zirkle, and R A Kudva. 2013. "Steady-State Permeability Measurements on Intact Shale Samples at Reservoir Conditions-Effect of Stress, Temperature, Pressure, and Type of Gas." In *SPE Middle East Oil and Gas Show and Conference*. OnePetro.

Sorbie, KS. 2013. *Polymer-Improved Oil Recovery*. Springer Science & Business Media.

Spivey, John P, and W John Lee. 2013. "Applied Well Test Interpretation."

Standnes, Dag Chun, Steinar Evje, and Pål Østebø Andersen. 2017. "A Novel Relative Permeability Model Based on Mixture Theory Approach Accounting for Solid–Fluid and Fluid–Fluid Interactions." *Transport in Porous Media* 119 (3): 707–38.

Stehfest, Harald. 1970. "Numerical Inversion of Laplace Transforms Algorithm 368." *Commun. ACM* 13 (1): 47–49.

Su, Yu-Liang, Ji-Long Xu, Wen-Dong Wang, Han Wang, and Shi-Yuan Zhan. 2022. "Relative Permeability Estimation of Oil− Water Two-Phase Flow in Shale Reservoir." *Petroleum Science* 19 (3): 1153–64.

Suwandi, Natanael, Fei Jiang, and Takeshi Tsuji. 2022. "Relative Permeability Variation Depending on Viscosity Ratio and Capillary Number." *Water Resources Research* 58 (6):

e2021WR031501.

Tangirala, Srikanth, and James J Sheng. 2019. “Roles of Surfactants during Soaking and Post Leak-off Production Stages of Hydraulic Fracturing Operation in Tight Oil-Wet Rocks.” *Energy & Fuels* 33 (9): 8363–73.

Tecklenburg, Jan, Insa Neuweiler, Marco Dentz, Jesus Carrera, Sebastian Geiger, Christian Abramowski, and Orlando Silva. 2013. “A Non-Local Two-Phase Flow Model for Immiscible Displacement in Highly Heterogeneous Porous Media and Its Parametrization.” *Advances in Water Resources* 62: 475–87.

Tinni, Ali, Ebrahim Fathi, Rajiv Agarwal, Carl Sondergeld, Yucel Akkutlu, and Chandra Rai. 2012. “Shale Permeability Measurements on Plugs and Crushed Samples.” In *SPE Canadian Unconventional Resources Conference*. OnePetro.

Valavanides, Marios S, Nikolaos Karadimitriou, and Holger Steeb. 2022. “Flow Dependent Relative Permeability Scaling for Steady-State Two-Phase Flow in Porous Media: Laboratory Validation on a Microfluidic Network.” In *SPWLA 63rd Annual Logging Symposium*. OnePetro.

Vonnegut, Bernard. 1942. “Rotating Bubble Method for the Determination of Surface and Interfacial Tensions.” *Review of Scientific Instruments* 13 (1): 6–9.

Walls, Joel D, Amos M Nur, and Thierry Bourbie. 1982. “Effects of Pressure and Partial Water Saturation on Gas Permeability in Tight Sands: Experimental Results.” *Journal of Petroleum Technology* 34 (04): 930–36.

Wang, Dongmei, Ray Butler, Jin Zhang, and Randy Seright. 2012. “Wettability Survey in Bakken Shale with Surfactant-Formulation Imbibition.” *SPE Reservoir Evaluation & Engineering* 15 (06): 695–705.

Wang, G X, X R Wei, K Wang, P Massarotto, and V Rudolph. 2010. “Sorption-Induced Swelling/Shrinkage and Permeability of Coal under Stressed Adsorption/Desorption Conditions.” *International Journal of Coal Geology* 83 (1): 46–54.

Wang, Kai, Feng Du, and Gongda Wang. 2017. “Investigation of Gas Pressure and Temperature Effects on the Permeability and Steady-State Time of Chinese Anthracite Coal: An

Experimental Study." *Journal of Natural Gas Science and Engineering* 40: 179–88.

Wasaki, Asana, and I Yucel Akkutlu. 2015. "Permeability of Organic-Rich Shale." *Spe Journal* 20 (06): 1384–96.

Welge, Henry J. 1952. "A Simplified Method for Computing Oil Recovery by Gas or Water Drive." *Journal of Petroleum Technology* 4 (04): 91–98.

Winhausen, Lisa, Alexandra Amann-Hildenbrand, Reinhard Fink, Mohammadreza Jalali, Kavan Khaledi, Pooya Hamdi, Janos L Urai, Joyce Schmatz, and Florian Amann. 2021. "A Comparative Study on Methods for Determining the Hydraulic Properties of a Clay Shale." *Geophysical Journal International* 224 (3): 1523–39.

Xia, Yan, Juan-Juan Zhou, Yan-Yan Gong, Zhan-Jun Li, and Eddy Y Zeng. 2020. "Strong Influence of Surfactants on Virgin Hydrophobic Microplastics Adsorbing Ionic Organic Pollutants." *Environmental Pollution* 265: 115061.

Xiao, Ting, Hao Xu, Nathan Moodie, Richard Esser, Wei Jia, Liange Zheng, Jonny Rutqvist, and Brian McPherson. 2020. "Chemical-mechanical Impacts of CO2 Intrusion into Heterogeneous Caprock." *Water Resources Research* 56 (11): e2020WR027193.

Xu, Guang, Yinping Chen, Jacques Eksteen, and Jialin Xu. 2018. "Surfactant-Aided Coal Dust Suppression: A Review of Evaluation Methods and Influencing Factors." *Science of the Total Environment* 639: 1060–76.

Yarveicy, Hamidreza, Ali Habibi, Serge Pegov, Ashkan Zolfaghari, and Hassan Dehghanpour. 2018. "Enhancing Oil Recovery by Adding Surfactants in Fracturing Water: A Montney Case Study." In *SPE Canada Unconventional Resources Conference*. OnePetro.

Yassin, Mahmood Reza, Hassan Dehghanpour, James Wood, and Qing Lan. 2016. "A Theory for Relative Permeability of Unconventional Rocks with Dual-Wettability Pore Network." *Spe Journal* 21 (06): 1970–80.

Yeganeh, Mohsen, Jessica Hegner, Eric Lewandowski, Aruna Mohan, Larry W Lake, Dan Cherney, Arben Jusufi, and Aditya Jaishankar. 2016. "Capillary Desaturation Curve Fundamentals." In *SPE Improved Oil Recovery Conference*. OnePetro.

Yekeen, Nurudeen, Eswaran Padmanabhan, Ahmad Kamal Idris, and Syed Muhammad Ibad. 2019. “Surfactant Adsorption Behaviors onto Shale from Malaysian Formations: Influence of Silicon Dioxide Nanoparticles, Surfactant Type, Temperature, Salinity and Shale Lithology.” *Journal of Petroleum Science and Engineering* 179: 841–54.

Yousefi, M., A. Habibi, and H. Dehghanpour. 2020. “Surfactant in Fracturing Fluid: Enhancing Imbibition Oil Recovery or Blocking Pore Throats?” In *Proceedings - SPE Symposium on Improved Oil Recovery*. https://doi.org/10.2118/200470-MS.

Yousefi, Mohammad, and Hassan Dehghanpour. 2022. “A Model and Measurement Technique for Liquid Permeability of Tight Porous Media Based on the Steady-State Method.” *Energy & Fuels*.

Yuan, Lin, Ali Habibi, and Hassan Dehghanpour. 2021. “Liquid Imbibition in Tight Rocks: The Role of Disjoining Pressure.” *Colloids and Surfaces A: Physicochemical and Engineering Aspects* 627: 127037.

Yucel Akkutlu, I, and Ebrahim Fathi. 2012. “Multiscale Gas Transport in Shales with Local Kerogen Heterogeneities.” *SPE Journal* 17 (04): 1002–11.

Zargartalebi, Mohammad, Nasim Barati, and Riyaz Kharrat. 2014. “Influences of Hydrophilic and Hydrophobic Silica Nanoparticles on Anionic Surfactant Properties: Interfacial and Adsorption Behaviors.” *Journal of Petroleum Science and Engineering* 119: 36–43.

Zeng, Tongzhou, Kyung Tae Kim, Charles J Werth, Lynn E Katz, and Kishore K Mohanty. 2020. “Surfactant Adsorption on Shale Samples: Experiments and an Additive Model.” *Energy & Fuels* 34 (5): 5436–43.

Zhang, Tao, Xiangfang Li, Zheng Sun, Dong Feng, Yanan Miao, Peihuan Li, and Zenghua Zhang. 2017. “An Analytical Model for Relative Permeability in Water-Wet Nanoporous Media.” *Chemical Engineering Science* 174: 1–12.

Zivar, Davood, Sunil Kumar, and Jalal Foroozesh. 2021. “Underground Hydrogen Storage: A Comprehensive Review.” *International Journal of Hydrogen Energy* 46 (45): 23436–62.

Appendix A
Derivation of General Diffusivity Equation with Pseudo-Compressibility Term

Consider linear flow of a slightly compressible flow through a porous medium. The continuity equation can be written as:

$$\frac{\partial}{\partial t}(\rho\varphi) = -\frac{\partial}{\partial x}(\rho v) \ldots\ldots \text{(A-1)}$$

Where φ is the porosity of the medium, ρ is the density of the fluid, and v is the fluid velocity.

For a slightly compressible fluid, we assume compressibility is constant with pressure and can be written as:

$$c = \frac{1}{\rho}\frac{\partial \rho}{\partial p} \ldots\ldots \text{(A-2)}$$

The rock compressibility can also be written as :

$$c_r = \frac{1}{\varphi}\frac{\partial \varphi}{\partial p} \ldots\ldots \text{(A-3)}$$

For the fluid velocity we can use Darcy equation:

$$v = -\frac{k}{\mu}\frac{\partial p}{\partial x} \ldots\ldots \text{(A-4)}$$

Substitute Eq. A-4 into Eq. A-1:

$$\frac{\partial}{\partial t}(\rho\varphi) = \frac{\partial}{\partial x}\left(\rho\frac{k}{\mu}\frac{\partial p}{\partial x}\right) \ldots\ldots \text{(A-5)}$$

Applying chain rule with the assumption of constant viscosity (μ) will result in:

$$\varphi\frac{\partial \rho}{\partial t} + \rho\frac{\partial \varphi}{\partial t} = \frac{\rho k}{\mu}\frac{\partial^2 p}{\partial x^2} + \frac{1}{\mu}\frac{\partial p}{\partial x}\left(\rho\frac{\partial k}{\partial x} + k\frac{\partial \rho}{\partial x}\right) \ldots\ldots \text{(A-6)}$$

Combining Eq. A-2, Eq. A-3, and Eq. A-6 we will get:

$$\frac{\partial^2 p}{\partial x^2} + c\left(\frac{\partial p}{\partial x}\right)^2 + \frac{1}{k}\left(\frac{\partial k}{\partial x}\right)\left(\frac{\partial p}{\partial x}\right) = \frac{\mu\varphi(c+c_r)}{k}\left(\frac{\partial p}{\partial t}\right) \ldots\ldots \text{(A-7)}$$

Applying chain rule for the term $\frac{1}{k}\left(\frac{\partial k}{\partial x}\right)\left(\frac{\partial p}{\partial x}\right)$ we have:

$$\frac{1}{k}\left(\frac{\partial k}{\partial x}\right)\left(\frac{\partial p}{\partial x}\right) = \frac{1}{k}\left(\frac{\partial k}{\partial p}\right)\left(\frac{\partial p}{\partial x}\right)\left(\frac{\partial p}{\partial x}\right) = \frac{1}{k}\left(\frac{\partial k}{\partial p}\right)\left(\frac{\partial p}{\partial x}\right)^2 \ldots\ldots \text{(A-8)}$$

Combining Eq. A-7 and Eq. A-8 we have:

$$\frac{\partial^2 p}{\partial x^2} + \acute{c}\left(\frac{\partial p}{\partial x}\right)^2 = \frac{\mu\varphi(c+c_r)}{k}\left(\frac{\partial p}{\partial t}\right) \ldots\ldots \text{(A-9)}$$

Where $\acute{c} = c + \frac{1}{k}\left(\frac{\partial k}{\partial p}\right)$

Appendix B
Solution of General Diffusivity Equation with Conventional Boundary Conditions

Figure B-1 shows a schematic of a plug with initial and boundary conditions to be modeled for 1-D flow. Since this equation is going to be solved after several rate changes and after each rate change we have to wait for the stabilization, we consider steady state flow is stablished along the plug as initial condition which creates a logarithmic pressure profile along the rock sample (as will be explained in appendix C). A constant flowrate of q is injected into the plug from the face at x = L. The outlet face, which is at x = 0, has atmospheric pressure. **Eq. B-1** is solved with stated initial and boundary conditions.

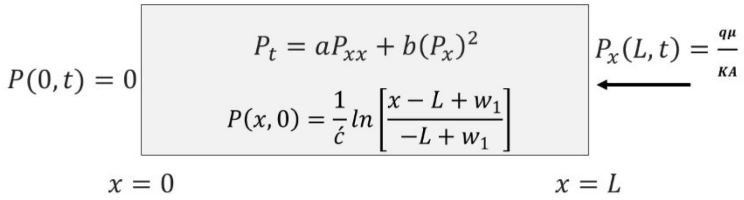

Figure B-1: One-dimensional model of diffusivity equation with initial and boundary conditions.

$\mathrm{P_t = aP_{xx} + b(P_x)^2}$……………………………………………………………………....(B-1)

Here, $\mathrm{a = \frac{k}{\mu c\emptyset}}$, $\mathrm{b = \frac{kc}{\mu c\emptyset}}$

To simplify the equation, we substitute $\mathrm{P(x,t) = \frac{a}{b} ln\ |H(x,t)|}$.

Then:

$\mathrm{H_t = aH_{xx}}$………………………………………………….…………………………….…(B-2)

The initial and boundary conditions change as:

I.C.: $\mathrm{H(x,0) = \frac{x-L+w_1}{-L+w_1}}$ where $\mathrm{w_1 = \frac{kA}{q_i\mu c}}$, here, $\mathrm{q_i}$ is the flowrate at which initial steady state was stablished.

B.C.1: $\mathrm{H(0,t) = 1}$

B.C.2: $\mathrm{H_x|_{x=L} = w_2H|_{x=L}}$

Where $w_2 = \frac{q\mu c}{KA}$

Then we substitute $U(x,t) = H(x,t) - \frac{x-L+w_1}{-L+w_1}$ to simplify initial and boundary condition 1.

$U_t = aU_{xx}$……………………………………………………………………………….…….(B-3)

I.C.: $U(x,0) = 0$

B.C.1: $U(0,t) = 0$

B.C.2: $U_x|_{x=L} = w_2 U|_{x=L} + w_4$

Where $w_4 = \frac{w_1 w_2 - 1}{-L+w_1}$

Now, we take Laplace from Eq. B-3 and its initial and boundary conditions.

$\widetilde{U}_{xx} - \frac{S}{a}\widetilde{U} = 0$……………………………………………...……………………………….…(B-4)

I.C.: $\widetilde{U}(x,0) = 0$

B.C.1: $\widetilde{U}(0,S) = 0$

B.C.2: $\widetilde{U}_x|_{x=L} = w_2 \widetilde{U}|_{x=L} + \frac{w_4}{S}$

The general solution of ordinary differential equation of Eq. B-4 is in the form of:

$\widetilde{U}(x,S) = Ae^{\sqrt{\frac{S}{a}}x} + Be^{-\sqrt{\frac{S}{a}}x}$ ……………………………………………...………………….....(B-5)

Applying initial or first boundary condition we will get:

$A = -B$

Applying second boundary condition we will get:

$A = \frac{w_4}{2S\sqrt{\frac{S}{a}}\cosh\left(\sqrt{\frac{S}{a}}L\right) - 2Sw_2\sinh\left(\sqrt{\frac{S}{a}}L\right)}$……………………………………...………..…(B-6)

Thus, the final form of solution of Eq. B-4 in Laplace domain is:

$\mathbf{\widetilde{U}(x,S)} = \frac{\mathbf{w_4 \sinh\left(\sqrt{\frac{S}{a}}x\right)}}{\mathbf{S\sqrt{\frac{S}{a}}\cosh\left(\sqrt{\frac{S}{a}}L\right) - Sw_2 \sinh\left(\sqrt{\frac{S}{a}}L\right)}}$………………………………………………...………(B-7)

Since this equation is complicated for analytical Laplace inverse, we use Stehfest's method (Stehfest 1970) to find Laplace inversion numerically. The method is explained in the work of Hassanzadeh and Pooladi-Darvish (2007).

Appendix C
Derivation of Logarithmic Initial Condition of General Diffusivity Equation

If we have a fully developed steady state flow as initial condition for Eq. 1, the P_t term in diffusivity equation is zero. Thus:

$aP_{xx} + b(P_x)^2 = 0$……………………………………………………………………….…(C-1)

Where $a = \frac{k}{\mu c \emptyset}$, $= \frac{k\acute{c}}{\mu c \emptyset}$, and $\acute{c} = c + \frac{1}{k}\left(\frac{\partial k}{\partial P}\right)$

Simplifying the Eq. C-1 we get:

$$P_{xx} = -\acute{c}(P_x)^2$$

Then substitute $z = P_x$:

$$z_x = -\acute{c}z^2$$

Solving this first order differential equation, we get:

$z = \frac{1}{\acute{c}x + C_1}$……………………………………………………………………………...(C-2)

At steady state condition the influx flowrate q_i is constant. We use Darcy equation to find constant C_1.

@ $x = L$ we have $z = P_x = \frac{q_i \mu}{kA}$. Thus:

$$C_1 = \frac{kA}{q_i \mu} - \acute{c}L$$

Substitute it in Eq. C-2 we get:

$$P_x = \frac{1}{\acute{c}(x - L) + \frac{kA}{q_i \mu}}$$

The solution of this differential equation is:

$P = \frac{1}{\acute{c}} \ln\left[\acute{c}(x - L) + \frac{kA}{q_i \mu}\right] + C_2$……………………………………………………………(C-3)

@ $x = 0$ which is outlet boundary condition we have $P(0, t) = 0$. Thus:

$C_2 = -\frac{1}{\acute{c}} \ln\left[-\acute{c}L + \frac{kA}{q_i \mu}\right]$ ………………………………………………………………...(C-4)

Substituting C_2 into Eq. C-3, we get initial condition when a steady state flow is fully developed along the rock sample:

$$P(x,0) = \frac{1}{\acute{c}} \ln\left[\frac{\acute{c}(x-L)+\frac{kA}{q_i\mu}}{-\acute{c}L+\frac{kA}{q_i\mu}}\right] \text{…….(C-5)}$$

If we substitute $w_1 = \frac{kA}{q_i\mu\acute{c}}$:

$$\mathbf{P(x,0)} = \frac{\mathbf{1}}{\acute{\mathbf{c}}} \mathbf{ln}\left[\frac{\mathbf{x-L+w_1}}{\mathbf{-L+w_1}}\right] \text{…....(C-6)}$$

Appendix D
Solution of General Diffusivity Equation with Modified Initial and Boundary Conditions

Figure D-1 shows a schematic of plug with initial and boundary conditions to be modeled for 1-D flow. Initially, steady state flow is stablished along the plug which creates a logarithmic pressure profile along the rock sample (as explained in appendix C). A time-dependent flowrate is injected into the plug from the face at x = L. The outlet face, which is at x = 0, has atmospheric pressure. Eq. D-1 is solved with stated initial and modified boundary conditions.

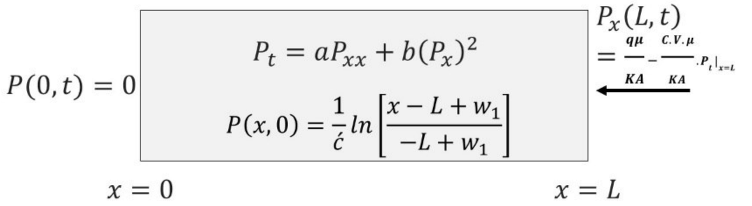

Figure D-1: One-dimensional model of diffusivity equation with modified boundary and initial conditions.

$\mathrm{P_t = aP_{xx} + b(P_x)^2}$ ……………………………………………………………………....(D-1)

Here, $\mathrm{a} = \frac{\mathrm{k}}{\mathrm{\mu c\emptyset}}$, $= \frac{\mathrm{k\acute{c}}}{\mathrm{\mu c\emptyset}}$, and $\mathrm{\acute{c} = c} + \frac{1}{\mathrm{k}}\left(\frac{\partial \mathrm{k}}{\partial \mathrm{P}}\right)$

To simplify the equation, we substitute $\mathrm{P(x,t)} = \frac{\mathrm{a}}{\mathrm{b}} \ln\ |\mathrm{H(x,t)}|$.

Then:

$\mathrm{H_t = aH_{xx}}$ ………………………………………………………………………………….(D-2)

The initial and boundary conditions change as:

I.C.: $\mathrm{H(x,0)} = \frac{\mathrm{x-L+w_1}}{\mathrm{-L+w_1}}$ where $\mathrm{w_1} = \frac{\mathrm{kA}}{\mathrm{q_i\mu\acute{c}}}$ here, $\mathrm{q_i}$ is the flowrate at which initial steady state was stablished.

B.C.1: $\mathrm{H(0,t) = 1}$

B.C.2: $\mathrm{H_x|_{x=L} = w_2H|_{x=L} - w_3H_t|_{x=L}}$

Where $\mathrm{w_2} = \frac{\mathrm{q\mu\acute{c}}}{\mathrm{KA}}$ and $\mathrm{w_3} = \frac{\mathrm{\mu cV}}{\mathrm{KA}}$

Then substitute $U(x,t) = H(x,t) - \frac{x-L+w_1}{-L+w_1}$ to simplify initial and boundary condition 1.

$U_t = aU_{xx}$………………………………………………………...…………………...(D-3)

I.C.: $U(x,0) = 0$

B.C.1: $U(0,t) = 0$

B.C.2: $U_x|_{x=L} = w_2 U|_{x=L} - w_3 U_t|_{x=L} + w_4$

Where $w_4 = \frac{w_1 w_2 - 1}{-L+w_1}$

Now, we take Laplace from Eq. D-3 and its initial and boundary conditions.

$\widetilde{U}_{xx} - \frac{S}{a}\widetilde{U} = 0$…………………………………………………….………………...(D-4)

I.C.: $\widetilde{U}(x,0) = 0$

B.C.1: $\widetilde{U}(0,S) = 0$

B.C.2: $\widetilde{U}_x|_{x=L} = w_2\widetilde{U}|_{x=L} - w_3 S\widetilde{U}|_{x=L} + \frac{w_4}{S}$

The general solution of ordinary differential equation of Eq. D-4 is in the form of:

$\widetilde{U}(x,S) = Ae^{\sqrt{\frac{S}{a}}x} + Be^{-\sqrt{\frac{S}{a}}x}$……………………………………………………….....(D-5)

Applying initial or first boundary condition we will get:

$A = -B$

Applying second boundary condition we will get:

$A = \frac{w_4}{2S\sqrt{\frac{S}{a}}\cosh\left(\sqrt{\frac{S}{a}}L\right) + 2S(Sw_3 - w_2)\sinh\left(\sqrt{\frac{S}{a}}L\right)}$…………………………………………………...(D-6)

Thus, the final form of solution of Eq. D-4 in Laplace domain is:

$\boldsymbol{\widetilde{U}(x,S)} = \frac{\boldsymbol{w_4 \sinh\left(\sqrt{\frac{S}{a}}x\right)}}{\boldsymbol{S\sqrt{\frac{S}{a}}\cosh\left(\sqrt{\frac{S}{a}}L\right) + S(Sw_3 - w_2)\sinh\left(\sqrt{\frac{S}{a}}L\right)}}$………………………………………………..(D-7)

Since this equation is complicated for analytical Laplace inverse, we use Stehfest's method (Stehfest 1970) to find Laplace inversion numerically. The method is explained in the work of Hassanzadeh and Pooladi-Darvish (2007).

Appendix E
General Equation of Two-Phase Immiscible Displacement

Consider the displacement of oil by water in a linear horizontal plug at a constant flowrate. Start with Darcy equation for each phase

$$q_w = -\frac{kk_{rw}A}{\mu_w}\frac{\partial P_w}{\partial x}, \tag{E-1}$$

$$q_o = -\frac{kk_{ro}A}{\mu_o}\frac{\partial P_o}{\partial x} \tag{E-2}$$

Using capillary pressure definition

$$\frac{\partial P_c}{\partial x} = \frac{\partial P_o}{\partial x} - \frac{\partial P_w}{\partial x} \tag{E-3}$$

Combining Eq. E-1 and Eq. E-2 into Eq. E-3:

$$\frac{\partial P_c}{\partial x} = \frac{q_w\mu_w}{kk_{rw}A} - \frac{q_o\mu_o}{kk_{ro}A} \tag{E-4}$$

The true fractional flow of water and oil are defined as:

$$f_w = \frac{q_w}{q_t}, f_o = \frac{q_o}{q_t} \tag{E-5}$$

Combining Eq. E-4 and Eq. E-5:

$$f_w = \frac{1+\frac{kk_{ro}A}{q_t\mu_o}\frac{\partial P_c}{\partial x}}{1+\frac{k_{ro}\mu_w}{k_{rw}\mu_o}} \tag{E-6}$$

Now, consider the continuity equation for the water phase

$$\emptyset A\frac{\partial S_w}{\partial t} + \frac{\partial q_w}{\partial x} = 0 \tag{E-7}$$

Eq. E-7 can be written in dimensionless form as

$$\frac{\partial S_w}{\partial t_D} + \frac{\partial f_w}{\partial x_D} = 0, \tag{E-8}$$

where

$$t_D = \frac{q_t t}{AL\emptyset}, \tag{E-9}$$

$$x_D = \frac{x}{L} \tag{E-10}$$

Substituting Eq. E-6 into Eq. E-8 gives the second-order, nonlinear, parabolic partial differential equation for the water phase. Here, P_c and k_r are considered a function of S_w.

$$\frac{\partial S_w}{\partial t_D} + \frac{\partial}{\partial x_D}\left[\frac{1+\frac{kk_{ro}A\partial P_c}{q_t\mu_o\ \ \partial x}}{1+\frac{k_{ro}\mu_w}{k_{rw}\mu_o}}\right] = 0 \quad \text{(E-11)}$$

Appendix F
Experimental Details of Waterflooding Tests

Here, we present the procedure for plug preparation, waterflooding tests, and permeability measurement. We clean the plug using a polar (methanol) and a nonpolar (toluene) solvent to remove all the residual fluids inside the core plug (McPhee et al. 2015). Then put it in an oven at 90*℃* and monitor its weight with time to make sure it is completely dry. After that, we put the plug inside a core holder under 1800 psi confining pressure and vacuum it for one day (**Figure F-1**). Then, we inject brine at a constant pressure of 1100 psi to saturate the plug. We inject 4-5 pore volume to make sure the plug is fully saturated with brine. After that, we inject oil at a constant flowrate of *0.06 cc/hr* to displace the brine and reach the S_{wirr}. We measure the pressure profile during the displacement process. When pressure stabilizes, we reach the S_{wirr}. We age the core plug for one week under 1100 psi pressure to restore the initial state of the wettability. Then, we measure the permeability of the plug saturated with oil at S_{wirr} by oil injection at different flowrates based on the method described in chapter two (Yousefi and Dehghanpour 2022). Now, the plug is ready for waterflooding test. We inject water at a constant flowrate of *0.06 cc/hr* to displace oil out of the plug. We record the pressure profile during the displacement process. The waterflooding continues until the recorded pressure is stabilized. We measure the permeability of the plug in this stage where the plug is saturated with water at S_{or}.

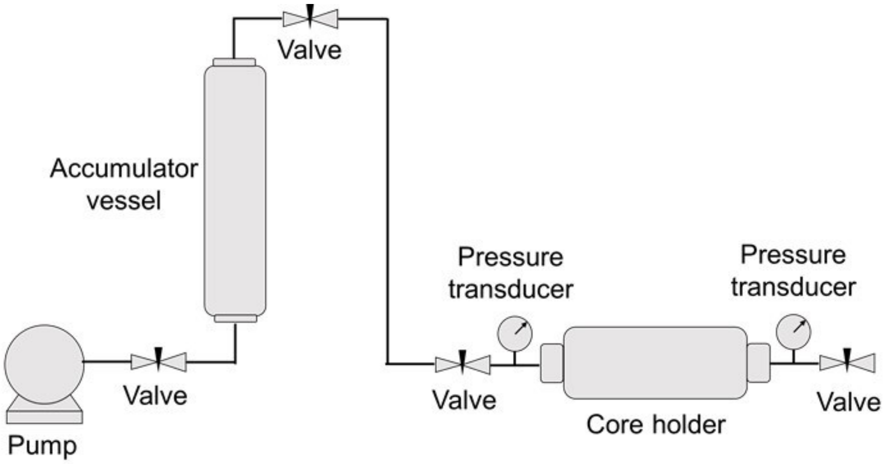

Figure F-1: Schematic of coreflooding apparatus used for waterflooding experiment.

Appendix G
Synthetic Brine Preparation Procedure

We use water analysis report of reservoir brine from a well in Montney formation to prepare the synthetic brine. Table G-1 lists the ion compositions of the reservoir and synthetic brine. First, we calculate the required mass for each salt based on the mass balance. The sequence of adding salts into the water is important since some salts may precipitate in presence of other salts due to low solubility in water. We use ASTM D1141 standard to follow a specific sequence for mixing the salts with water. The procedure of preparing the synthetic brine is as follows:

- 189.3631gr NaCl and 2.3994 gr $MgSO_4.7H_2O$ are added to 1000 cc of DI water in beaker 1 and stirred for about 3 hours.
- 2.5764 gr $MgCl_2$ and 6.1612 gr $CaCl_2.2H_2O$ are added to 250cc of DI water in beaker 2 and stirred for about 3 hours.
- 3.4890 gr KCl and 1.5425 gr $NaHCO_3$ were added to 250cc of DI water in beaker 3 and stirred for about 3 hours.
- Solution of beaker 2 is gradually added to beaker 1 with rigorous mixing (rpm=500). Then, the solution of beaker 3 is added to beaker 1. The whole brine is stirred for about 1.5 hours.

We notice that the solution is not clear, and some solid particles precipitated at the bottom of bottle after 2 days.

The source of precipitation is bicarbonate ion. Since its concentration is low (747 ppm), we decide to remove $NaHCO_3$ from solution to prevent the precipitation. To keep the ionic strength same as original brine with $NaHCO_3$, 0.7153 gr NaCl is added to the solution. The modified brine solution is clear, and no more precipitation is observed after 1 week.

Table G-1: ion compositions of the reservoir brine and synthetic brine.

Ion	Na	K	Ca	Mg	Cl	HCO_3	SO_4
Concentration (mg/L) in Brine	47630	1220	1120	596	80945	747	623
Concentration (mg/L) in Synthetic Brine	49750	1220	1120	596	81379	0	623